Engineering Solid Oxide CO_2 Electrolysis:

From Nanoparticle-Decorated Perovskite Cathode to System-Level Modeling

by

Seyed Mohammadali Emadi Foshtomi

A thesis

presented to the University of Waterloo

in fulfillment of the

thesis requirement for the degree of

Doctor of Philosophy

in

Chemical Engineering

Waterloo, Ontario, Canada, 2025

© Seyed Mohammadali Emadi Foshtomi 2025

Examining Committee Membership

The following served on the Examining Committee for this thesis:

External member:	Inès Esma Achouri Associate Professor Department of Chemical Engineering and Biotechnology Engineering Université de Sherbrooke
Supervisor:	Eric Croiset Professor Department of Chemical Engineering University of Waterloo
Internal members:	Xianshe Feng Professor Department of Chemical Engineering University of Waterloo
	Milad Kamkar Assistant Professor Department of Chemical Engineering University of Waterloo
Internal-external member:	XiaoYu Wu Assistant Professor Department of Mechanical and Mechatronics Engineering University of Waterloo

Author's Declaration

This thesis consists of material all of which I authored or co-authored: see Statement of Contributions included in the thesis. This is a true copy of the thesis, including any required final revisions, as accepted by my examiners.

I understand that my thesis may be made electronically available to the public.

Statement of Contributions

Chapter 5 of this thesis is based on the following published article:

Emadi, M., Barahimi, V., & Croiset, E. (2025). Integrated direct air CO_2 capture and solid oxide electrolyzer for sustainable chemical production: Case studies of methanol and synthesis fuel. Journal of CO_2 Utilization, 96, 103096. https://doi.org/10.1016/J.JCOU.2025.103096

The work presented in this chapter was carried out in collaboration with Mr. Vahid Barahimi and my supervisor, Professor Eric Croiset. Mr. Barahimi contributed to Fischer–Tropsch process simulation, while Professor Croiset provided supervision, guidance, and critical feedback on data interpretation and manuscript preparation. The overall research concept, methodology, and writing of the chapter were primarily completed by the author of this thesis.

The inclusion of this published work complies with the guidelines of the University of Waterloo and the publisher's policies.

Artificial Intelligence Disclosure

Portions of this thesis were developed with the assistance of artificial intelligence for text refinement and grammar checking. All content has been reviewed, edited, and validated by the author to ensure accuracy, originality, and alignment with academic standards.

Abstract

Solid oxide electrolysis cell (SOEC) is a promising technology for CO_2 electrolysis and subsequent conversion to useful chemicals. This thesis combines the experimental development of new cathode materials with system-level simulation to enhance the performance of SOECs for CO_2 electrolysis and assess their applicability for fuel production. There are two components to the work: (1) proposing nanoparticle decorated perovskite cathode material and (2) integration of DAC, SOEC and synfuel production and asses its performance with techno-economic and environmental analysis.

In the experimental section, the focus was on the cathode material of the SOEC since it is the limiting factor for CO_2 electrolysis. $Sr_2Fe_{1.5}Mo_{0.5}O_{6-\delta}$ (SFM) has attracted much attention due to its decent performance of CO_2 electrolysis. To enhance the SFM performance, it was modified by doping bismuth and nickel to make a new composition of $Bi_{0.1}Sr_{1.9}Fe_{1.4}Ni_{0.1}Mo_{0.5}O_{6-\delta}$ (BiSFNiM). The Ni-doping made it possible for Fe–Ni nanoparticles to exsolve in-situ when the material was reduced by 5% H_2/Ar. Structural characterizations like XRD showed that, during exsolution, the material changed from a pure double perovskite structure to a mixed-phase material with both Ruddlesden–Popper (RP) and residual double perovskite phases and metallic nanoparticles. Using electron microscopy (SEM/TEM/EDS), it showed that Ni migrated to the surface of the perovskite bulk where it forms Fe–Ni nanoparticles. This material, then, was used as the cathode of SOEC and the results showed that these exsolved Fe–Ni nanoparticles significantly improved the electrocatalytic activity for the CO_2 reduction reaction (CO_2RR). Electrochemical performance tests demonstrated substantial improvements in current density and polarization resistance. The fabricated cell achieved a peak current density of 1.3 A/cm² at 800 °C under an applied voltage of 1.6 V, while it was 1.0 A/cm² for the non-exsolved nanoparticles sample.

The second half of this thesis was a process simulation and system-level evaluation of an integrated DAC-SOEC facility. The technology was based on capturing 250,000 tonnes of CO_2 from the air each year and turning it into either methanol or synthesis fuel through downstream processes. Methanol production was 36.4 tonnes per hour, while synfuel output was 15.1 tonnes per hour. The techno-economic analysis found that the levelized production cost for methanol was $1.32 per kilogram (nearly double the current market price) and for synfuel, it was $2.78 per kilogram (approximately 45% more than normal expenses). Using Ontario's electricity grid mix, the simulated plant achieved greenhouse gas emissions of 31.1 gCO_2-eq/MJ for methanol and 5.2 gCO_2-eq/MJ for synfuel, the latter representing a reduction compared to conventional fossil-based pathways (40 g-CO_2-eq/MJ-MeOH and 29 g-CO_2-eq/MJ-synfuel). Further sensitivity analysis demonstrated that switching to fully renewable electricity sources, such as hydropower or wind, could push the synfuel production case into a net-negative emissions region.

In conclusion, this thesis contributes to both fundamental and applied aspects of CO_2 electrolysis. On the material side, it offers a strong plan for boosting cathode performance by co-doping and nanoparticle exsolution. It also gives information about phase stability, exsolution behavior, and catalytic activity. At the system level, it shows that combining DAC and SOEC for sustainable fuel production is possible from a technological, economic, and environmental point of view. The dual approach shows how innovative materials and systems design can work together to help us toward carbon-neutral chemical manufacture.

Acknowledgments

I would like to sincerely thank my supervisor, Dr. Eric Croiset, for their guidance, encouragement, and support throughout my PhD journey. Their advice and expertise have been invaluable to this work.

I am deeply grateful to my parents, Mohammadjavad Emadi and Sedigheh Heydari, whose endless love, sacrifices, and belief in me have been the foundation of all my achievements. I also want to thank my brothers and sister, Sajjad, Ata and Maryam, for their constant support, encouragement, and for always being just a phone call away whenever I needed motivation or comfort.

To my wife, Zahra Razavi, who joined me partway through this journey, thank you for your patience, understanding, and for bringing balance and strength to the second half of my PhD.

I also want to thank my friends, Vahid Barahimi and Saeed Habibpour, for making this time more enjoyable.

This work would not have been possible without all of you.

Dedication

To my parents

Table of Contents

Examining Committee Membership ii

Author's Declaration iii

Statement of Contributions iv

Abstract v

Acknowledgments vii

Dedication viii

List of Figures xii

List of Tables xvi

List of Abbreviations xvii

Chapter 1 Introduction 1

1.1 Aims and Objective 2

1.2 Structure and content of this dissertation 5

Chapter 2 Literature Review 6

2.1 Advantages and Challenges of Solid Oxide CO_2 Electrolysis 6

2.2 Working principle of CO_2-SOEC 7

2.2.1 Thermodynamic of CO_2-SOEC 8

2.2.2 Performance of CO_2-SOEC 10

2.3 Electrolyte and Air Electrode Materials for Solid Oxide Cells 13

2.4 Cathode (fuel electrode) materials for SOEC 14

2.4.1 Perovskites 15

2.4.2 Double perovskite 18

2.5 CO_2 electrolysis using double perovskite as fuel electrode 19

Chapter 3 Experimental Methodology 28

3.1 Perovskite powder synthesis 28
3.2 Cell fabrication 30
3.2.1 Electrolyte substrate 32
3.2.2 Buffer layer 34
3.2.3 Electrodes 35
3.3 Testing of the cells 38
3.4 Characterization and electrochemical measurements 41
Chapter 4 Experimental Results of Fe–Ni Nanoparticle-decorated $Bi_{0.1}Sr_{1.9}Fe_{1.4}Ni_{0.1}Mo_{0.5}O_{6-\delta}$ Cathode in CO_2 Electrolysis 42
4.1 Crystal structure 43
4.2 Interfacial compatibility 44
4.3 Thermal Stability 45
4.4 Cathode material exsolution behaviors 46
4.4.1 X-ray Diffraction results 47
4.4.2 X-ray photoelectron spectroscopy results 49
4.4.3 Scanning electron microscopy results 51
4.4.4 Transmission electron microscopy results 52
4.5 Cell structure 56
4.6 Cell electrochemical performance 59
4.6.1 I–V Characteristics of BiSFMNi and Fe–Ni@BiSFMNi Cathodes 60
4.6.2 Electrochemical Impedance Spectroscopy (EIS) Analysis 63
4.6.3 Distribution of Relaxation Times (DRT) Analysis 64
4.7 Long-term stability 66
4.8 Performance comparison with literature 67

4.9 Experimental work conclusion 69
Chapter 5 Simulation Study of DAC-SOEC-Methanol/Synfuel Plant 70
5.1 Introduction 70
5.2 Process overview 74
٥,٢,١ Direct air capture (DAC) model 75
5.2.2 SOEC model 79
5.2.3 Methanol production model 82
5.2.4 Fischer-Tropsch model 84
5.3 Methodology 86
5.3.1 Economic analysis 87
5.3.2 Net CO2 equivalent emission assessment 89
5.3.3 Key performance indicators 90
5.4 Results and discussion 91
5.4.1 Base case results 91
5.4.2 Economic analysis results 92
٥,٤,٣ Environmental analysis 99
5.5 Simulation study conclusion 103
Chapter 6 Conclusions and Recommendations for Future Work 104
6.1 Conclusion 104
6.2 Recommendations for future work 106
References 108
Appendix 118

List of Figures

Figure 1.1. CO_2 loop for carbon capture and utilization [4], with permission from © John Wiley and Sons. 2

Figure 1.2. Schematic outline of the research framework. 4

Figure 2.1. Schematic of a solid oxide CO_2 electrolysis cell. 8

Figure 2.2. Energy demand as a function of temperature for CO_2 electrolysis [7], with permission from © ACS Publications. 9

Figure 2.3. Perovskite ABX_3 lattice. (a) Large A and small B cations, with X anions; (b) octahedron by X anions; (c) octahedra lattice [19], with permission from © Taylor & Francis. 17

Figure 2.4. Crystal structures of: (a) Single perovskite; (b) double perovskite; (c) layered perovskite [19], with permission from © Taylor & Francis..... 18

Figure 2.5. Ordering of BO_6 octahedra in $A_2B'B''O_6$ double perovskites: (a) zero-dimensional or rocksalt type, (b) one-dimensional or columnar, and (c) two-dimensional or layered [19], with permission from © Taylor & Francis. 19

Figure 2.6. Ordering of A-site ions in $A'A''B_2O_6$ double perovskites: (a) zero-dimensional or rocksalt type, (b) one-dimensional or columnar, and (c) two-dimensional or layered [19], with permission from © Taylor & Francis. 19

Figure 3.1. Solution combustion synthesis process followed in this research. 31

Figure 3.2. Overall cell fabrication process. 31

Figure 3.3. The basic principle of dry pressing [51], with permission from © Elsevier. 33

Figure 3.4. LSGM electrolyte substrates after sintering. 33

Figure 3.5. LDC buffer layer on the electrolyte substrate after sintering. 34

Figure 3.6. Screen printing working principle [52], with permission from © Royal Society of Chemistry. 35

Figure 3.7. Screen printing machine and the mesh. 36

Figure 3.8. Screen printed electrode using as-prepared electrode materials showing weak adhesion.

..... 37

Figure 3.9. Particle size analysis of (a) as-prepared SFM (median size=22.1 μm) and (b) after 24 hr ball milling (median size=1.7 μm). 37

Figure 3.10. Sintered single cells with electrode active area of 1 cm^2 ready for testing, (a) fuel side, and (b) air side. 38

Figure 3.11. SOEC test station at the University of Waterloo. 40

Figure 3.12. Fiaxell fuel cell test station parts. 40

Figure 4.1. Schematic of the solid oxide electrolysis cell configuration used in this study. 42

Figure 4.2. XRD patterns of SFM, BiSFM, and BiSFMNi powders. 44

Figure 4.3.Chemical compatibility of binary mixes of BiSFMNi -LDC, BiSFMNi -LSGM and LDC-LSGM. 45

Figure 4.4. TGA of SFM and BiSFMNi samples in N_2, Air and CO_2 atmospheres. 46

Figure 4.5. XRD patterns of BiSFMNi samples as-synthesized and reduced in 5% H_2/Ar at 800 °C for different duration. 47

Figure 4.6. Rietveld refinement results of XRD patterns BiSFMNi sample reduced in 5% H_2/Ar at 800 °C for 1 hour. 48

Figure 4.7. XRD patterns of BiSFMNi in oxidized, reduced, and reoxidized states. 49

Figure 4.8. XPS spectra of (a) Fe 2*p*, (b) Ni 2*p*, (c) Mo 3*d*, and (d) O 1*s* regions before and after 1 hr reduction in 5% H_2-Ar. 50

Figure 4.9. SEM images of BiSFMNi in three states: As-synthesize, reduced in 5% H_2/Ar at 800 °C for 2, 10, 30 and 60 minutes, and reoxidized in air. 52

Figure 4.10. TEM image and EDS analysis of the as-synthesized BiSFMNi sample. 55

Figure 4.11. TEM image and EDS analysis of the reduced BiSFMNi sample. 55

Figure 4.12. STEM image and EDS elemental mapping of BiSFMNi perovskite after reduction treatment showing exsolved nanoparticles. 56

Figure 4.13. Cross-sectional SEM image of the fabricated single cell. 57

Figure 4.14. Line EDS elemental mapping across the cell cross-section. 58

Figure 4.15. I–V characteristics of three independently fabricated cells, demonstrating reproducibility of electrochemical performance. 60

Figure 4.16. Electrochemical performance of cell under CO_2 electrolysis conditions: (a) I–V characteristics of BiSFMNi and Fe–Ni@BiSFMNi cathodes, (b) Percentage improvement in current density of Fe–Ni@BiSFMNi over BiSFMNi, (c) I–V characteristics of the Fe–Ni@BiSFMNi cathode measured at 700 °C, 750 °C, and 800 °C, and (d) Short-term electrochemical stability test under constant voltage operation at 1.0 V, 1.2 V, and 1.4 V. .. 62

Figure 4.17. Electrochemical impedance spectra (EIS) of (a) cell with Fe–Ni@BiSFMNi at OCV, 1.2 V and 1.4V, (b) Comparison of Fe–Ni@BiSFMNi and BiSFMNi, and (c) Temperature dependence of EIS spectra of Fe–Ni@BiSFMNi at 1.2 V. 64

Figure 4.18. DRT spectra: (a) comparison of Fe–Ni@BiSFMNi and BiSFMNi cathodes at 800 °C and 1.2 V, and (b) DRT spectra of Fe–Ni@BiSFMNi at 800 °C, 750 °C, and 700 °C under 1.2 V applied voltage. 66

Figure 4.19. Long-term CO_2 electrolysis performance at 1.4 V over 140 hours. 67

Figure 5.1. Overall direct air capture to fuel plant configuration. 75

Figure 5.2. Reactions occurring in the DAC unit. 76

Figure 5.3. Aspen plus model of DAC. 78

Figure 5.4. Aspen Plus model of Calciner. 78

Figure 5.5. SOEC Aspen Plus Model. 82

Figure 5.6. Methanol production Aspen model. 83

Figure 5.7. Aspen Plus model of Fischer-Tropsch unit. 86

Figure 5.8. Contribution of each part to the capital cost for (a) methanol and (b) synfuel case studies. 95

Figure 5.9. Effect of electricity sources on the levelized cost of production. Ontario grid was the base case scenario. 96

Figure 5.10. Effect of SOEC replacement period on the levelized cost of production. 97

Figure 5.11. Effect of SOEC cost reduction per five years on the levelized cost of production. . 98

Figure 5.12. Effect of interest rate on the levelized cost of production. 99

Figure 5.13. GHG emissions contributors for both case studies..... 102

Figure 5.14. GHG emissions for different sources of electricity. 102

List of Tables

Table 4.1. A comparison of current densities with literature at 800 °C for pure CO_2 electrolysis. 68

Table 5.1. Fundamental equations for the simulation of the SOEC [68–70]. 80

Table 5.2. Characteristics of the SOEC stack [68–70]. 81

Table 5.3. Kinetic constants for methanol production reactions [72]. 84

Table 5.4. Equipment purchase cost. 88

Table 5.5. Economic parameters assumed in the base case. 88

Table 5.6. Electricity market price of different renewable sources. 89

Table 5.7. Emission factors of resources used in this research. 90

Table 5.8. Required supplies and production for the base case. 92

Table 5.9. Investment cost of different units and levelized cost of production. 94

Table 5.10. Carbon balance for methanol and synfuel production. 101

Table A.1. Calculation of reagent quantities for sol–gel synthesis of $Sr_{1.9}Bi_{0.1}Fe_{1.4}Ni_{0.1}Mo_{0.5}O_{6-\delta}$ Perovskite. 118

Table A.2. Carbon Aspen PLUS™ simulation block types and parameters. 119

List of Abbreviations

A_{cell}	active surface area, m^2
C	Annualized cost
D_{eff}	effective diffusion coefficient, m^2/s
F	Faraday constant, C/kmol
f	partial fugacity, bar
$\overline{\Delta g}^{\circ}$	change in molar Gibbs free energy, J/mol
$\Delta \dot{H}$	enthalpy change of reaction, J/mol
i	current, A
j	current density, A/m^2
k	reaction rate constant
K	adsorption equilibrium constant, bar^{-1}
LHV	Lower heating value, kJ/kg
n_{e}	number of electrons
$\dot{n}$	molar flow rate, mol/s
$\dot{m}$	Mass flow rate, kg/s
P	pressure, Pa or bar
p	partial pressure
r	reaction rate per weight of catalyst, mol/kg
$\dot{Q}$	heat rate, W
$\bar{R}$	universal gas constant, J/mol.K
T	temperature, K
V	voltage, V
U_{rev}	reversible cell voltage, V
$\dot{W}$	power, W
Z	Cost, $

Subscripts

0	atmospheric condition
act	activation
conc	concentration
el	electrolyte
equip	equipment
eq	equivalent
elec	electricity
ohm	ohmic
ref	reference

Abbreviations

CCU	carbon capture and utilization
CCPP	CO_2 capture per amount of product
CRF	capital recovery factor
DAC	direct air carbon capture
CEPCI	chemical Engineering Plant Cost Index
LPC	levelized production cost
FT	Fischer-Tropsch
GWP	global warming potential
GHG	greenhouse gas
LCP	levelized cost of electricity
LHV	lower heating value
NG	natural gas
rWGS	reverse water gas shift
SEC	specific energy consumption
SOEC	solid oxide electrolysis cells
O&M	operation and maintenance
PEF	primary energy factor
YSZ	$(Y_2O_3)_{0.08}(ZrO_2)_{0.92}$
LSM	$(La_{0.80}Sr_{0.20})_{0.95}MnO_{3-\delta}$
LSGM	$La_{0.80}Sr_{0.20}Ga_{0.80}Mg_{0.20}O_{3-\delta}$
LSCF	$(La_{0.60}Sr_{0.40})_{0.95}Co_{0.20}Fe_{0.80}O_{3-\delta}$
LDC	$La_{0.4}Ce_{0.6}O_{1.8}$
SDC	$Sm_{0.20}Ce_{0.80}O_{1.95}$
GDC	$Gd_{0.10}Ce_{0.90}O_{1.95}$
SFM	$Sr_2Fe_{1.5}Mo_{0.5}O_{6-\delta}$
BiSFMNi	$Bi_{0.1}Sr_{1.9}Fe_{1.4}Ni_{0.1}Mo_{0.5}O_{6-\delta}$
BSCF	$Ba_{0.5}Sr_{0.5}Co_{0.8}Fe_{0.2}O_{3-\delta}$

Chapter 1

Introduction

The ever-increasing use of fossil fuels has been the main cause of global warming via massive emissions of carbon dioxide (CO_2) in the earth's atmosphere, resulting in atmospheric CO_2 concentration increase from 390 ppm in 2012 to 427 ppm in 2025 [1]. This amount of carbon dioxide will have irreparable effects on nature. Electricity, heat production and transportation account for the largest share of carbon dioxide production. Next are the chemical industries that also significantly emit carbon dioxide.

Among the solutions that were put forward to solve the carbon dioxide emissions problem, one solution is carbon capture and storage. In this method, carbon dioxide is captured and stored, for example, in an underground reservoir. However, this method requires a lot of energy, is expensive, and there is a risk of carbon dioxide leakage [2]. As a result, the production of a useful product from carbon dioxide instead of storing it gained more attention. Carbon capture and utilization (CCU) technologies offer a promising avenue to address these dual challenges by not only reducing CO_2 emissions but also converting this greenhouse gas into valuable chemical products. The first step to utilizing CO_2 is its reduction to CO, which can be used further to produce other chemicals when reacted with hydrogen. There are four general methods for converting carbon dioxide into carbon monoxide: thermochemical (thermal energy), electrochemical (electricity), photochemical (photon) and biochemical (biology cultivation). Among these, the electrochemical method has been the focus of much research in recent years. The process is controllable by adjusting temperature and can be linked with renewable energy, electricity production by photovoltaic panels or wind turbines as examples. Direct Air Capture (DAC) technology provides a means to

selectively extract CO_2 from ambient air, offering a scalable and environmentally benign approach to carbon capture. The captured CO_2 can then be utilized as a feedstock for chemical synthesis processes, such as methanol or synthetic fuel (synfuel), thereby closing the carbon cycle and mitigating the environmental impact of anthropogenic CO_2 emissions [3]. Meanwhile, SOEC technology enables the electrochemical conversion of CO_2, when mixed with water, into syngas (a mixture of carbon monoxide and hydrogen) through co-electrolysis at high temperatures The overall carbon loop can be seen in Figure 1.1.

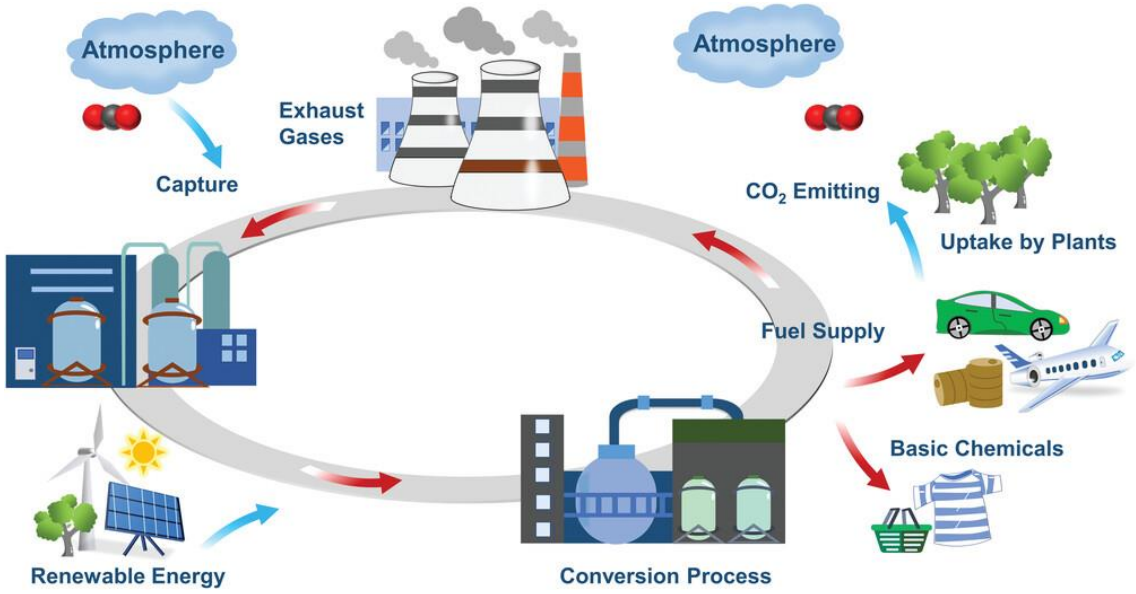


Figure 1.1. CO_2 loop for carbon capture and utilization. Reprinted with permission from [4].

Copyright 2023 John Wiley and Sons.

1.1 Aims and Objective

Due to the slower rate of CO_2 electrochemical reduction in the SOEC cathode compared to the anode's oxygen evolution process, the system has a high resistance. The performance of many cathode materials is also poor due to their low CO_2 catalytic activity and adsorption capacity. Therefore, the main objective of this research is to enhance the performance of CO_2 reduction in

SOEC. It is necessary to develop cathode materials with the optimal combination of high conductivity, structural stability, high CO_2 adsorption capacity, and high electrocatalytic activity for CO_2 splitting.

While optimizing cathode materials can enhance the electrochemical performance of SOECs, it is also essential to evaluate the broader impact of SOEC integration into industrial processes. To assess the feasibility and efficiency of large-scale CO_2 electrolysis, this research also includes a system-level simulation of a DAC-SOEC-Methanol/ Fischer Tropsch plant. This simulation aims to analyze the techno-economic viability and carbon footprint of integrating SOEC technology into a sustainable methanol production process.

To reach the above-mentioned goals, the project is divided into two main objectives:

Objective 1: this part focuses on the synthesis of co-doped double perovskite powder to use as the fuel electrode in SOEC. SOEC cells were initially fabricated using $(Y_2O_3)_{0.08}(ZrO_2)_{0.92}$ (YSZ) as the electrolyte since it is the most common electrolyte in literature. $(La_{0.60}Sr_{0.40})_{0.95}Co_{0.20}Fe_{0.80}O_{3-\delta}$/ $Gd_{0.10}Ce_{0.90}O_{1.95}$ (LSCF/GDC) was used for the air electrode and $Sr_2Fe_{1.5}Mo_{0.5}O_{6-\delta}$ (SFM) for the fuel electrode. LSCF combined with GDC offers high oxygen-ion conductivity and excellent catalytic activity for the oxygen evolution reaction, making it a strong anode choice in SOECs [5]. SFM, as a double perovskite, provides good electronic and ionic conductivity with enhanced CO_2 adsorption and stability, supporting efficient CO_2 electrolysis at the cathode [6]. To enhance the performance, Bi was doped on the A-site of SFM and Ni was doped on the B-site to form $Bi_{0.1}Sr_{1.9}Fe_{1.4}Ni_{0.1}Mo_{0.5}O_{6-\delta}$. The material is then reduced to form nanoparticles on the surface. Following these modifications, the electrolyte was switched from YSZ to $La_{0.80}Sr_{0.20}Ga_{0.80}Mg_{0.20}O_{3-\delta}$ (LSGM) to further increase the performance of the cell.

Objective 2: in the process simulation part of this research, a DAC-SOEC-Methanol/Fischer

Tropsch system was modeled using Aspen Plus. The primary objective of this integrated system is to harness atmospheric CO_2 to produce liquid hydrocarbons, offering a sustainable pathway towards reducing CO_2 emissions and advancing the transition towards a carbon-neutral future. The simulation included process modeling of CO_2 capture, solid oxide electrolysis, and methanol/Fischer-Tropsch plant. Additionally, a techno-economic analysis was conducted to assess the system's cost-effectiveness, while an environmental assessment was performed to evaluate its carbon footprint and sustainability compared to conventional methanol production methods. This study provides insights into the potential of SOEC technology in large-scale CO_2 utilization and renewable fuel production.

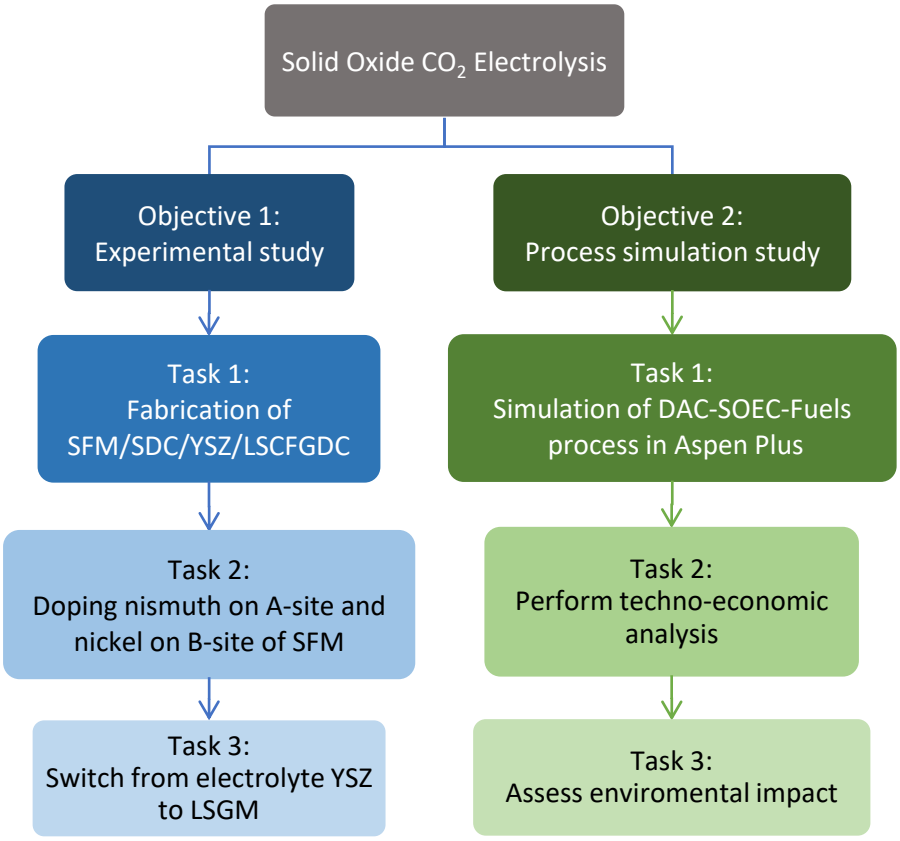


Figure 1.2. Schematic outline of the research framework.

1.2 Structure and content of this dissertation

The contents of each chapter are as follows: Chapter 2 explains how solid oxide cells (SOCs) work by first giving an overview of how SOECs work and then going into detail about the main electrochemical reactions and the thermodynamics that control them. After that, it addresses cathode materials, introduces the perovskite structure, and gives a full review of the literature on how these materials can be used in CO_2 electrolysis.

Chapter 3 details the experimental methodology, including the cell fabrication process, test setup, operating conditions, and characterization techniques. Chapter 4 shows the outcomes of the experimental work. Then, through characterization methods, a comparison is conducted to show how the proposed cathode can improve CO_2 electrolysis performance. In chapter 5, the second objective of this thesis is explored. This chapter starts with a literature review on chemical production using direct air capture and SOEC is presented, followed by a full description of methodology and modeling. Then, the results of the simulation are presented including both economic and environmental aspects. Finally, in chapter 6, an overall summary and conclusions of the thesis are given, followed by recommended future work.

Chapter 2

Literature Review

In this chapter, the working principle of a solid oxide cell is explained and then a literature review of recently published papers on the cathode materials is presented, with a focus on perovskite-based cathode materials for CO_2 reduction.

2.1 Advantages and Challenges of Solid Oxide CO_2 Electrolysis

Compared with more established low-temperature electrolysis technology, high-temperature solid oxide electrolysis has gained attention due to some significant advantages. First, it has higher conversion efficiency, meaning high electrical efficiency as high as 95% [7]. This is 25-30% higher than low-temperature electrolysis technologies of alkaline electrolysis cells (AEC) and proton exchange membrane electrolysis cells (PEMEC) [8], which means lower electricity consumption. Second, SOECs can use a wider range of electrolytes, including solid ceramic materials, which can make them more durable and resistant to degradation over time. Third, SOECs can operate in both fuel cell and electrolysis modes, allowing for flexibility in energy storage and production. Finally, SOECs have the potential to be more cost-effective and environmentally friendly compared to other electrolysis technologies due to their high efficiency and use of abundant and lower cost materials. One important feature of SOECs is that they can produce syngas, i.e. mixture of CO and H_2, directly from co-electrolysis of CO_2 and H_2O. The syngas can be used to produce a broad range of fuels and chemicals like methanol, ethanol, methane, etc. The ratio of CO/H_2 for different applications can be adjusted by varying the ratio of the CO_2/H_2O feed into the SOEC. However, some drawbacks of SOEC are the slower rate of CO_2 electrochemical reduction in the cathode compared to that of the anode's oxygen evolution process. Many cathode materials have

insufficient CO_2 catalytic activity and adsorption capacity, which results in poor cell performance. The advancement of SOEC technology thus necessitates the development of cathode materials that possess high conductivity, structural stability, high CO_2 adsorption capacity, and high electrocatalytic activity for CO_2 splitting.

2.2 Working principle of CO_2-SOEC

As shown in Figure 2.1, a Solid Oxide Electrolysis Cell (SOEC) consists of three primary components: the cathode (fuel electrode), the anode (air electrode), and the electrolyte, each playing a crucial role in the electrochemical conversion process.

- Cathode (fuel electrode)

  The cathode is responsible for the reduction of carbon dioxide (CO_2) into carbon monoxide (CO) and oxygen ions (O^{2-}). In an SOEC operating in CO_2 electrolysis mode, CO_2 is supplied to the cathode, where it undergoes an electrochemical reduction reaction: $CO_2 + 2e^- \rightarrow CO + O^{2-}$. This reaction requires electrons, which are supplied from an external power source, driving the electrochemical process. The cathode must exhibit high electronic conductivity, excellent catalytic activity for CO_2 reduction and stability in a reducing atmosphere.

- Electrolyte

  The electrolyte is a dense, ion-conducting ceramic layer that selectively allows oxygen ions (O^{2-}) to pass from the cathode to the anode while blocking electron transport. The electrolyte must be dense to prevent gas crossover and ensure efficient ion transport.

- Anode (air electrode)

  At the anode, the oxygen ions (O^{2-}) that migrate through the electrolyte from the cathode are oxidized to form molecular oxygen (O_2), releasing electrons back into the external circuit: $O^{2-} \rightarrow \frac{1}{2}O_2 + 2e^-$. This oxidation reaction completes the electrochemical process. The anode

material must exhibit high electronic and ionic conductivity, as well as stability in an oxidizing atmosphere.

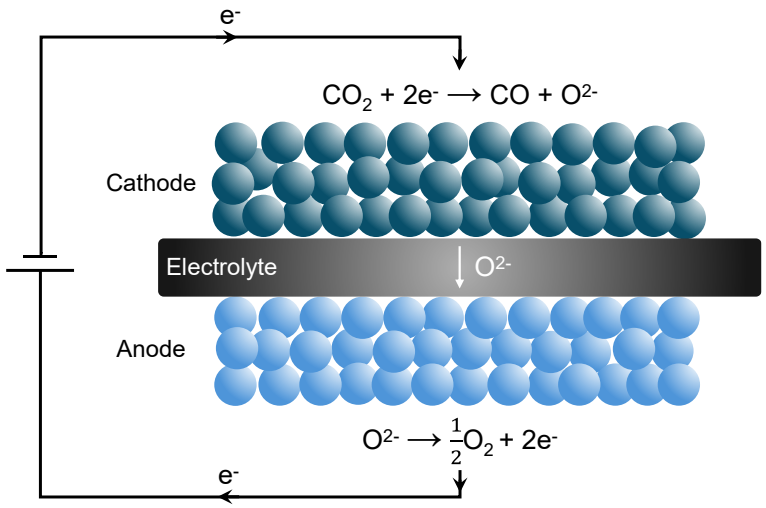


Figure 2.1. Schematic of a solid oxide CO_2 electrolysis cell.

2.2.1 Thermodynamic of CO_2-SOEC

During the overall CO_2 reduction reaction (CO_2RR, Eq. 1), two half electro-reactions occur at the cathode and the anode (Eqs. 2 and 3, respectively).

$$CO_{2(gas)} \rightleftharpoons CO_{(gas)} + \frac{1}{2}O_{2(gas)} \quad (1)$$

$$\text{Cathode reaction: } CO_{2(gas)} + 2e^- \rightleftharpoons CO_{(gas)} + O^{2-} \quad (2)$$

$$\text{Anode reaction: } O^{2-} \rightleftharpoons 2e^- + \frac{1}{2}O_{2(gas)} \quad (3)$$

CO_2RR's total energy consumption can be calculated based on the enthalpy change according to Eq. 4:

$$\Delta_r H^0 = \Delta_r G^0 + T\Delta_r S^0 \quad (4)$$

where 'r' stands for reaction, and '0' refers to standard conditions of (1 bar and 25 °C). $\Delta_r H^0$ is the change in both thermal energy $T\Delta_r S^0$ and Gibbs free energy $\Delta_r G^0$, which is the electrical

energy. Assuming that CO_2RR is ideally reversible with two electrons transferred, $\Delta_r G^0$ is the electrical energy (Eq. 5), when there are no byproducts or extra work done to the environment.

$$\Delta_r G^0 = 2E^0 F \tag{5}$$

where E^0 is the electromotive force (EMF) at standard pressure, and F is the Faraday constant.

The value of E^0 under standard conditions (1 bar and 25 °C) is 1.33 V at. Due to the temperature dependence of $\Delta_r G^0$, E^0 changes with temperature as well, as seen in Figure 2.2. E^0 drops because of the thermal energy contributing more to the overall enthalpy change at higher temperatures. For instance, at the usual SOEC operating temperature of 800 °C, E^0 is 0.98 V.

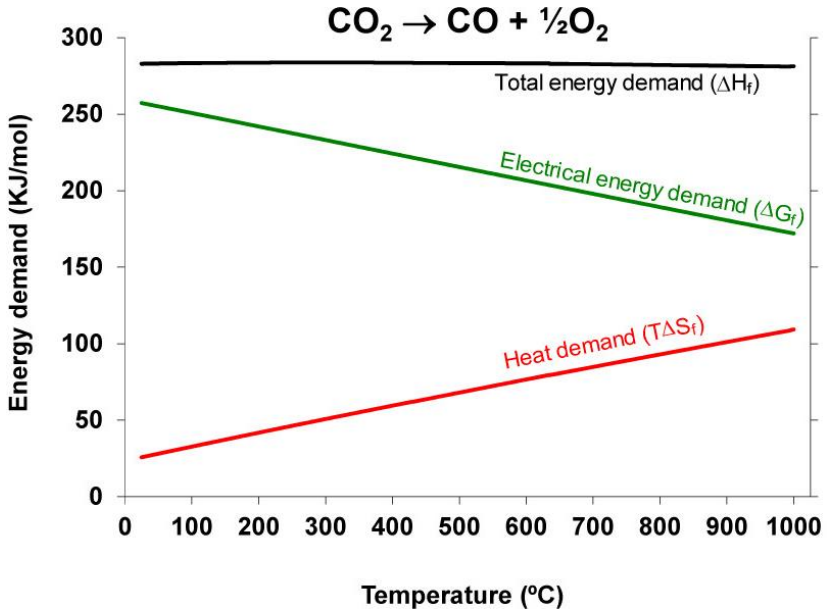


Figure 2.2. Energy demand as a function of temperature for CO_2 electrolysis. Reprinted with permission from [7]. Copyright 2014 ACS Publications.

The partial pressures of CO_2 and CO in the cathodic chamber and O_2 in the anodic chamber must be considered as the two half-cell processes (Eqs. 2 and 3) continue independently at the cathode and the anode. The potential when the reaction achieves equilibrium is described by the reversible potential E_{rev}, which is determined by the partial pressures. When the cathodic potential is greater

than E_{rev}, CO_2 is reduced, but when it is less than E_{rev}, CO is oxidized. The Nernst equation is used to compute E_{rev}:

$$E_{rev} = E^0 + \frac{RT}{2F} \ln \left(\frac{p_{CO,c}\, {p_{O_2,a}}^{1/2}}{p_{CO_2,c}} \right) \quad (6)$$

where p_i represents the partial pressure of CO and CO_2 at the cathode and O_2 at the anode, and the subscripts "c" and "a" stand for the cathode and anode, respectively. While the Nernst equation provides the theoretical equilibrium voltage for an electrochemical cell, the actual voltage observed in an SOEC under open-circuit conditions is known as the Open Circuit Voltage (OCV). In real systems, the measured OCV often deviates from theoretical value due to various practical losses like gas crossover, sealing imperfections, and minor electronic leakage in the electrolyte. When the SOEC is operating (i.e., current is flowing), additional losses such as activation, ohmic, and concentration losses further reduce the actual operating voltage, as described in the next section.

2.2.2 Performance of CO_2-SOEC

In practical operation, the actual cell voltage required to drive electrolysis is higher than the OCV due to various losses, known as overpotentials. These overpotentials arise from electrode reaction kinetics, ionic and electronic resistances, and mass transport limitations. As a result, additional energy input is needed to overcome these inefficiencies and sustain electrochemical reactions. The required potential (V) applied to the SOEC can be written as:

$$V = E_{rev} + \eta_{act,c} + \eta_{act,a} + \eta_{ohmic} + \eta_{con,a} + \eta_{con,c} \quad (7)$$

where $\eta_{act,c}$is the activation overpotential of cathode; $\eta_{act,a}$ the activation overpotential of anode; η_{ohmic} the ohmic overpotential; $\eta_{con,c}$ the concentration overpotential of cathode; and $\eta_{con,a}$ the concentration overpotential of anode. The current is calculated using Eq. (8)

$$i = 4 \times \dot{n}_{O_2} \times F \tag{8}$$

where $\dot{n}$ is molar flow rate.

The processes linked to the cathodic polarization for CO_2RR utilizing an SOEC device typically consist of three parts: (1) CO_2 adsorption and activation; (2) electronic/oxygen ionic migration from/to the reaction sites; and (3) mass transfer of CO_2 and CO inside the electrode pores. As a result, three categories-activation polarization, ohmic polarization, and concentration polarization-could be used to describe the polarization phenomena.

- **Activation polarization**

The restricted catalytic activity of the electrode materials, which frequently takes precedence when the applied voltage is relatively low, is the primary reason for the activation polarization [9]. Typically, the main tool for interpreting the phenomena of activation polarization is the Butler-Volmer (B-V) equation.

$$i = i_0 \left[exp\left(\frac{\beta z F \eta}{RT}\right) - exp\left(-\frac{(1-\beta) z F \eta}{RT}\right)\right] \tag{9}$$

where i is the electrolysis current, i_0 the exchange current, η the activation overpotential, z the number of charges transferred, and β the charge transfer coefficient. The activation overpotentials for anode and cathode can be derived as:

$$\eta_{act,a} = \frac{RT}{2F} \sinh^{-1}\left(\frac{i}{2i_{0,a}}\right) \tag{10}$$

$$\eta_{act,c} = \frac{RT}{2F} \sinh^{-1}\left(\frac{i}{2i_{0,c}}\right) \tag{11}$$

- **Ohmic polarization**

The barrier to the movement of oxygen ions (oxygen vacancies) and electrons between the parts

of the cell is what causes the ohmic polarization. The ohmic resistance of the electrolyte makes up a considerable portion of the overall ohmic resistance since the ionic conductivity is often much lower than the electronic conductivity. High ionic conductivity electrolytes are desired, and the electrolyte layer should be as thin as possible to minimize ohmic polarization. The ohmic overpotential is calculated by:

$$\eta_{omic} = i.R_{\Omega} \tag{12}$$

where R_{Ω} is ohmic resistance.

- **Concentration polarization**

When the electro-reduction process proceeds more rapidly than the gaseous reactants' mass transfer, concentration polarization occurs. Once mass transfer has taken control of the entire reaction, the current density stops rising with the voltage applied and instead stays constant. The gaseous transport rate may be constrained by porous electrode structure, particularly the micrometer-size-pores where gas transports through the Knudsen diffusion predominates, which is typical in SOEC electrodes. In contrast to other reactants like H_2 and H_2O, CO_2 molecules are big and more difficult to adsorb. As a result, such phenomena can be rather prevalent for CO_2RR. On the other hand, because the reaction rate is often relatively low even at a high voltage, CO_2 diffusion is seldom the governing mechanism. The concentration polarization at cathode and anode are expressed in Eqs. 13-14, respectively.

$$\eta_{con,c} = \frac{RT}{2F}\ln\left(\frac{1 + (RTid_c/2FD_{CO_2}^{eff}P_{Co}^{0})}{1 - (RTid_c/2FD_{CO_2}^{eff}P_{CO}^{0})}\right) \tag{13}$$

$$\eta_{con,a} = \frac{RT}{4F} ln \left(\frac{\sqrt{(RTi\mu d_a / 2FB_g) + \left(p^0_{O_2}\right)^2}}{p^0_{O_2}} \right) \quad (14)$$

where D^{eff} is effective diffusion coefficient, B_g is the flow permeability, μ is dynamic viscosity, and d is thickness of the electrode (anode or cathode).

2.3 Electrolyte and Air Electrode Materials for Solid Oxide Cells

The performance of solid oxide cells (SOCs) is heavily influenced by the choice of electrolyte and air electrode materials. An ideal electrolyte must exhibit high ionic conductivity (>10^{-2} S/cm) and negligible electronic conductivity across the operating temperature range [10,11]. Yttria-stabilized zirconia (YSZ) is the most widely used electrolyte due to its structural stability and moderate oxygen ion conductivity (~0.03 S/cm at 800°C [10]). However, its performance decreases at intermediate temperatures (<700°C) [12]. Alternatives such as scandia-stabilized zirconia (ScSZ) offer higher conductivity (~0.128 S/cm at 800°C) but suffer from high cost and limited availability. Doped ceria electrolytes (e.g., GDC or SDC) provide excellent ionic conductivity at intermediate temperatures but exhibit electronic leakage due to their mixed ionic electronic conductors (MIEC) characteristics, and low mechanical strength, limiting their use [11].

$LaGaO_3$-based perovskites, such as $La_{0.9}Sr_{0.1}Ga_{0.8}Mg_{0.2}O_{3-\delta}$ (LSGM), demonstrate superior ionic conductivity (~0.12 S/cm at 800°C [13]), making them promising electrolyte candidates. However, challenges such as Ga_2O_3 volatilization and reactivity with Ni-based electrodes necessitate the use of buffer layers like doped ceria. Other materials, including Bi_2O_3-based oxides and apatite-type lanthanum silicates, offer high conductivity but face issues related to stability or sintering requirements [12].

Air electrodes in SOCs must facilitate oxygen reduction (ORR) in SOFC mode and oxygen

evolution (OER) in SOEC mode, requiring both high catalytic activity and mixed ionic–electronic conductivity [12]. Lanthanum strontium manganite (LSM) is commonly used due to its compatibility with electrolytes, but its limited ionic conductivity necessitates the use of composite electrodes with ionic conductors like YSZ [12]. Advanced air electrode materials such as double perovskites (e.g., PBCC) and Ruddlesden–Popper (RP) oxides (e.g., $La_2NiO_{4+\delta}$, $Pr_2NiO_{4+\delta}$) have garnered interest due to their high oxygen mobility, ORR activity, and thermal stability. These materials feature layered structures that promote fast oxygen diffusion and are considered strong candidates for next-generation SOC cathodes [12]. Lanthanum strontium cobalt ferrite (LSCF) is a widely adopted MIEC material with excellent oxygen transport properties, though it is chemically incompatible with YSZ and requires a GDC interlayer to prevent degradation [11].

In this work, LSGM is selected as the electrolyte material due to its high oxygen ion conductivity and full ionic conduction across a wide range of oxygen partial pressures. For the anode electrode, a composite of $La_{0.6}Sr_{0.4}Cr_{0.5}Fe_{0.5}O_{3-\delta}$ (LSCF) and Gd-doped ceria (GDC)—referred to as LSCF/GDC—is utilized. This composite benefits from the mixed ionic and electronic conductivity of LSCF, while the addition of GDC enhances the ionic transport and improves interfacial compatibility with the LSGM electrolyte.

2.4 Cathode (fuel electrode) materials for SOEC

One of the fuel electrode's main functions is to provide reaction sites and to catalyze the electrochemical reaction of the fuel. As a result, the fuel electrode must be stable in a reducing atmosphere and possess a high level of electronic conductivity and catalytic activity [14]. The fuel electrode material must also have a thermal expansion similar to that of the other components of the cell, as it operates at high temperatures (700-850 °C). To facilitate the diffusion of fuel gas to the three-phase interface, the fuel electrode for the SOEC must also be porous. Fuel electrode

materials for high temperature SOECs consist primarily of precious metals, electronic conductive ceramics, and mixed conductor oxides. Nickel, copper, and precious metals are commonly used as fuel electrode materials, but they face limitations such as thermal instability, corrosion at high temperatures, and high cost or scarcity. These issues lead to performance degradation, making pure metals less ideal for long-term SOEC operation. To overcome these challenges, fuel cells often use alloys or composite materials that combine the benefits of different metals while minimizing their drawbacks. Researchers have then mixed the metal Ni with the YSZ (Yttria Stabilized Zirconia) electrolyte to make a composite anode [15] and they have been using it ever since. A typical fuel electrode mainly includes Ni-based cermet anodes, Cu-based anodes, and calcium titanium oxide anodes. Among them, Ni-based fuel electrodes have high catalytic activity and are relatively inexpensive [16]. However, cermet cathodes such as Ni-YSZ are prone to coke deposition during CO_2 electrolysis. As such, there has been efforts to develop alternative cathode material like perovskites.

2.4.1 Perovskites

Since the 1950s, research on perovskite materials has expanded quickly and is now being conducted in many areas of science and engineering. Perovskite materials typically have a structure of ABX_3 where A and B represent cations, and X is the anion. The large A-site cations occupy the 12-fold sites, while the B-site cations and oxygen ions form the BX_6 octahedra at the corners, as shown in Figure 2.3. Since the perovskite structure deviates from the ideal cubic structure due to the varied arrangement of BX_6 octahedra, the BX_6 octahedra defines the primary structural properties of the perovskites. However, the functional properties of perovskites are influenced by cationic and anionic defects, cation and anion stoichiometry, doping, synthesis method, etc.

Lanthanide (such as La, Pr, Sm, Gd, Nd, etc.) metal ions or alkaline earth (Ca, Sr, Ba) metal ions occupy the A-site and transition metal ions (such as Mn, Fe, Co, Ni, etc.) occupy the B-site. The perovskite structure's structural integrity is provided by the A-site ion, while its characteristics, such as electrocatalytic activity, electronic conductivity, etc., are determined by the B-site ion. The advantage of such a unique structure is that the physical and chemical properties of the material can be adjusted by doping a broad range of elements [17]. A-site and B-site elements may be partially replaced with many different combinations of other elements without changing their crystal structure. Different functionalities that cannot be achieved by a single oxide material or their combinations can be brought about by the presence of many such ions in the same lattice. Oxide perovskites, where X is oxygen, are distinctive in their oxygen vacancies. Significant changes in a material's characteristics are brought on by the existence of oxygen vacancies in perovskite oxides; these changes are seldom seen in oxides with other structures. Doping is one way to change the oxygen vacancies in perovskite oxides. Besides that, perovskite has a mixed ionic-electronic conductivity (MIEC) that makes it a suitable replacement for traditional electrode martial. The other advantage of the perovskite is that it increases the active sites of the metal-oxide-gas TPBs (Triple Phase Boundaries) in cermet electrodes to the oxide-gas interface on the entire surface of the perovskite. Perovskites have good redox stability, a fine catalytic impact on fuel oxidation, and may successfully suppress the hydrocarbon fuels' tendency to deposit carbon in the fuel electrode [18]. The overall valence states of the ions at positions A and B change when they are partially replaced by other ions, which changes the valence states of transition metal ions or causes oxygen vacancies to form in the crystal lattice, giving the substance a specific oxygen ion conductivity.

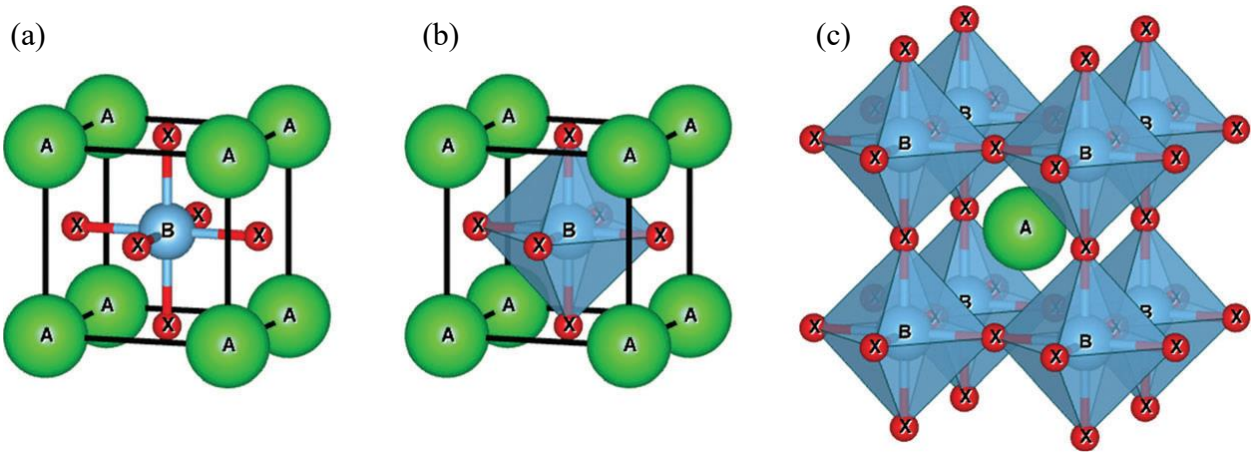


Figure 2.3. Perovskite ABX_3 lattice. (a) Large A and small B cations, with X anions; (b) octahedron by X anions; (c) octahedra lattice. Reprinted with permission from [19]. Copyright 2020 Taylor & Francis.

In terms of structure, perovskite can be categorized into the following three groups:

1) Single perovskite: there is no order in the structure of the octahedra, as shown in Figure 2.4(a). In contrast to complex perovskites, single perovskites can be synthesized easily at low temperatures, and their properties can easily be modified by doping.

2) Double perovskite: a doubled lattice spacing is produced by two different types of octahedra, as shown in Figure 2.4(b). The presence of two property-determining B-site cations is likely to show superior properties than ABX_3 perovskite materials, especially among the halide perovskites for opto-electronic applications [19].

3) Layered perovskite: the octahedra can create a layered structure, as seen in Figure 2.4(c). The Ruddlesden-Popper phase, the Dion-Jacobson phase, the Aurivillius phase, and the $A_nB_nO_{3n+2}$ layered phase are further classifications for the layered perovskites. Since the present work is concerned with the use of double perovskite as fuel electrode, the following section will describe in more detail only the double perovskite [19].

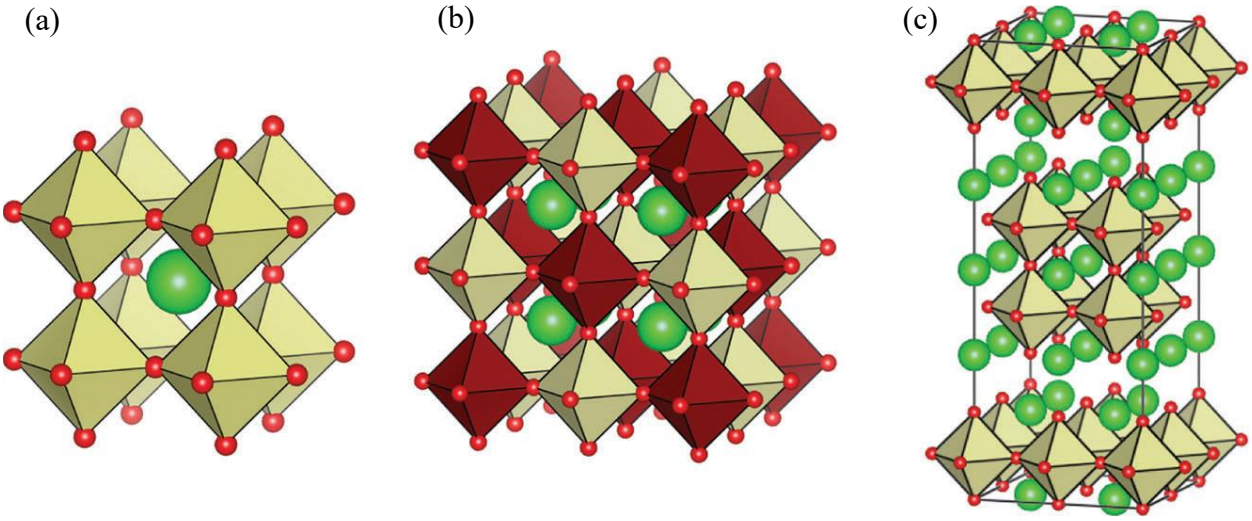


Figure 2.4. Crystal structures of: (a) Single perovskite; (b) double perovskite; (c) layered perovskite. Reprinted with permission from [19]. Copyright 2020 Taylor & Francis.

2.4.2 Double perovskite

Double perovskites often have the general formulae $A'A''B_2O_6$ (double A-site), $A_2B'B''O_6$ (double B-site), or $A'A''B'B''O_6$ or have A- and B-lattice sites filled by more than two different types of ions (mixed site). The arrangement of the A′, A″ or B′, and B″ cations in the corresponding lattices determines the crystal structure of double perovskites. If the size difference between A′ and A″ or B′ and B″ cations is large, then such an arrangement is important. In typical double perovskite structures, three types of ordering can be observed depending on the cation at either the A- or B-site. When the B′ and B″ cations are occupied in the same places, the rocksalt structure (Figure 2.5(a)), which is the most symmetrical, is created. As illustrated in Figure 2.5(a), the B′ and B″ octahedra in the rocksalt structure are all alternately separated from one another, which is known as zero-dimensional ordering. As shown in Figure 2.5(b) and (c), the cations can also adopt layered or columnar ordering, which correspond to one- or two-dimensional ordering, respectively. The $A'A''B_2O_6$ perovskite structures, depicted in Figure 2.6, show A-site ion ordering similarly. Such ordering happens in double perovskite structures and is influenced by the size of the A-site ions in

A′A″BO_6 perovskites as well as the general difference in charge of the B-site cations.

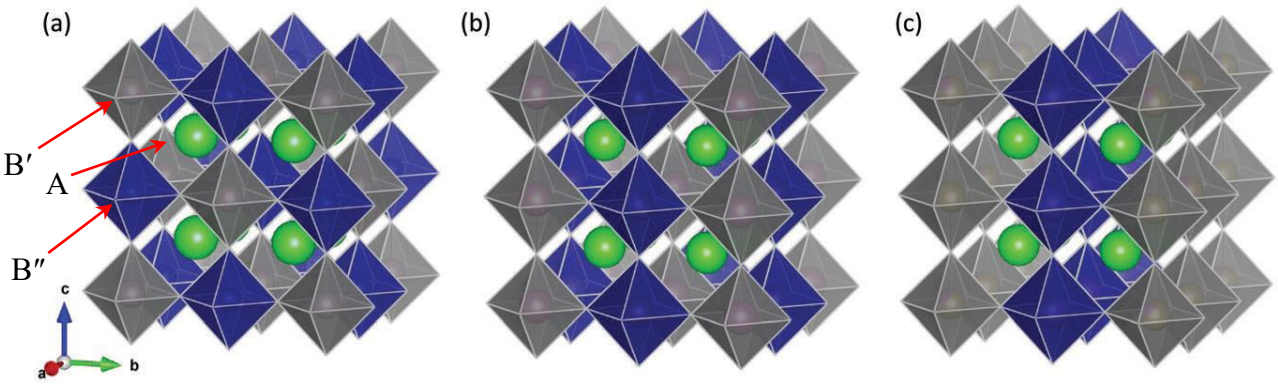


Figure 2.5. Ordering of BO_6 octahedra in $A_2B'B''O_6$ double perovskites: (a) zero-dimensional or rocksalt type, (b) one-dimensional or columnar, and (c) two-dimensional or layered. Reprinted with permission from [19]. Copyright 2020 Taylor & Francis.

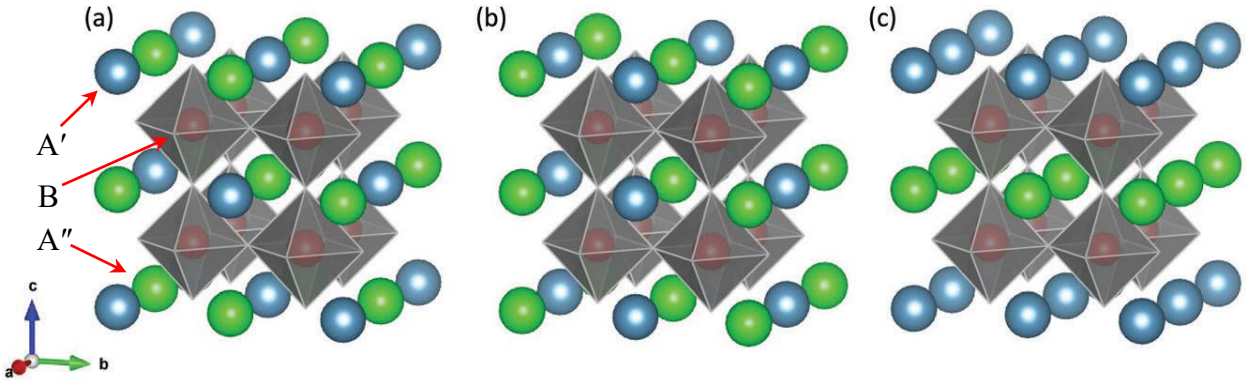


Figure 2.6. Ordering of A-site ions in A′A″B_2O_6 double perovskites: (a) zero-dimensional or rocksalt type, (b) one-dimensional or columnar, and (c) two-dimensional or layered. Reprinted with permission from [19]. Copyright 2020 Taylor & Francis.

2.5 CO_2 electrolysis using double perovskite as fuel electrode

Perovskite materials possess mixed ionic-electronic conductivity and good chemical stability. Among perovskites that have been used in SOEC, $Sr_2Fe_{1.5}Mo_{0.5}O_{6-\delta}$ (SFM) has attracted much attention [20]. SFM has notable conductivity and redox stability, and it is frequently recommended as the electrode CO_2 electrolysis in SOEC [20]. While SFM is thermally and chemically more

robust, especially for CO_2 electrolysis, its catalytic activity, CO_2 adsorption capability, and long-term phase stability still need to be enhanced—especially when compared to the conductivity and catalytic strength of Ni-based cathodes [21]. Researchers have explored a variety of techniques recently to increase its electrocatalytic activity for CO_2 electrolysis, including the infiltration technique, doping, and in-situ exsolution. A cathode made of $Sr_2Fe_{1.5}Mo_{0.5}O_{6-\delta}$ (SFM) deposited on a YSZ scaffold was investigated by Li et al [22]. Their results showed that the SFM-YSZ ceramic performed very well in comparison with traditional Ni-YSZ cermet that needs safe gas. The cell achieved 1.1 A/cm^2 at 1.5 V and 800 °C, which is higher by one order of magnitude than other reported perovskite ceramics prior to 2016. The use of $Sr_2Fe_{1.5}Mo_{0.5}O_{6-\delta}$ (SFM) for pure CO_2 electrolysis without using any safe gas was presented for the first time in 2017 by Li et al. [23]. They used LSGM as the electrolyte, which resulted in a current density of 0.71 A/cm^2 at 1.5 V and 800 °C. They further improved their performance by introducing SFM-$Sm_{0.2}Ce_{0.8}O_{2-\delta}$ (SFM-SDC) composite material. The performance peaked at 1.09 A/cm^2 for the same operating conditions, proving that SFM is a promising fuel electrode for CO_2 electrolysis. Lv et al. [24] proposed a composite of SFM and $Gd_{0.2}Ce_{0.8}O_{1.9}$ (GDC) to increase the activity for CO_2RR. The GDC infiltrated SFM reached 0.45 A/cm^2 at 1.6 V and 800 °C which is higher than the standalone SFM (0.283 A/cm^2). The extended TPBs lengths, additional active sites for CO_2 adsorption and electro-reduction, and improved oxygen ion transport capabilities are the results of the GDC infiltration. Xi et al. [25] investigated the effect of composition of the B-site of the double perovskite $Sr_2Fe_{1+x}Mo_{1-x}O_{6-\delta}$ on the performance of the CO_2 electrolysis cell. They found a current density of 1.5 A/cm^2 at 1.5 V and 800 °C, which is comparable to the present state-of-the-art Ni-based catalysts. The findings showed adding more Fe to $Sr_2Fe_{1+x}Mo_{1-x}O_{6-\delta}$ improved the reaction kinetics.

- **Symmetrical cells**

In the above reported studies, the SOEC cathode and anode were made of different materials, but double perovskites have also been used in symmetrical cells, which would ease the fabrication process and render them suitable for reversible SOFC/SOEC cells. Li et al. [26] proposed a symmetrical cell consisting of $La_{0.9}Sr_{0.1}Ga_{0.8}Mg_{0.2}O_{3-\delta}$ (LSGM) as the electrolyte and SFM deposited on LSGM as electrodes. With a current density of 1.24 A/cm^2 at 1.5 V and 800 °C, the cell proved to be a promising option for electrolyzing CO_2, and this might be due to the enlarged active sites produced by infiltrated Sr_2FeMoO_6 (SFM) nanoparticles. Wang et al. [27] presented a symmetrical SFM-SDC/LSGM/SFM-SDC cells that were used in a high temperature H_2O/CO_2 co-electrolysis process to produce syngas, and the results showed good electrochemical performance with an electrolysis current density of 0.73 A/cm^2 under 1.3 V at 850 °C. By raising the operating temperature and applied cell voltage, improved co-electrolysis kinetics, including an increase in electrolysis current density and a decrease in interfacial polarization resistance, were achieved. With a variety of B-site cation options in a wide range of compositions, $Sr_2Fe_{1.5}Mo_{0.5}O_{6-\delta}$ as the cathode material offers flexibility in adjusting their attributes. A metal-ceramic composite was produced by Hou and Xie [28] where the B-site of $Sr_2Fe_{1.5}Mo_{0.5}O_{6-\delta}$ was doped with 10% Fe. The in-situ generated Fe-ceramic composite cathode offers a large and effective triple-phase boundary (TPB) for the H_2O/CO_2 co-electrolysis process after being reduced. The current density of the symmetrical cell reached 1.27 A/cm^2 at 1.6 V and 850 °C for $Sr_2Fe_{1.6}Mo_{0.5}O_{6-\delta}$, which in case of $Sr_2Fe_{1.5}Mo_{0.5}O_{6-\delta}$ was 1.02 A/cm^2. Xu et al. [29] studied the catalytic properties and reaction kinetics of CO_2 on PBCO ($PrBaCo_2O_{5.5+\delta}$) surfaces for a symmetrical PBCO/YSZ/PBCO cell. The CO_2 reaction behavior on the PBCO electrode was investigated using electrochemical impedance spectroscopy. The surface resistance of CO_2 on PBCO is around 30 Ω.cm^2, which suggests that

PBCO might be a desirable choice for CO_2 reduction. Niu et al. [30] studied a symmetrical cell with structure of STC02F/LSGM/STC02F with STC02F as $Sr_2Ti_{0.8}Co_{0.2}FeO_6$. They performed in-situ exsolution of cobalt-iron nanoparticles on the fuel electrode. Their results showed a current density of 0.5 A/cm^2 at 1.3 V and 800 °C.

- **B-site doping**

Doping SFM with foreign elements to change the defective system and the crystal structure is another method to improve its electrical conductivity and electrocatalytic activity. Jiang et al. [31] aimed at examining the impact of partial Fe substitution by Mn in SFM (to generate $Sr_2Fe_{1.4}Mn_{0.1}Mo_{0.5}O_6$ (SFMM0.1)) on its efficiency as a cathode material for CO_2 electrolysis with the goal of accelerating the rate of CO_2 reduction. At 800 °C and 50% CO/CO_2, the polarization resistance falls from 1.15 $\Omega.cm^2$ for SFM to 0.60 $\Omega.cm^2$ for SFMM0.1. Under the same conditions, the polarization resistance of a symmetrical cell with dual-phase SFMM0.1-SDC (samaria-doped ceria) electrodes drops even further to 0.50 $\Omega.cm^2$. When SFMM0.1-SDC is integrated as the cathode in a solid oxide cell for electrolysis of pure CO_2, higher performance is shown, obtaining a current density of 1.35 A/cm^2 at 800 °C at 1.5 V. Xu et al. [32] proposed Cu-doped SFM as a novel material for cathode. The $Sr_2Fe_{1.3}Cu_{0.2}Mo_{0.5}O_{6-\delta}$ (SFCM) had a lower polarization resistance of 1.125 $\Omega.cm^2$ in comparison of 1.834 $\Omega.cm^2$ for SFM. In principle, using Cu as dopant increased the oxygen vacancies in the B-site of the SFM perovskite, which dramatically increased the chemical adsorption capacity of carbon dioxide at high temperatures. The interaction between CO_2 molecules and oxygen vacancies was improved by the higher concentration of oxygen vacancies, which also provided more area for CO_2 adsorption. Xi et al. [33] tested the $Sr_2FeMoO_{6-\delta}$ (SFM) as the cathode materials for CO_2 electrolysis by substituting Mo partially with Mg. They found that by doping Mg more oxygen vacancies are formed after reduction and subsequently increasing the

electrochemical performance with 1.4 A/cm^2 at 800 °C and 1.5 V, which two times higher than simple SFM.

- **A-site doping**

B-site doping has been well explored in literature due to successful improvement in cell performance. A-site doping, however, has not been thoroughly researched and a limited number of research papers were found on A-site doping of SFM perovskite for CO_2 electrolysis. A-site doping can influence the crystal structure, oxygen vacancy concentration, and overall stability of the perovskite, thereby impacting its ionic and electronic conductivity. Recent studies have tried to enhance the performance by doping rare-earth and alkaline-earth metals on the A-site. For example, Sun et al. [34] investigated the performance of doping La on the $Sr_2Fe_{1.5}Mo_{0.5}O_{6-\delta}$ perovskite. The results showed that $Sr_{1.9}La_{0.1}Fe_{1.5}Mo_{0.5}O_{6-\delta}$ with the LSGM as the electrolyte could achieve current density of 2.76 A/cm^2 at 850 °C and 1.5 V, which is higher than non-doped SFM. This is because La-doping enhances the oxygen surface exchange rate as well as the bulk diffusion coefficient. Yang et al. [35] studied the effect of doping Bismuth on the A-site of SFM perovskite as the cathode for CO_2 electrolysis. By partially replacing Sr with Bi, the modified SFM showed better CO_2 adsorption and improved oxygen ion conductivity. The cell delivered a high current density of 1620 mA cm^{-2} at 1.6 V and 850 °C.

- **Exsolution**

When a solid solution is formed by mixing two or more components, the atoms of each element are uniformly distributed within the crystal lattice. However, under certain conditions—such as cooling, compositional changes, or changes in temperature and pressure—one of the components may become insoluble, leading to the formation of a separate phase within the structure [36]. The newly formed phase will often have a different composition, crystal structure, and physical

properties compared to the original solid solution. This can lead to a range of interesting properties and applications, such as improved mechanical strength, enhanced catalytic activity, and increased conductivity [36]. Exsolution of transition metal particles from the base double perovskite cathode can lead to a promising electrode with enhanced CO_2 catalytic activation. Li et al. [37] studied the effect of adding Ni-Fe nanoparticles into SFM-SDC uniformly. The chemical adsorption of CO_2 and the kinetics of its surface reactions were both improved by the exsolved NiFe nanoparticles. With a 1.5 V applied voltage at 800 °C, SOECs using this unique cathode have shown a peak current density of 2.16 A/cm^2 and consistent CO_2 electrolysis performance for 500 hours. To effectively accelerate the CO_2RR in SOECs, in situ exsolved Fe–Ni nanoparticles on a $Sr_2Fe_{1.35}Mo_{0.45}Ni_{0.2}O_6$ (SFNM) double perovskite substrate (Fe–Ni@SFNM) have been developed by Lv et al. [38]. The SOEC with the Fe–Ni@SFNM-GDC ($Gd_{0.2}Ce_{0.8}O_{1.9}$) cathode exhibits great stability and no coke deposition for 40 h at 1.2 V, as well as a current density of 0.934 A/cm^2 at 1.6 V and 800 °C. During the synthesis procedure, nickel was added to the B-site of $Sr_2Fe_{1.5}Mo_{0.5}O_6$ to create a stoichiometric $Sr_2Fe_{1.35}Mo_{0.45}Ni_{0.2}O_6$ (SFNM) double perovskite oxide. Using a high-temperature reduction process, Fe–Ni alloy nanoparticles were exsolved in place and equally anchored on the perovskite surface while the double perovskite kept its original structure. Lv et al. [39] showed that metallic Co can be exsolved from the parent perovskite in a reducing environment, resulting in the creation of cation defects and oxygen vacancies. Metallic Fe may subsequently be exsolved to produce CoFe alloy nanoparticles in SFMC, along with the structure changing from double to layered perovskite at 800 °C. At 600 °C in an oxidizing environment, the spherical CoFe alloy nanoparticles are first converted to flat $CoFeO_x$, then at 800 °C, the structure is changed back to double perovskite while being entirely dissolved back into the bulk. Due to the synergistic impact of CoFe alloy nanoparticles and plentiful oxygen vacancies at the metal-oxide

interfaces, the SFMC cathode decorated with CoFe alloy nanoparticles exhibits 1.2 A/cm^2 at 1.6 V and 800 °C which is 50% higher than the parent cathode of SFMC. Chen et al. [40] prepared a double perovskite of $Sr_2Fe_{1.5+x}Mo_{0.5}O_{6-\delta}$ with exsolved Fe nanoparticles. This type of in-situ generated Fe nanoparticles offers a method for creating a metal-oxide three-phase boundaries to improve electro-catalysis activity. Their cell with the structure of $SF_{1.5+x}M$-SDC/LSGM/LSM-SDC showed a current density of 1.16 A/cm^2 at 1.8 V and 850 °C. Zhang et al [41] investigated the stability issued of exsolved nanoparticles on the SFM perovskite. Although the nanoparticles make the material performs better, they are unstable at high voltages. Zhang et al. found out the B-site vacancies are the primary cause of the degradation. Therefore, they supplemented the perovskite with external Fe. The results showed that the supplemented SFNM had better catalytic activity and less degradation. Xi et al. [42] explored the exsolution of bimetallic nanoparticles of Fe-Cu on the SFM perovskite. This was done by doping Cu on the SFM structure and then performing reduction treatment. Results showed a current density of 2.5 A/cm^2 at 1.5 V and 800 °C, which was higher than 1.6 A/cm^2 for unreduced electrode. Lv et al. [43] developed a redox-induced redispersion strategy to create RhO_x nanoclusters on SFM. In this method, the material is reduced to create the nanoparticles of RhFe and then oxidized again to selectively dissolve the iron species and keep the RhO_x clusters on the surface. The results showed 45.9% improvement in the performance of CO_2 electrolysis. Zhang et al. [44] investigated the performance improvement of SFM perovskite by co-doping Ni on B-site and Fluorine on oxygen site. Ni doping introduced Ni-Fe nanoparticles on the surface while F doping improved bulk properties. The results showed that doping reduced the polarization resistance from 0.64 to 0.31 Ω cm^2, and a current density of 2.66 A/cm^2 (800 °C, 1.5 V). Zhang et al. [45] investigated the performance of double perovskite and layered perovskite of SFM with nanoparticles exsolved. By introducing a B-site iron supplement

strategy, the authors successfully promote nanoparticle exsolution while preserving the perovskite scaffold, breaking the traditional trade-off. Double perovskite-based nanoparticles (DP-NPs) showed the highest activity, while layered perovskite-based nanoparticles (LP-NPs) offered superior stability. Shen et al. [46] explored the benefit of doping SFM with iridium. The prepared powder was then reduced to form IrFe nanoparticles onto the SFM surface. The results showed a current density of 1.46 A/cm^2 for IrFe@SFIrM and 1.16 A/cm^2 for SFM at 1.6 V, which shows an improvement of 25.8%. Hu et al. [47] proposed a novel strategy of dual-exsolution of nanoparticles on a composite electrode made of SFM and GDC. The cell delivered 1.72 A/cm^2 at 1.5 V for CO_2RR, which is almost double that of SFM/GDC electrode with no nanoparticles. Liu et al. [48] studied the effect of doping zinc on Fe-sites of SFM to improve the Fe nanoparticles exsolution and ultimately increase the CO_2RR performance. The cell achieved a high current density of 2.74 A/cm^2 at 850 ℃ and 1.6 V while for SFM with no nanoparticles it was 1.42 A/cm^2. Tan et al. [49] presented a high-performance solid oxide electrolysis cell (SOEC) cathode composed of $Pr_{0.4}Sr_{1.6}(NiFe)_{1.5}Mo_{0.5}O_{6-\delta}$ (PSNFM) double perovskite, decorated with exsolved NiFe/FeO_x (NFA@FeO) core-shell nanoparticles. The in-situ exsolved particles and generated oxygen vacancies significantly enhanced CO_2 adsorption and reduction activity. As a result, the cell achieved a high current density of 1.58 A/cm² at 1.4 V and 800 °C. López-García et al. [50] explored a double perovskite, $Sr_xFeCo_{0.2}Ni_{0.2}Mn_{0.1}Mo_{0.5}O_{6-\delta}$ (x = 2.0, 1.9, 1.8), as a cathode material for solid oxide electrolysis cells (SOECs). It demonstrates the formation of tunable Fe–Co–Ni ternary alloy nanoparticles via in situ exsolution, influenced by reduction temperature and A-site stoichiometry. Exsolution at 600 °C resulted in smaller, more abundant nanoparticles and better CO_2 electrolysis performance than higher-temperature treatments, which led to RP phase formation. The x = 2.0 composition showed superior nanoparticle formation and conductivity.

These findings highlight the potential of tailored alloy nanoparticle exsolution for enhancing SOEC efficiency and broader energy conversion applications.

Exsolution has emerged as a highly promising strategy for enhancing electrode performance in solid oxide electrolysis cells (SOECs). Unlike conventional infiltration methods, exsolved nanoparticles are socketed into the perovskite matrix, offering excellent thermal stability and strong metal-support interaction. This approach not only prevents particle agglomeration under harsh conditions but also introduces abundant active sites and oxygen vacancies, significantly boosting catalytic activity and long-term durability. As such, exsolution provides a robust pathway to develop next-generation SOEC electrodes with improved efficiency and stability for CO_2 electrolysis and related energy conversion applications.

Chapter 3

Experimental Methodology

In this section, the complete experimental procedures employed in this study are described in detail. It covers the synthesis of cathode powders using the sol–gel method, followed by subsequent processing steps for doping and nanoparticle exsolution. The fabrication of the full solid oxide electrolysis cell (SOEC), including electrolyte preparation, electrode deposition, and sintering processes, is also presented. Furthermore, the section outlines the characterization techniques used to analyze the structural, morphological, and electrochemical properties of the materials and cells, such as X-ray diffraction (XRD), scanning electron microscopy (SEM), electrochemical impedance spectroscopy (EIS), and current–voltage measurements. This detailed methodology ensures that the experimental approach is transparent, reproducible, and directly linked to the performance evaluation discussed in the subsequent results sections.

3.1 Perovskite powder synthesis

Powders are synthesized using sol–gel method. The sol–gel method is a wet-chemical synthesis technique used to produce ceramic or glassy materials from a solution. In this process, a homogeneous solution (sol) containing metal precursors is first prepared. Through hydrolysis and polycondensation reactions, the sol gradually transforms into a gel, which is a three-dimensional network containing both solid and liquid phases. The gel is then dried and calcined to remove residual organics, resulting in a fine, homogeneous oxide powder with high purity and controlled stoichiometry. This method is particularly advantageous for synthesizing complex oxides because it allows mixing at the molecular level, leading to uniform particle size and excellent compositional control. The $Bi_{0.1}Sr_{1.9}Fe_{1.4}Ni_{0.1}Mo_{0.5}O_{6-\delta}$ powder synthesis procedure, shown in Figure 3.1, is as

follows:

Step 1: precursor solution preparation

Stoichiometric amounts of $Sr(NO_3)_2$, $Bi(NO_3)_3 \cdot 5H_2O$, $Fe(NO_3)_3 \cdot 9H_2O$, $Ni(NO_3)_2 \cdot 6H_2O$ and $(NH_4)_6Mo_7O_{24} \cdot 4H_2O$ (all purchased from Fisher Scientific) were dissolved in distilled water under continuous magnetic stirring to ensure complete dissolution and homogeneity of the cation mixture. The volume of distilled water used to dissolve the metal nitrates was selected based on the solubility limits of each precursor and the required stoichiometric quantities. The total water volume V_{total} was taken as the sum of the individual minimum volumes with an added safety margin (typically 20–30%) to ensure complete dissolution and easy stirring. A sample calculation is presented in Table A.1 in Appendix.

Step 2: chelating and complexation

EDTA was added to distilled water under constant stirring. The mixture was then heated to 80 °C, after which aqueous ammonia was slowly added until the EDTA particles were completely dissolved. The pre-prepared EDTA–NH_3H_2O solution was added to the precursor solution to chelate the metal ions and prevent premature precipitation. Citric acid was subsequently introduced as both a complexing agent and an additional fuel source for combustion. The molar ratio of EDTA : citric acid : total metal ions was maintained at 1:1.5:1, which promotes the formation of a stable polymeric network. Upon addition of citric acid, the solution changed to a green color with dispersed fine particles, indicating complex formation. The pH of the resulting solution was about 2.6.

Step 3: pH adjustment

NH_3H_2O was added dropwise to raise the pH value to around 8. The liquid started to become dark red and transparent after pH around 3.5. A pH of 8 was selected to ensure the complete chelation

of metal ions with EDTA and to maintain the metal–EDTA complexes in a stable, soluble form.

Step 4: gel formation

The solution was stirred and heated on a hot plate at 80 °C to promote slow evaporation of water, leading to gelation (around 12 hours). The gel ensured uniform distribution of all metal species at the molecular level, which is critical for achieving phase purity after calcination.

Step 5: combustion step

The resulting gel was transferred to a ceramic dish and placed in oven and heated up to 300 °C for 4 hours. At this temperature, an exothermic self-igniting combustion reaction occurred, decomposing nitrates and organic matter, and generating a porous, foamy precursor structure. During this process, the organic components ignite, producing noticeable smoke. Therefore, the oven should be equipped with an outlet connected to proper ventilation to ensure safe removal of the fumes.

Step 6: grinding

The porous combustion product was manually ground using an agate mortar and pestle to obtain a fine powder.

Step 7: calcination

Finally, the powder was calcined in air at 1100 °C for 5 hours (heating rate: 3 °C/min) to achieve complete crystallization of the single-phase perovskite structure.

3.2 Cell fabrication

Cell fabrication begins with preparation of the dense electrolyte substrate, followed by deposition of electrodes onto the electrolyte. The overall process is shown in Figure 3.2. Detailed procedure for each part is provided in the following subsections.

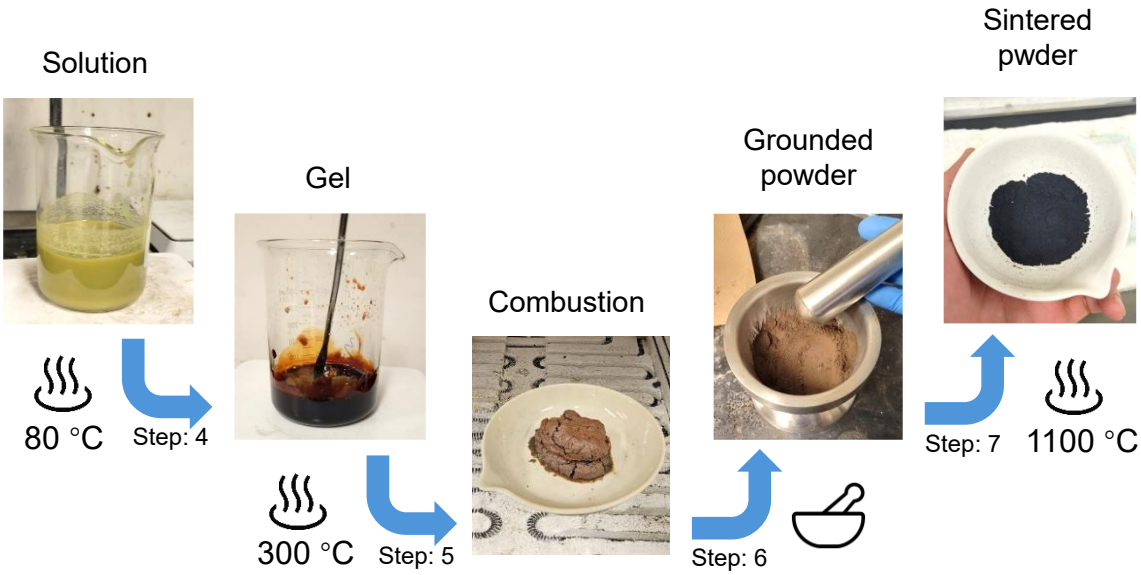


Figure 3.1. Solution combustion synthesis process followed in this research.

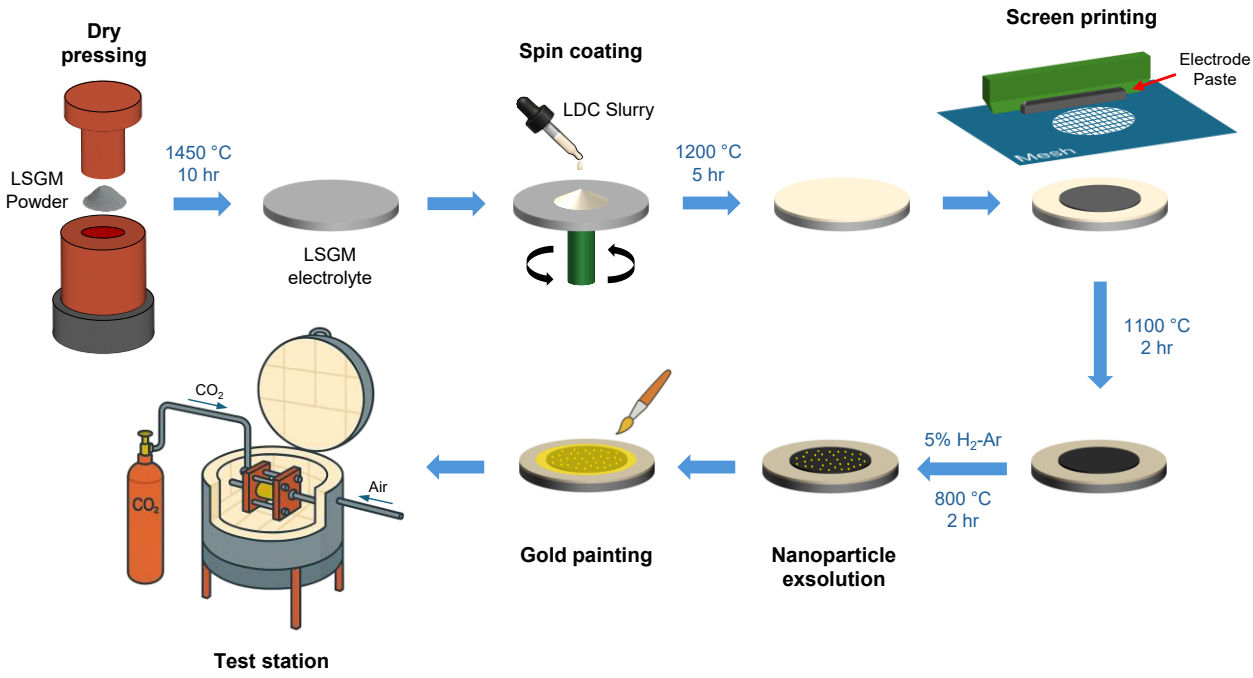


Figure 3.2. Overall cell fabrication process.

3.2.1 Electrolyte substrate

The cells used in this research are electrolyte-supported, with the electrolyte substrates fabricated using a dry pressing technique. The process of ceramic dry pressing involves placing ceramic powder into a metal mold and applying high pressure to compact the powder into a dense green body. During pressing, the particles are rearranged and brought into close contact, forming a compact with the same shape and cross-section as the mold. A schematic of dry press is shown in Figure 3.3. Dry pressing has several benefits, including a straightforward process, little labor, quick production, high densities and strengths, precise sizing and minimal shrinkage. The drawback is that the pressed product's shape is severely constrained, and the green body's internal compactness is inconsistent, and also uneven pressure distribution, density, and shrinkage, all of which contribute to the phenomena of cracking and delamination.

The LSGM electrolyte powder (purchased from Fuelcellmaterials) is uniaxially pressed at 150 MPa using a 30 mm diameter die set to form circular pellet with a thickness of 0.4 mm. The pellet was then ramped up to 1450 ℃ at 2 ℃/min and kept for 10 hours to achieve a fully dense electrolyte. The pellet shrank to a diameter of 24 mm and thickness of 0.3 mm. Figure 3.4 shows the LSGM electrolyte substrates after sintering.

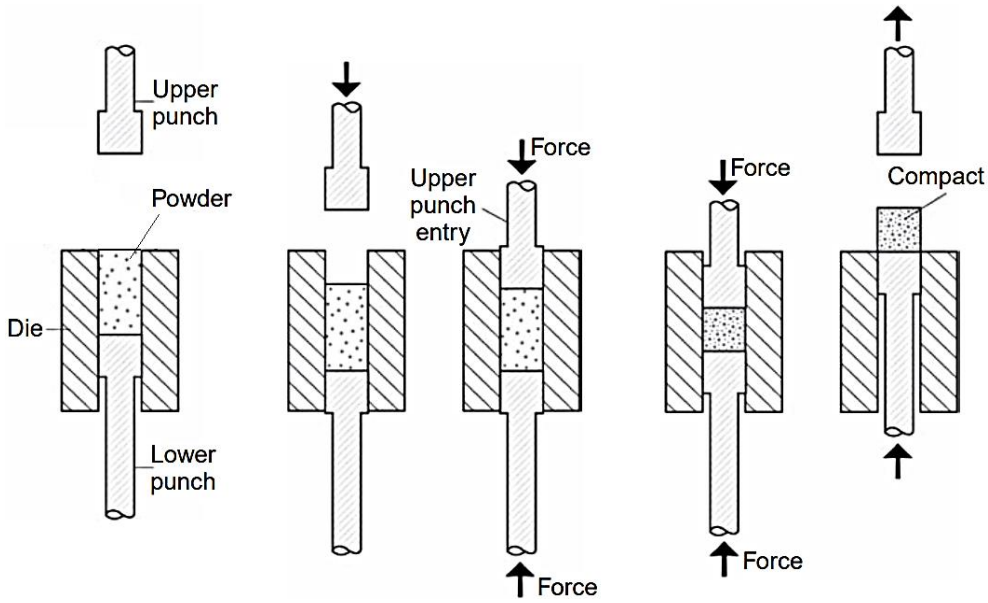


Figure 3.3. The basic principle of dry pressing. Reprinted with permission from [51]. Copyright 2009 Elsevier.



Figure 3.4. LSGM electrolyte substrates after sintering.

3.2.2 Buffer layer

The presence of Ni at the electrode-electrolyte interface can lead to undesirable reactions or interdiffusion, potentially reducing the cell performance and stability. To prevent this, a thin La-doped ceria (LDC) buffer layer must be applied between BSFNM and LSGM. The LDC layer acts as a chemical barrier, preventing such reactions while maintaining low interfacial resistance due to its high ionic conductivity and compatibility with both LSGM and perovskite-based electrodes. The LDC powder was synthesized via the same sol-gel method described in section 3.1. The powder was calcined at 1000 °C for 5 hours to form pure phase LDC. A paste was prepared by mixing the LDC powder with an ink vehicle (FuelCellMaterials) in a 1:2 weight ratio of powder to ink. The resulting paste was then spin-coated onto the LSGM substrate and sintered at 1200 °C for 5 hours to form a buffer layer prior to deposition of the BiSFMNi cathode. The electrolyte with the LDC layer (white color) deposited on it is shown in Figure 3.5.

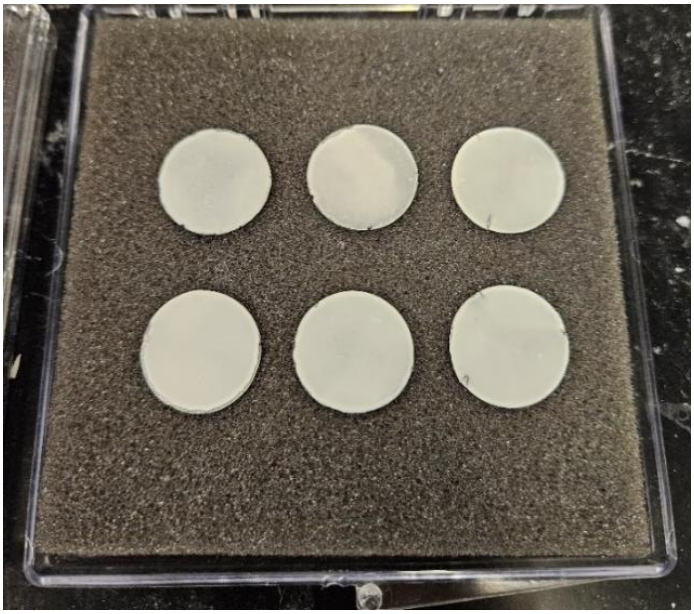


Figure 3.5. LDC buffer layer on the electrolyte substrate after sintering.

3.2.3 Electrodes

For the air electrode, a commercial LSCF/GDC paste ($La_{0.6}Sr_{0.4}Co_{0.2}Fe_{0.8}O_{3-\delta}$ mixed with GDC) was purchased from Fuelcellmaterials. The paste was used as received without further modification and directly applied onto the electrolyte substrate by screen printing. To make the cathode paste for screen printing, synthesized BiSFMNi powder was mixed with a commercially available ink vehicle (Fuelcellmaterials) in a 1:1 weight ratio and ball milled to make a paste that was smooth and easy to print. The paste was used to put the cathode layer on top of the electrolyte substrate using the screen-printing machine. In the screen-printing process, the substrate is covered with a fine-pattern mesh, and the prepared paste or ink is applied on the mesh. The paste is then forcefully pressed through a mesh with an area of 1 cm^2 using a blade to have an electrode with an active area of 1 cm^2. Depending on demand, the screen-printing layer's thickness may be adjusted. Film thicknesses of 10 to 100 µm may be produced via screen-printing. The operation of a screen-printing process and the actual screen-printing machine and the mesh are shown in Figure 3.6 and Figure 3.7, respectively.

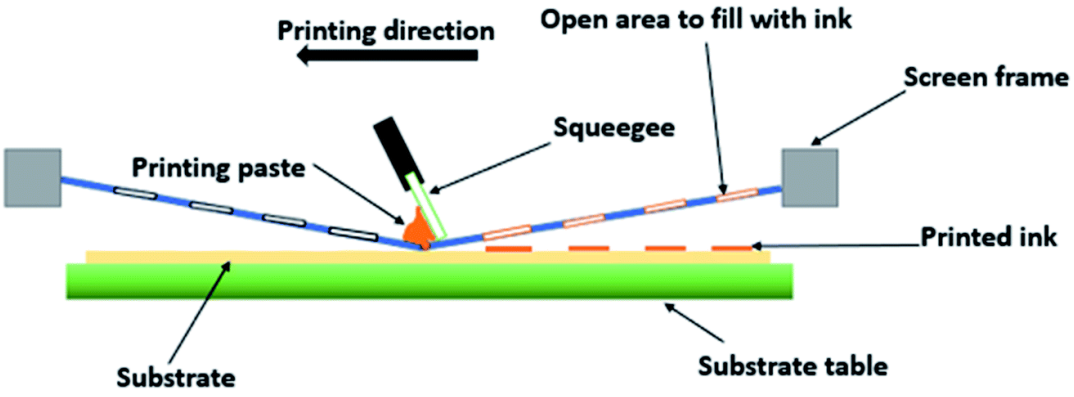


Figure 3.6. Screen printing working principle. Reprinted with permission from [52]. Copyright 2021 Royal Society of Chemistry.

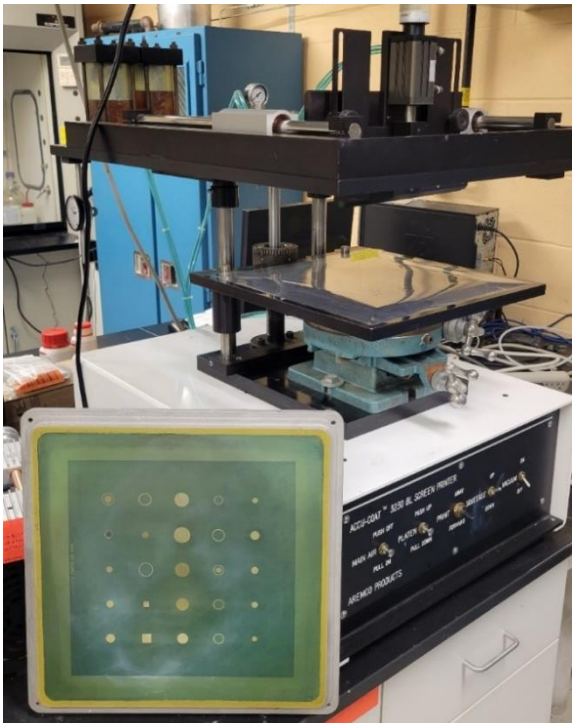


Figure 3.7. Screen printing machine and the mesh.

After screen-printing the electrodes, the cell was sintered at 1100 °C. Nevertheless, the cathode particles' adhesion to the electrolyte and to one another was weak. As demonstrated in Figure 3.8, a trace would appear on the finger even if the electrode was lightly scratched. It is believed that this inadequate adhesion is most likely due to the large particle size of the powder. Consequently, the particle size analysis shown in Figure 3.9 (a) was carried out. It revealed that the powder's median particle size was approximately 22.1 µm. To solve the issue, using a low energy ball mill with zirconia balls, the powder was ball milled 24 hours. An amount of typically 10g of powder was mixed with isopropanol in a 1:2 weight ratio of powder to isopropanol prior to milling. As shown in Figure 3.9 (b), the median particle size has been decreased to 1.7 µm. The ball milled powder was then used for screen printing and showed good contact and bond after sintering. This is most likely because smaller particles pack more densely and uniformly, promoting stronger neck formation between particles and with the electrolyte surface, which leads to improved adhesion of

the electrode layer after sintering. The single cells made by ball milled powders are shown in Figure 3.10.

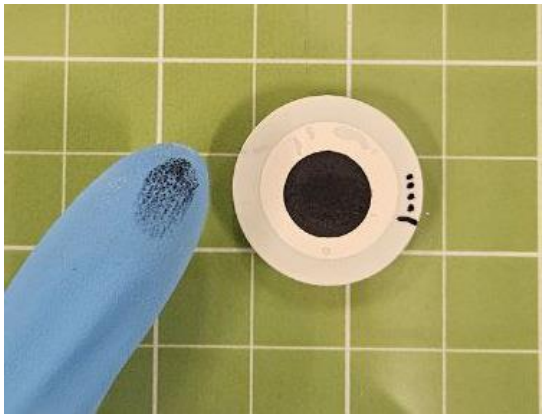


Figure 3.8. Screen printed electrode using as-prepared electrode materials showing weak adhesion.

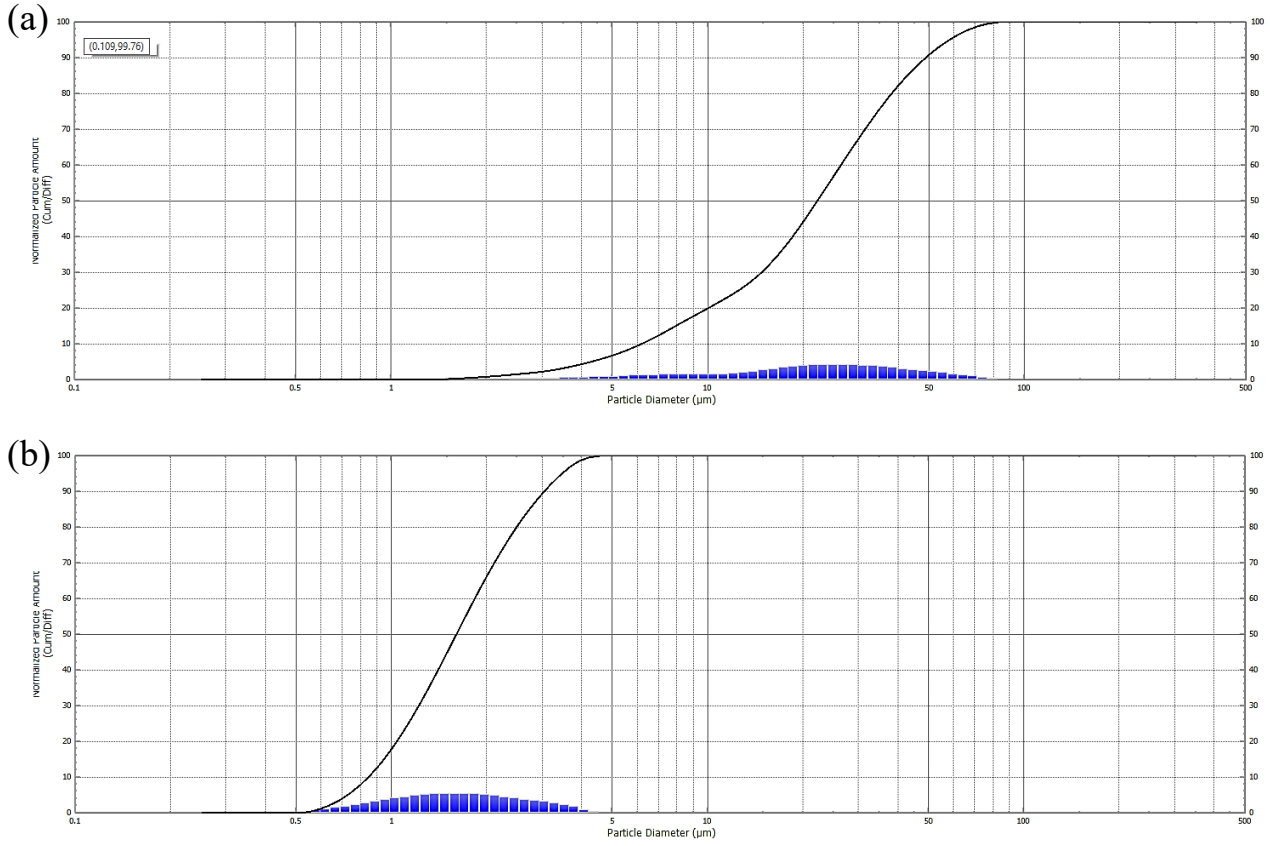


Figure 3.9. Particle size analysis of (a) as-prepared SFM (median size=22.1 μm) and (b) after 24 hr ball milling (median size=1.7 μm).

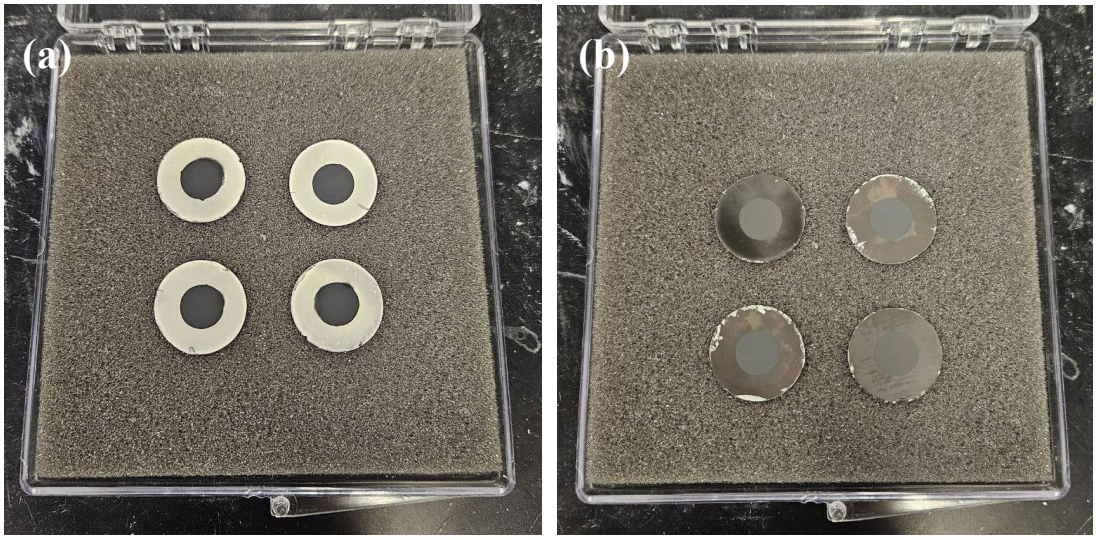


Figure 3.10. Sintered single cells with electrode active area of 1 cm^2 ready for testing, (a) fuel side, and (b) air side.

3.3 Testing of the cells

The electrochemical performance of the fabricated SOEC cells was evaluated using Fiaxell test station. The cell was first mounted onto the test fixture and sealed with Open Flanges™ inside the furnace. To make sure that the heat was evenly distributed and to avoid thermal shock, the system was heated slowly at 1 °C/min in air to 800 °C. When the appropriate temperature was reached, argon gas was added to the cathode side to clear out any leftover air from the fuel chamber. Then, the desired reactant gases were supplied to the fuel and air sides, and the system was allowed to stabilize until a steady open-circuit voltage (OCV) was observed. A stable and high open-circuit voltage (OCV), consistent with the theoretical Nernst potential, is not only an indicator of proper electrochemical activity but also confirms good gas tightness of the cell assembly, demonstrating that there is minimal gas leakage across the electrolyte. After achieving a stable OCV, electrochemical measurements—including I–V curves, electrochemical impedance spectroscopy (EIS), and distribution of relaxation times (DRT) analysis—were performed. Following these baseline tests, the fuel side was switched to a 10% H_2–Ar gas mixture for a reduction period to

promote in-situ exsolution of Fe–Ni nanoparticles at the cathode, while maintaining air flow on the anode side. After the reduction treatment, the gas supply was switched back to CO_2-containing fuel, and the electrochemical tests were repeated under identical conditions to evaluate the impact of nanoparticle exsolution on CO_2 electrolysis performance. Lastly, the cell temperature dropped in steps to 750 °C and then to 700 °C to see how performance changes with temperature.

Figure 3.11 depicts the test station that was used to measure the performance of solid oxide electrolysis cells (SOECs). The system is kept in a walk-in fume hood to keep the operator safe when they are working with carbon monoxide (CO) and other gases. Gas lines connect the gas cylinders to the test stations, and a mass flow controller controls the flow rate of gas into the system. There is a CO detector at the top that continuously monitors possible leaks. The cell is put within the Open Flanges™ testing fixture from Fiaxell, which is illustrated in Figure 3.12. Then, it is put inside the Squadro SQ11 kiln from Kittec. A thermometer is used to check the furnace's operating temperature. A Gamry potentiostat is connected to the cell's electrical connections, while a PC controls the potentiostat to take electrochemical measurements.

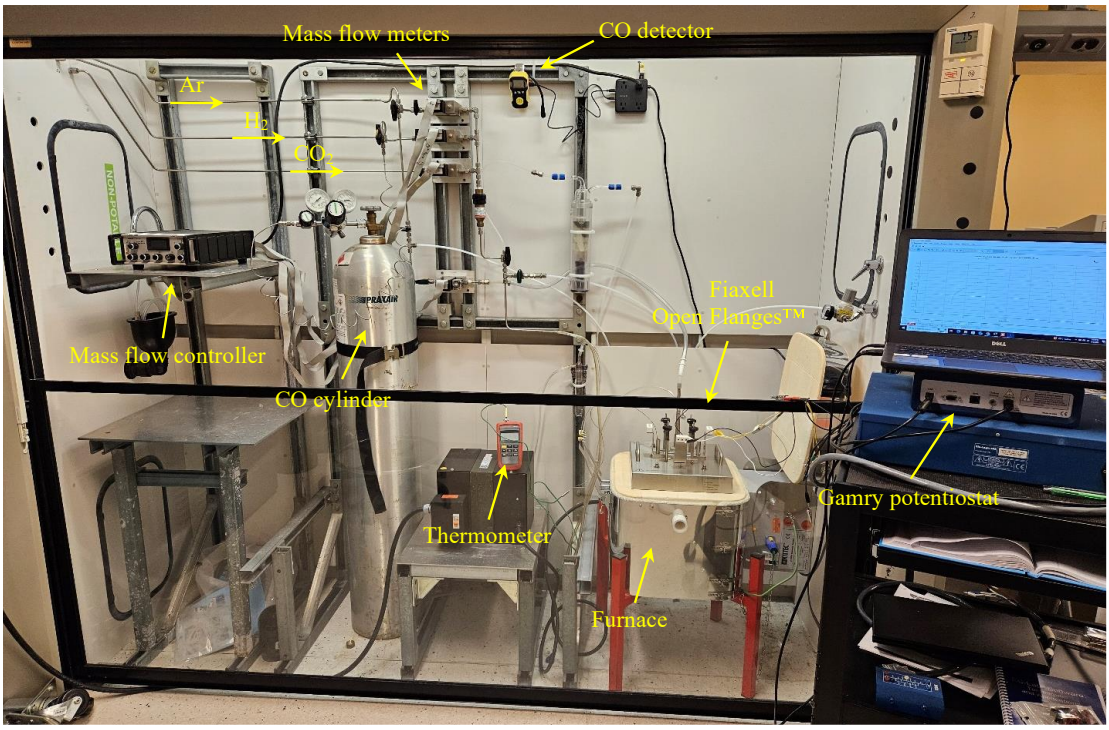


Figure 3.11. SOEC test station at the University of Waterloo.

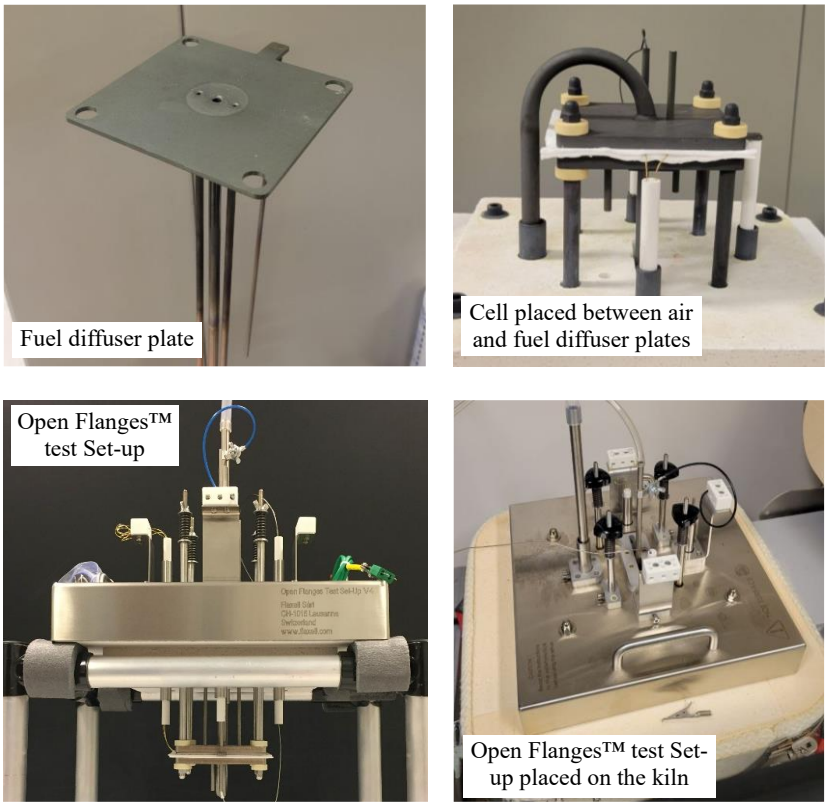


Figure 3.12. Fiaxell fuel cell test station parts.

3.4 Characterization and electrochemical measurements

Diverse characterization approaches were utilized to examine the structural, morphological, and electrochemical features of the synthesized materials and fabricated cells. The surface and cross-sectional microstructures were analyzed utilizing scanning electron microscopy (SEM). A Tescan Vega II SEM was utilized for general imaging and to examine cell architecture and layer thicknesses, whilst high-resolution imaging of electrode surfaces and exsolved nanoparticles was conducted using a Zeiss Merlin SEM. Transmission electron microscopy (TEM) was conducted utilizing a Libra 200 MC TEM for nanoscale structural research, facilitating meticulous examination of particle morphology, interfaces, and crystal lattice fringes. Phase identification and crystallographic analysis were conducted via X-ray diffraction (XRD) utilizing a Rigaku MiniFlex II diffractometer with Cu Kα radiation. To investigate the chemical states and surface composition of the elements, X-ray photoelectron spectroscopy (XPS) analysis was performed using a Thermo-VG Scientific ESCALab 250 microprobe. The XPS results provided insight into the oxidation states of transition metals and the effect of reduction treatment on surface chemistry, complementing the structural and morphological analysis. The electrochemical performance was assessed utilizing a Gamry 5000P potentiostat, which is also equipped with impedance spectroscopy (EIS) and distribution of relaxation times (DRT) analysis.

Chapter 4

Experimental Results of Fe–Ni Nanoparticle-decorated $Bi_{0.1}Sr_{1.9}Fe_{1.4}Ni_{0.1}Mo_{0.5}O_{6-\delta}$ Cathode in CO_2 Electrolysis

This chapter presents the experimental results for the fabrication and testing of double perovskite cathodes with nanoparticles for solid oxide CO_2 electrolysis cells (SOECs). Figure 4.1 illustrates the structural configuration of the cell used in this study. The cell is composed of a dense electrolyte layer sandwiched between two porous electrodes. The cathode (fuel electrode) is made of a co-doped perovskite material decorated with exsolved metal nanoparticles to enhance CO_2 adsorption and catalytic activity. The anode (oxygen electrode) facilitates the release of oxygen gas. This schematic provides a visual representation for the material-specific results and performance evaluations presented in the following sections.

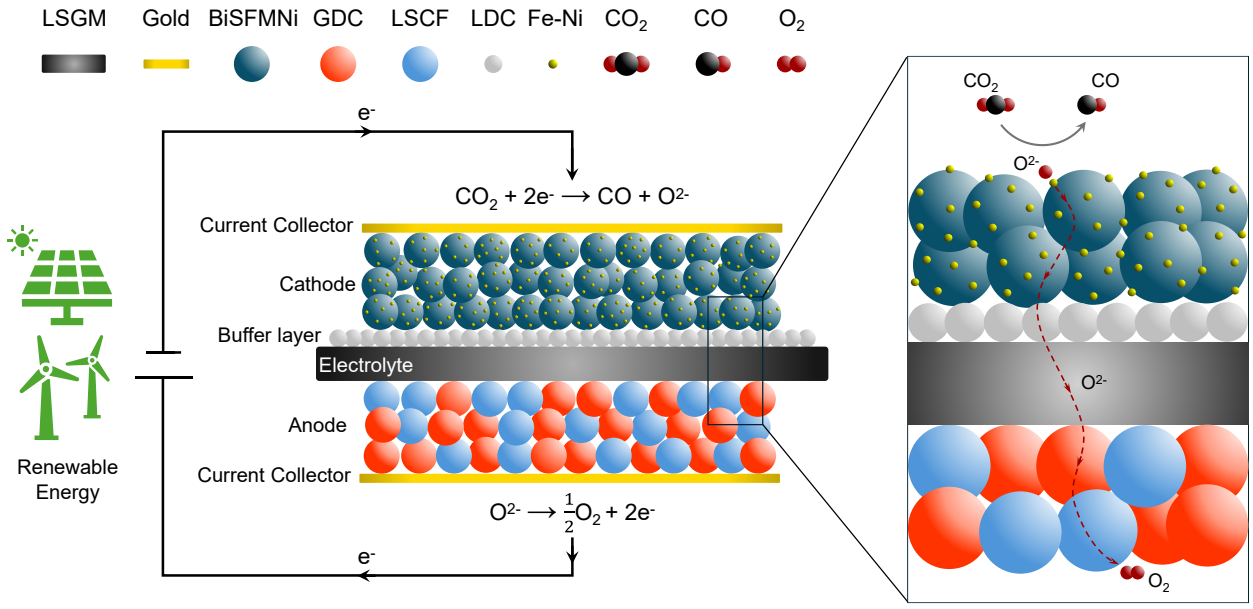


Figure 4.1. Schematic of the solid oxide electrolysis cell configuration used in this study.

The first step is to use X-ray diffraction (XRD) to make sure that the synthesized materials are pure phase. Next, compatibility tests are done to see how stable the cathode material is when it is mixed with the buffer layer and electrolyte. Scanning electron microscopy (SEM) and transmission electron microscopy (TEM) are then used to give a detailed picture of the microstructure, focusing on the particle morphology and nanoparticle exsolution. Surface chemical states and elemental compositions are then investigated using X-ray photoelectron spectroscopy (XPS). Lastly, the cell's electrochemical performance is tested using current–voltage (I–V) measurements, electrochemical impedance spectroscopy (EIS), and distribution of relaxation times (DRT) analysis. This gives us information about how the electrodes work and how changes to the materials affect the overall performance of the cells.

4.1 Crystal structure

X-ray diffraction (XRD) is used to look at the crystal structure and phase purity of the synthesized perovskite materials. The results, shown in Figure 4.2, indicate that all the compositions - SFM, Bi-doped SFM (BiSFM), and Bi/Ni co-doped SFM (BiSFMNi) - have a pure double perovskite phase with no secondary phases that could be seen. This shows that adding Bi to the A-site and Ni to the B-site was accomplished without changing the structure of the perovskite lattice.

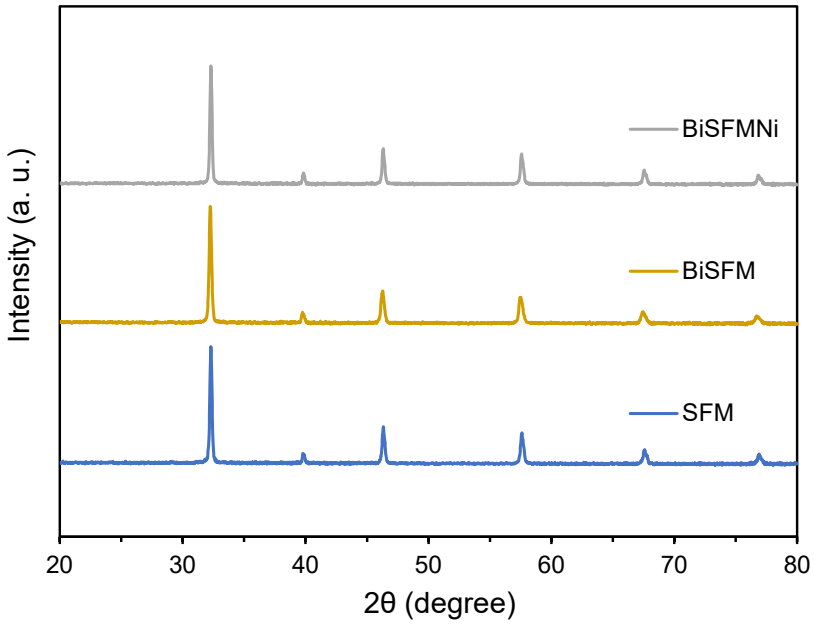


Figure 4.2. XRD patterns of SFM, BiSFM, and BiSFMNi powders.

4.2 Interfacial compatibility

Compatibility experiments between BiSFMNi, LDC and LSGM helped to confirm the need of the LDC buffer layer. Binary mixes of BiSFMNi-LDC, BiSFMNi-LSGM, and LDC-LSGM were prepared in a 1:1 weight ratio, pressed into pellets, and sintered at 1100 °C for 5 hours. XRD analysis was then performed to evaluate phase stability. As shown in Figure 4.3, there is a strong chemical compatibility between LSGM and LDC as well as between LDC and BiSFMNi. A small amount of a new phase in the BiSFMNi-LSGM combination suggests some interfacial interaction between these two materials. These results confirm the need of a thin LDC buffer layer to reduce unwanted interfacial interactions and enhance the chemical stability between the LSGM electrolyte and BiSFMNi cathode.

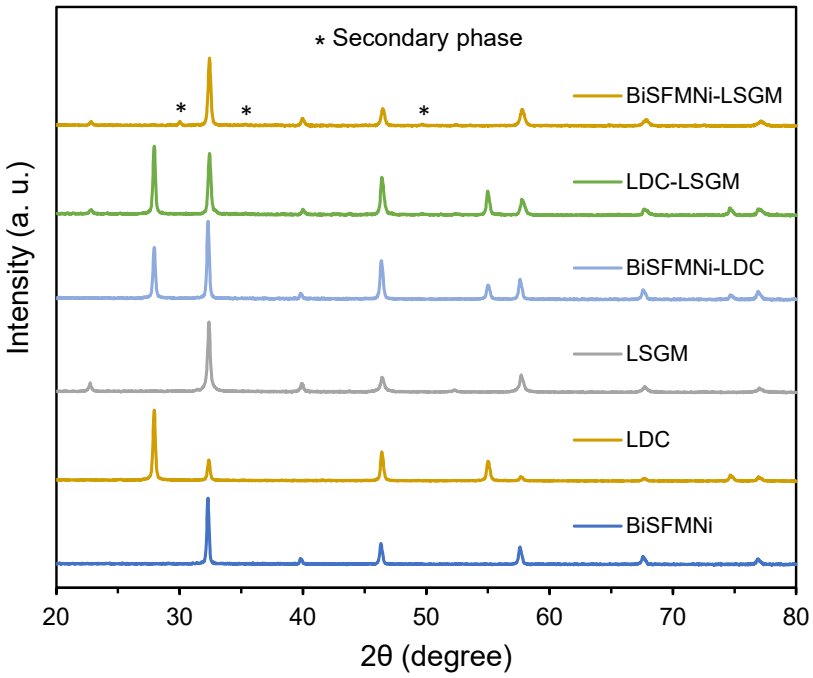


Figure 4.3.Chemical compatibility of binary mixes of BiSFMNi -LDC, BiSFMNi -LSGM and LDC-LSGM.

4.3 Thermal Stability

The Thermogravimetric analysis (TGA) results, shown in Figure 4.4, provide valuable insights into the thermal stability and oxygen release behavior of the perovskite powders under different atmospheres. Both SFM and BiSFMNi samples exhibit gradual weight loss with increasing temperature, mainly associated with lattice oxygen release and minor surface species desorption such as adsorbed water and carbonates. The TGA curves can be divided into three distinct weight-loss regions: (i) 25–400 °C, corresponding to desorption of adsorbed water and surface species, (ii) 400–800 °C, associated with lattice oxygen release and redox activity of the perovskite, and (iii) above 800 °C, linked to deep oxygen loss and potential partial structural instability. In air, the weight loss is minimal compared to inert (N_2) or reactive (CO_2) conditions, confirming the higher stability of the perovskite lattice in oxidizing environments. Under pure CO_2, both SFM and BiSFMNi exhibit slightly higher weight loss, which may be related to surface interactions with

CO_2 or transient carbonate formation and decomposition. Notably, the Bi and Ni doping shows improved thermal stability compared to pristine SFM, with less overall weight change across all atmospheres, suggesting that co-doping helps stabilize the oxygen sublattice and suppresses excessive oxygen release.

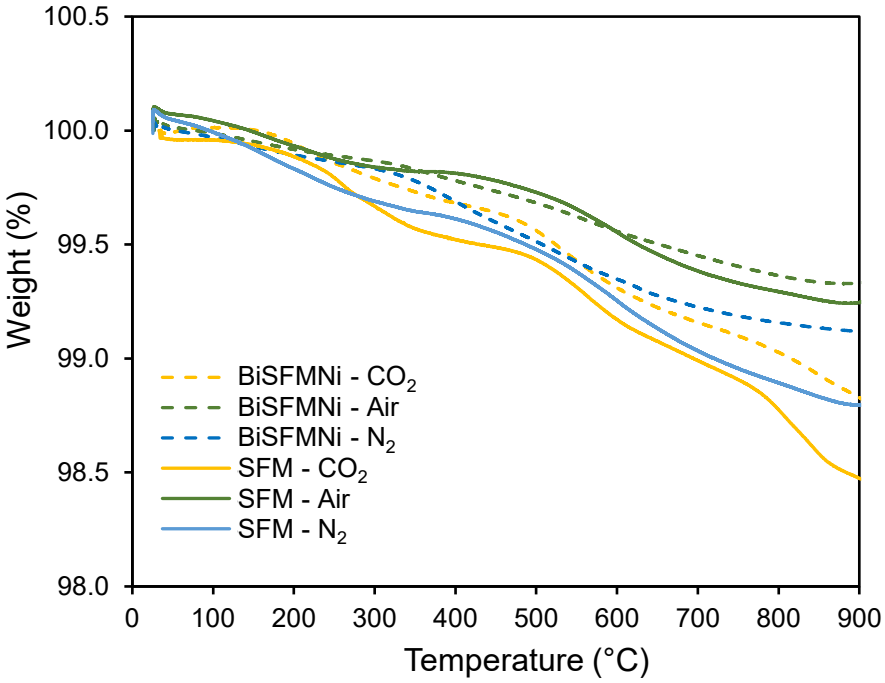


Figure 4.4. TGA of SFM and BiSFMNi samples in N_2, Air and CO_2 atmospheres.

4.4 Cathode material exsolution behaviors

This section presents the results of various characterization techniques used to investigate the exsolution behavior of the cathode materials, providing insights into their structural, morphological, and compositional changes under reducing conditions.

4.4.1 X-ray Diffraction results

XRD analysis was conducted on both BiSFMNi samples under reducing conditions to investigate the exsolution behavior; the results are plotted in Figure 4.5. The oxidized version of the BiSFMNi showed a pure double perovskite phase. After 1 hour of reduction in 5% H_2/Ar at 800 °C, however, the XRD pattern showed the appearance of secondary phases, such as a Ruddlesden–Popper (RP) structure, metallic Fe–Ni, and leftover double perovskite. This means that the perovskite scaffold breaks down in part and nanoparticles are starting to exsolve. The Fe–Ni peaks got stronger as the reduction time increased, while the double perovskite peaks got weaker. This shows that the structure is breaking down and that the RP phase is becoming more dominant. After 5 hours of reduction, the XRD pattern predominantly showed the Ruddlesden–Popper phase along with Fe–Ni alloy peaks. This suggests that the original double perovskite structure had largely transformed, and a significant number of nanoparticles had been exsolved.

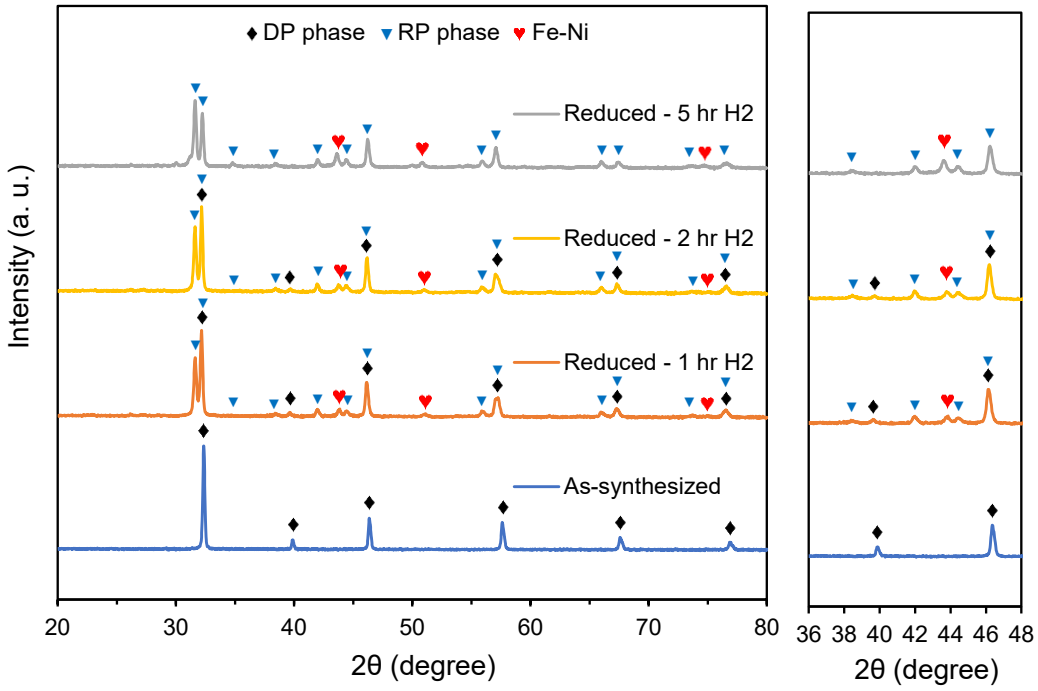


Figure 4.5. XRD patterns of BiSFMNi samples as-synthesized and reduced in 5% H_2/Ar at 800 °C for different duration.

Figure 4.6 shows the Rietveld refinement that was performed on the XRD pattern of BiSFMNi sample that had been reduced for one hour The sample had 6.56% Fe–Ni alloy, 27.61% DP phase, and 65.83% RP phase.

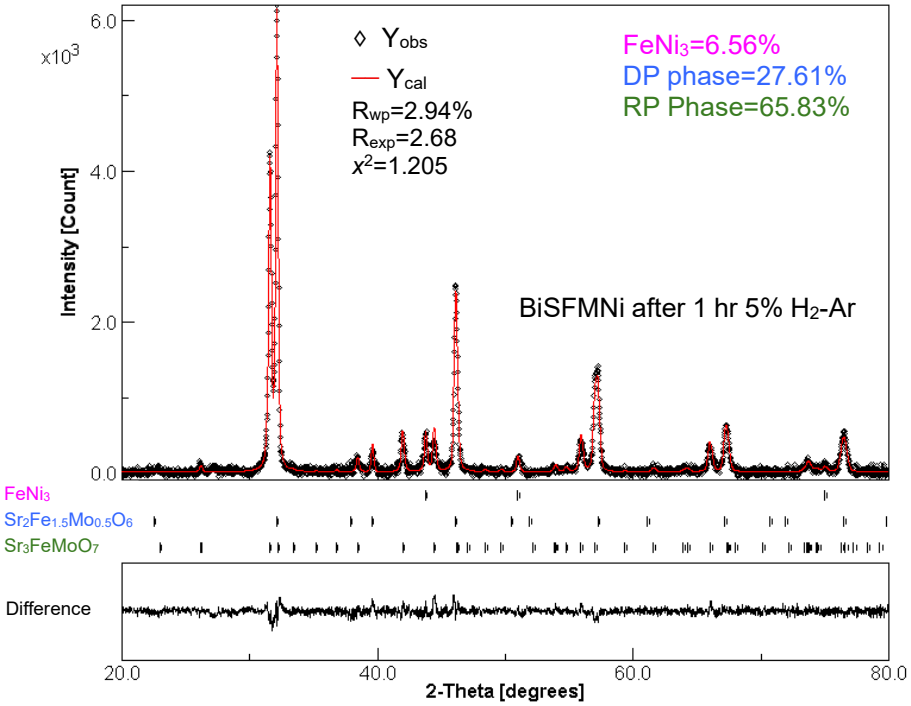


Figure 4.6. Rietveld refinement results of XRD patterns BiSFMNi sample reduced in 5% H_2/Ar at 800 °C for 1 hour.

XRD was also used to look at three samples of the BiSFMNi material: the as-synthesized (oxidized), reduced, and reoxidized states and the results are shown in Figure 4.7. This was done to see whether the structure could return to its original state. The XRD analysis of the reoxidized BiSFMNi sample showed that the double perovskite structure had completely recovered. There were no peaks that matched the previously exsolved Fe–Ni alloy or Ruddlesden–Popper phase. This means that the changes in structure caused by reduction is reversible. The reoxidation process effectively puts the exsolved metal species back into the lattice, bringing the material back to its original double perovskite phase.

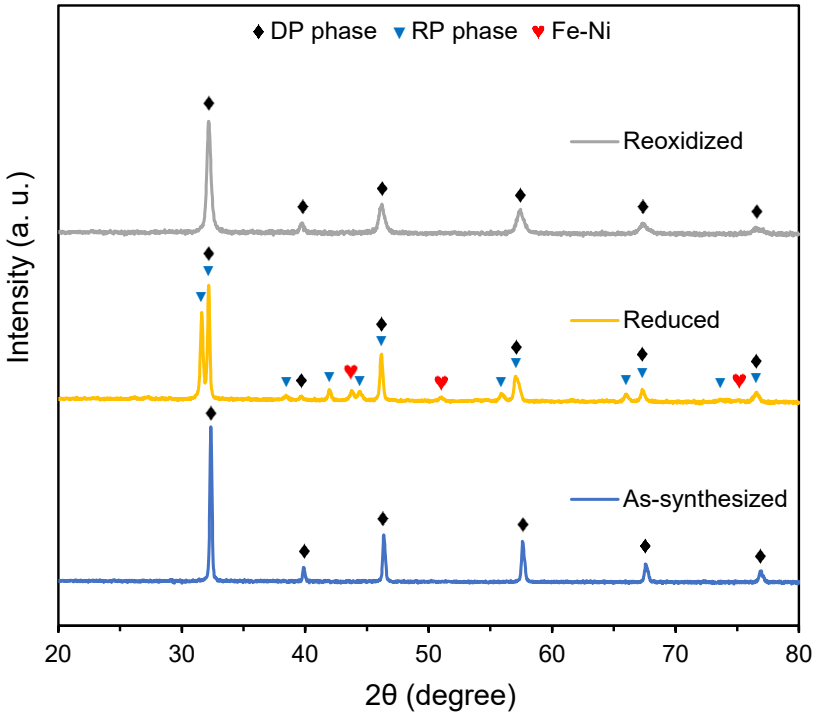


Figure 4.7. XRD patterns of BiSFMNi in oxidized, reduced, and reoxidized states.

4.4.2 X-ray photoelectron spectroscopy results

X-ray photoelectron spectroscopy (XPS) was performed to investigate the chemical states of Fe, Ni, and O before and after reduction and results are shown in Figure 4.8. The Fe 2*p* spectra showed that the sample contained Fe^{3+} and Fe^{2+}. After reduction, a clear Fe^{0} peak appeared, showing that some of the iron had been reduced. In the same way, the Ni 2*p* spectra first displayed peaks that matched Ni^{2+} and Ni^{3+}, but following reduction, they changed to produce a Ni^{0} signal. The Mo 3d spectra showed Mo^{6+} in the fresh sample, with the appearance of Mo^{5+} after reduction; however, no Mo^{0} peak was observed. This suggests that while Mo underwent partial reduction, it did not participate in the formation of metallic nanoparticles, unlike Fe and Ni. The O 1*s* spectra had two peaks: one for lattice oxygen (O_{latt}), which is usually seen at lower binding energies, and the other for adsorbed oxygen species (O_{ads}), which is seen at higher binding energies. After the reduction, the O_{latt} peak became less intense, while the O_{ads} peak got stronger. This change showed that the

reduction treatment causes oxygen vacancies to occur in the perovskite lattice, perhaps because of Fe–Ni nanoparticles exsolution. These results showed that Ni and Fe were successfully reduced in-situ to their metallic forms, which supports the idea that exsolved Fe–Ni nanoparticles can form on the surface of perovskite.

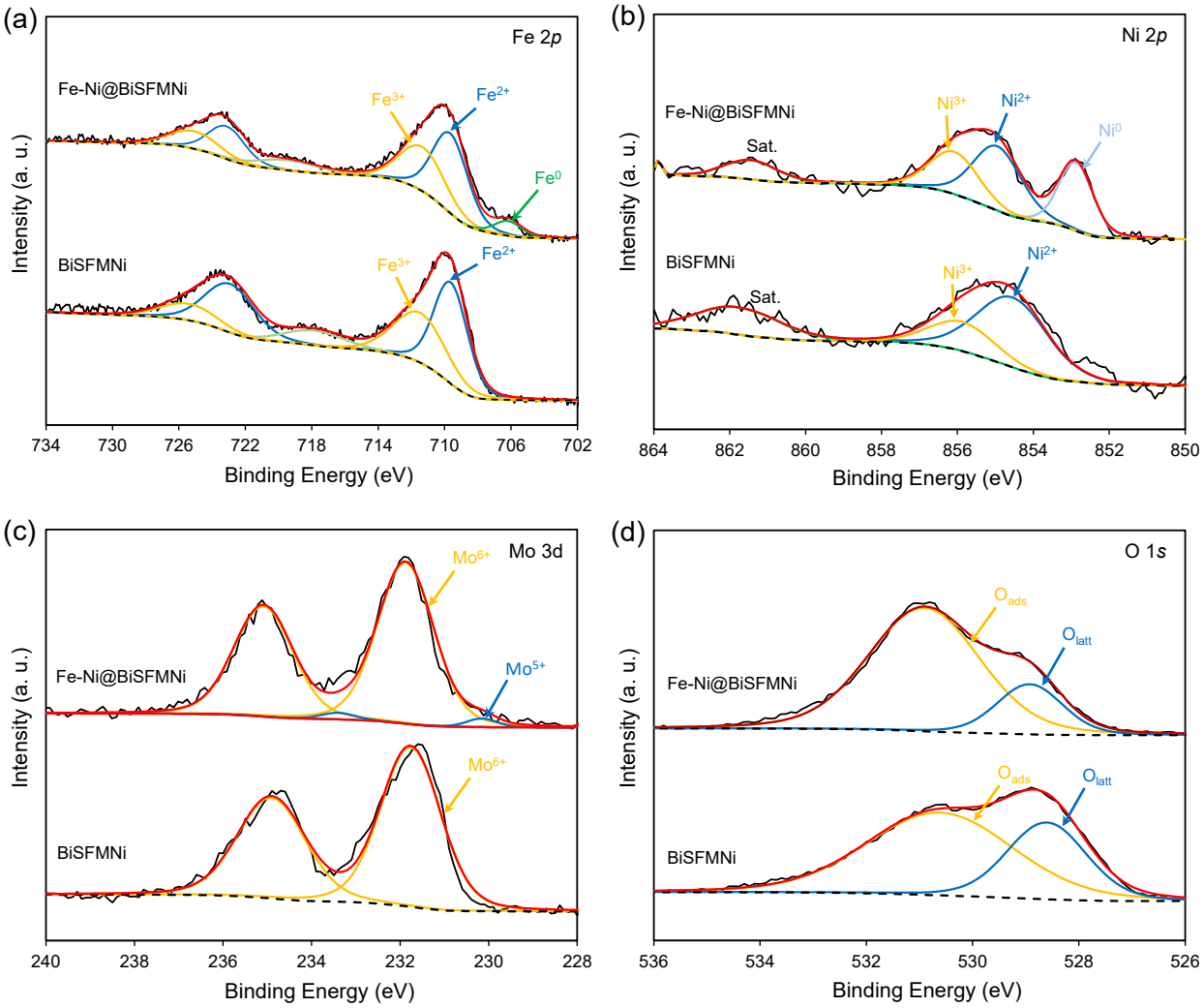


Figure 4.8. XPS spectra of (a) Fe 2*p*, (b) Ni 2*p*, (c) Mo 3*d*, and (d) O 1*s* regions before and after 1 hr reduction in 5% H_2-Ar.

4.4.3 Scanning electron microscopy results

Figure 4.9 presents SEM images of BiSFMNi samples at different stages of the reduction and reoxidation process, including the as-synthesized powder, and samples reduced for 2, 10, 30, and 60 minutes, followed by a reoxidized sample. When oxidized, the material had clean, packed grains with smooth surfaces, which is normally expected from a well-sintered perovskite structure with no particles on the surface. As the reduction time increases, a gradual emergence of surface nanoparticles is observed. At 2 and 10 minutes, a few nanoparticles begin to appear, while at 30 and 60 minutes, the number and density of exsolved nanoparticles significantly increase, indicating progressive exsolution of Fe–Ni alloy particles from the perovskite matrix under a reducing atmosphere (5% H_2/Ar at 800 °C). The appearance of surface nanoparticles matches the XRD evidence of the formation of the Fe–Ni phase and a partial change in structure. The grains underneath also look like they are getting rougher on the surface, which could mean that the structure is changing as it moves into the Ruddlesden–Popper phase. In the reoxidized sample, the nanoparticles are no longer visible, and the surface appears smoother and more compact compared to the reduced state. This suggests that the exsolved Fe–Ni nanoparticles moved back into the perovskite lattice during reoxidation, bringing back the original structure. The surface morphology looks like that of the oxidized sample, which backs up the conclusion that the structural change can happen again under redox cycling circumstances, which was also found by XRD.

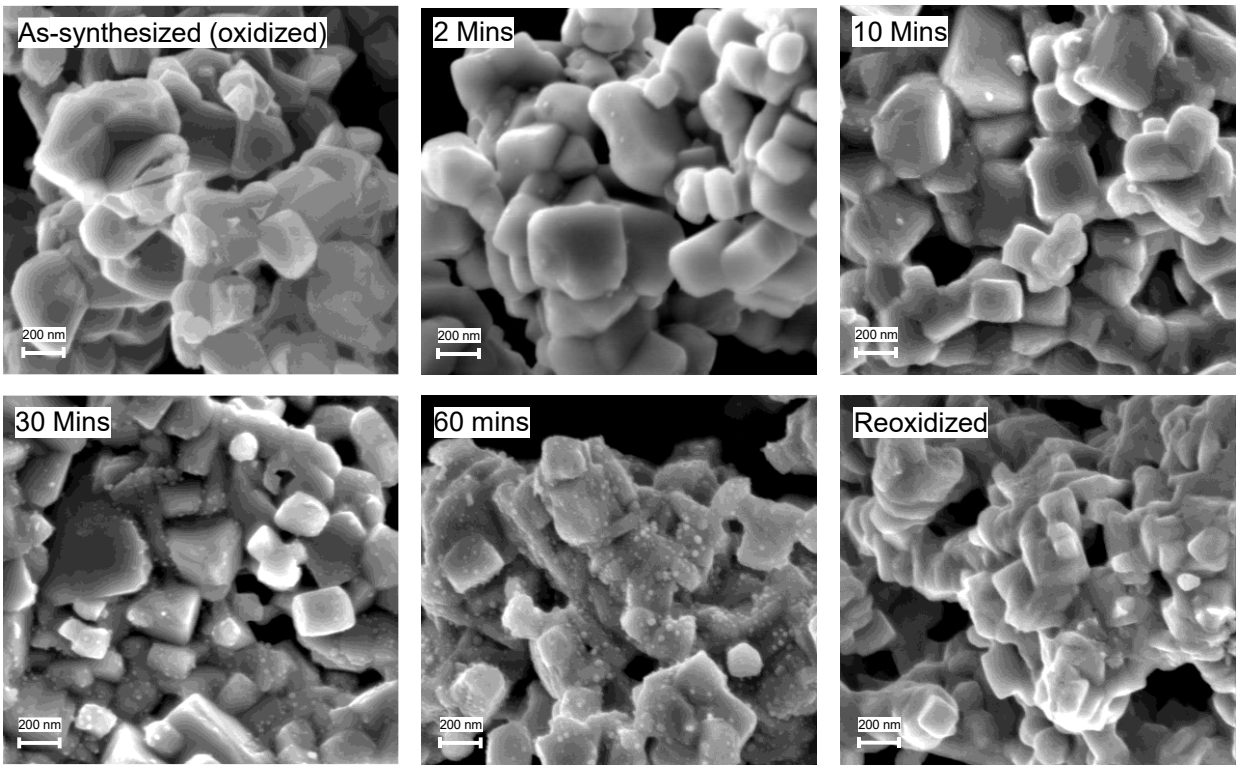


Figure 4.9. SEM images of BiSFMNi in three states: As-synthesize, reduced in 5% H_2/Ar at 800 °C for 2, 10, 30 and 60 minutes, and reoxidized in air.

4.4.4 Transmission electron microscopy results

The exsolution behavior and structural evolution of the BiSFMNi were investigated using transmission electron microscopy techniques. Figure 4.10 and 4.11 present comparative TEM images of the sample before and after reduction at 800 °C for 2 hours in 5% H_2/Ar atmosphere.

In the as-synthesized state (Figure 4.10), the perovskite exhibits a cubic, dense surface morphology without any apparent nanoparticle decoration. Energy-dispersive X-ray spectroscopy (EDS) confirms a homogeneous elemental distribution across the sample. The quantified atomic percentages closely match the nominal target composition of $Bi_{0.1}Sr_{1.9}Fe_{1.4}Ni_{0.1}Mo_{0.5}O_{6-\delta}$, verifying the successful synthesis and cation incorporation into the lattice.

After reduction (Figure 4.11), clear morphological changes are observed. Numerous

nanoparticles have emerged and are uniformly distributed on the surface of the perovskite matrix. Scanning transmission electron microscopy (STEM) images clearly show these nanoparticles anchored to the host surface. High-resolution TEM (HR-TEM) images reveal lattice fringes indicating the crystalline nature of both the perovskite matrix and the exsolved nanoparticles. The interface between the nanoparticle and the host lattice appears coherent, suggesting strong integration and good adhesion.

To further analyze the composition and phase separation, EDS analysis carried out at two places: one on a nanoparticle and one on the perovskite bulk. The EDS spectrum from the nanoparticle area had a strong Fe peak and a smaller but clear Ni peak. This means that Fe–Ni alloy nanoparticles were formed, which is what was seen in the XRD as the Fe–Ni phase. However, the EDS spectra from the perovskite bulk showed Sr, Fe, Mo, Bi, O, and a very little quantity of Ni. This means that most of the Ni ions were exsolved during reduction, but a small amount stayed in the bulk lattice. Ni exsolution happens over time. It is likely that after a longer reduction time (like 5 hours), almost all of the Ni will be exsolved to form more nanoparticles. This migration of Ni from the lattice to the surface can be harnessed to control the density, size, and distribution of exsolved nanoparticles. The atomic percentages obtained from the EDS analysis after reduction of the bulk perovskite closely match the stoichiometry of the Ruddlesden–Popper phase, $Sr_3Fe_{1.5}Mo_{0.5}O_{6.5-\delta}$, confirming the presence of this secondary phase.

Additionally, EDS elemental mapping was performed to provide a clearer visualization of the spatial distribution of individual elements across the sample. This technique helped distinguish the regions containing exsolved nanoparticles from the perovskite and Ruddlesden–Popper phases based on elemental composition. The EDS maps, shown in Figure 4.12, show the spatial distribution of key elements: Fe and Ni signals are strongly localized in the exsolved nanoparticle

regions, confirming the formation of Fe–Ni alloy nanoparticles, consistent with Fe–Ni as identified in XRD analysis. In contrast, Sr, Mo, Bi, and O signals are concentrated within the bulk matrix, indicating their retention in the perovskite lattice. The presence of Bi remains uniformly distributed in the matrix, suggesting that Bi remains stable during reduction and does not participate in nanoparticle formation.

Overall, the combination of STEM, HR-TEM, and EDS analysis confirms that the reduction treatment induces selective exsolution of B-site elements (Fe and Ni), while the A-site dopant (Bi) and other structural components remain integrated in the perovskite lattice.

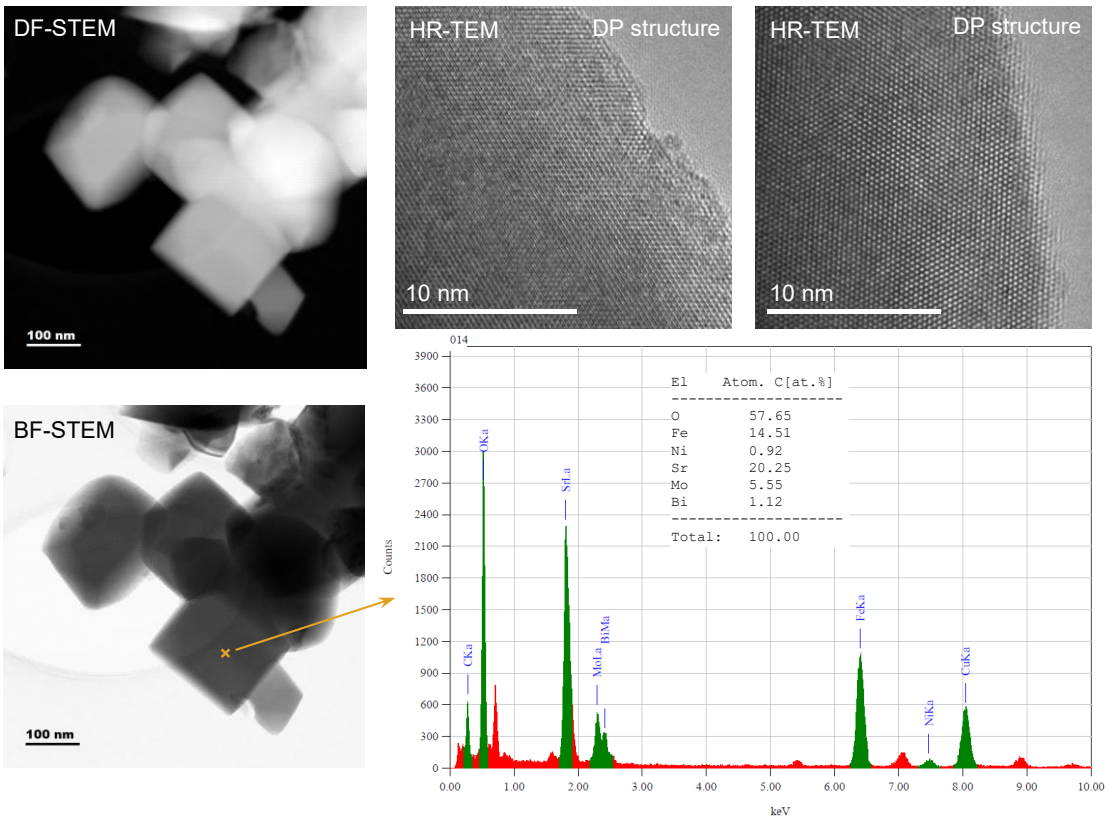


Figure 4.10. TEM image and EDS analysis of the as-synthesized BiSFMNi sample.

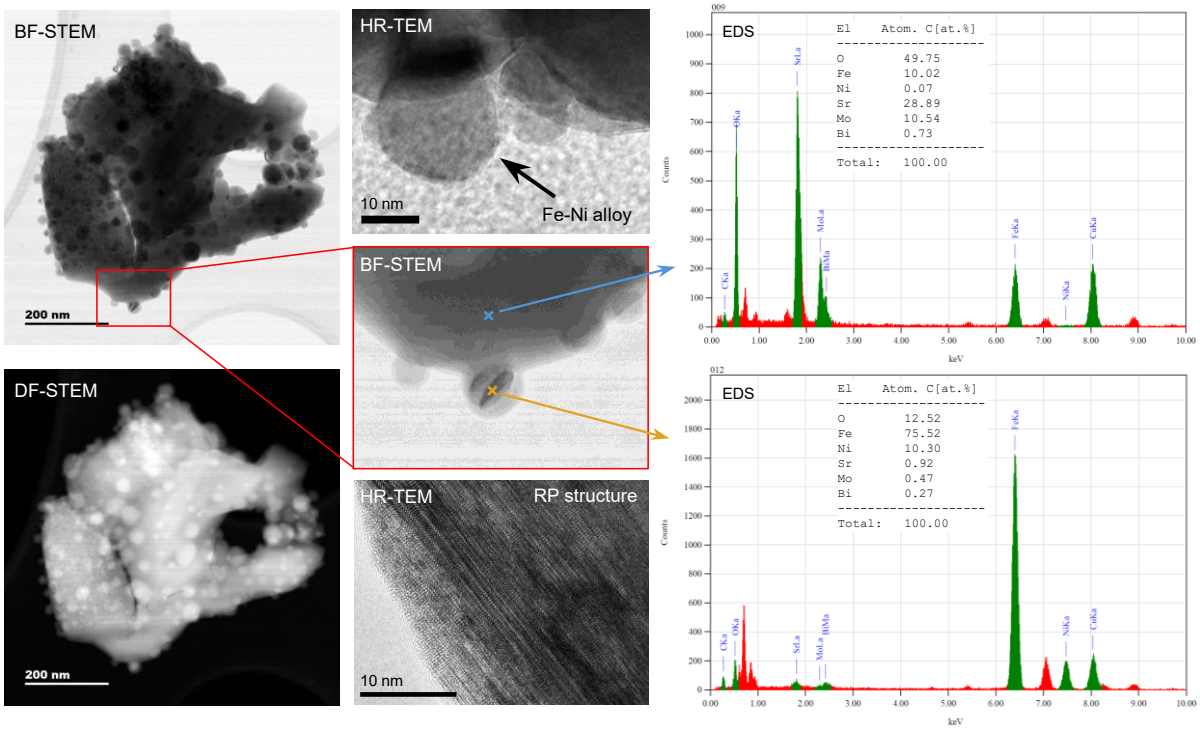


Figure 4.11. TEM image and EDS analysis of the reduced BiSFMNi sample.

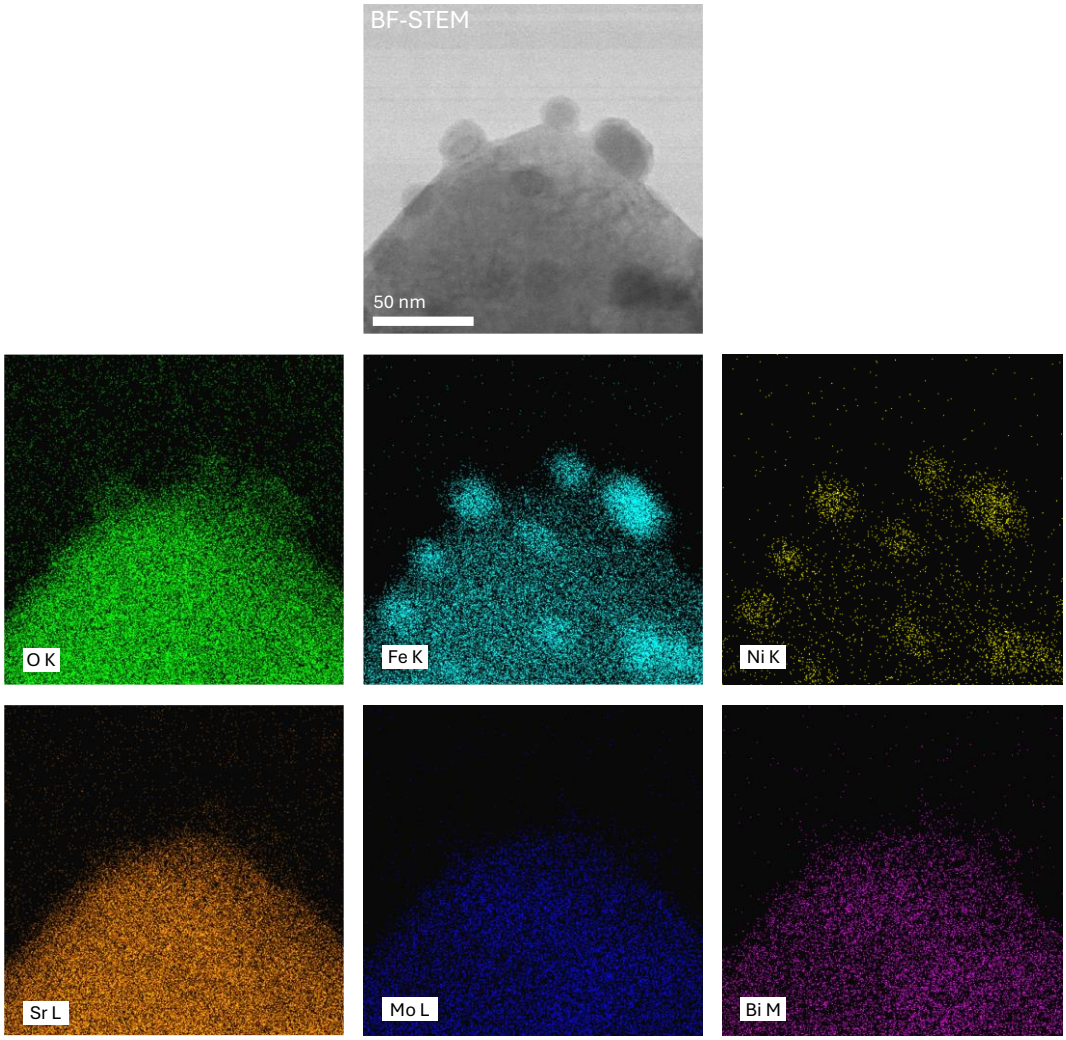


Figure 4.12. STEM image and EDS elemental mapping of BiSFMNi perovskite after reduction treatment showing exsolved nanoparticles.

4.5 Cell structure

The SEM cross-sectional image, Figure 4.13 , shows the multilayer structure of the fabricated solid oxide electrolysis cell (SOEC), confirming successful layer deposition and good interfacial contact between components. The LSGM electrolytelayer is around 275 μm thick and gives the structural strength and ionic conductivity. On the fuel side (bottom), there is a 40 μm-thick porous cathode (BiSFMNi) that is separated from the electrolyte by a 5 μm La-doped ceria (LDC) buffer layer. This thin layer was deposited via spin coating, which proved to be highly effective for achieving

a uniform and continuous coating. The LDC layer makes the cathode and the LSGM electrolyte more chemically compatible and stops unwanted reactions at the interface. There is a 55 µm-thick porous anode (LSCF/GDC) on the oxygen side (top). The microstructure of both electrodes is porous, which is necessary for gas diffusion and offering a triple-phase boundary during CO_2 electrolysis. The clear layer boundaries and the strong interfaces show that the screen-printing and sintering procedures worked well.

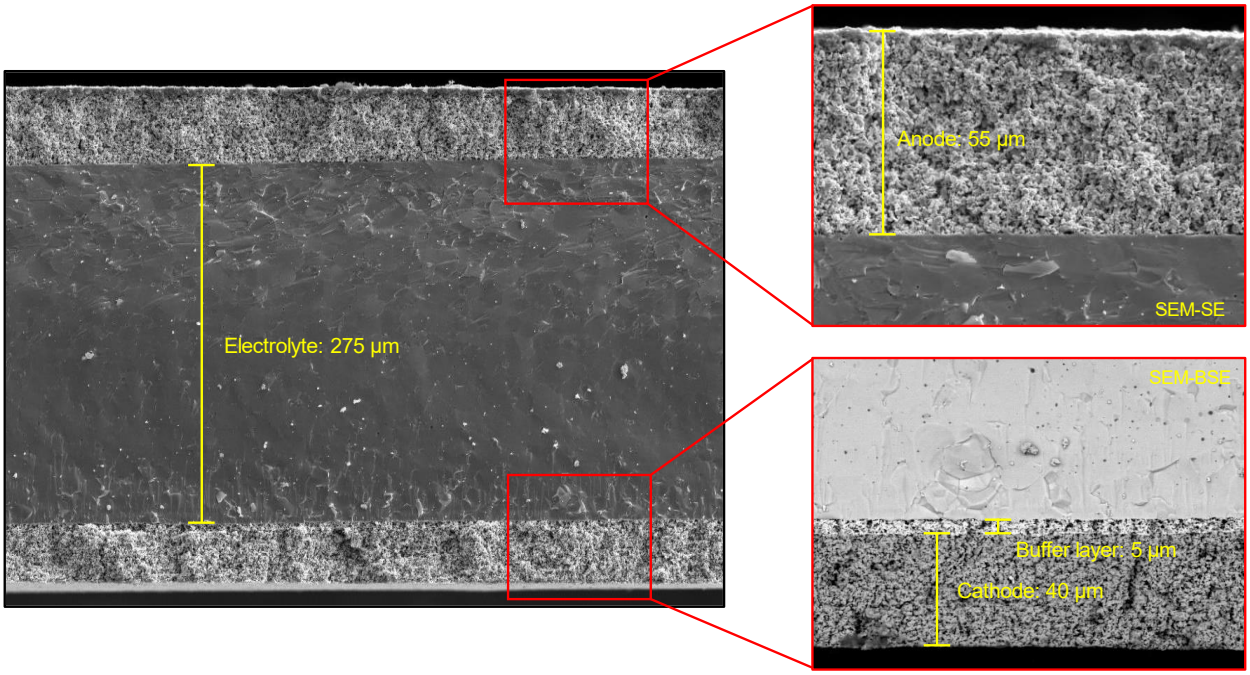


Figure 4.13. Cross-sectional SEM image of the fabricated single cell.

Line EDS analysis was performed across to see how the elements were spread out across the cell. In Figure 4.14, along with the SEM cross-section, the matching elemental intensity profiles are depicted. The figure clearly shows that the layers have different compositions with well-defined interfaces. The LSCF/GDC oxygen electrode has signals for La, Sr, Co, Fe, Gd and Ce, which is expected from its mixed perovskite-fluorite structure. As expected for a LSGM phase, the electrolyte is mostly made up of La, Sr, Ga, and Mg. There is a little area between the electrolyte

and the cathode where La and Ce signals are higher than normal. This shows that a thin LDC (La-doped Ceria) buffer layer has been successfully deposited. On the fuel side, the BiSFMNi is confirmed by big signals for Fe, Mo, Bi and a tiny signal for Ni. There was no significant elemental crossover or interdiffusion between neighboring layers, which shows that the spin-coated LDC buffer layer does a good job of keeping the cathode and electrolyte from reacting with one other in ways that are not desirable.

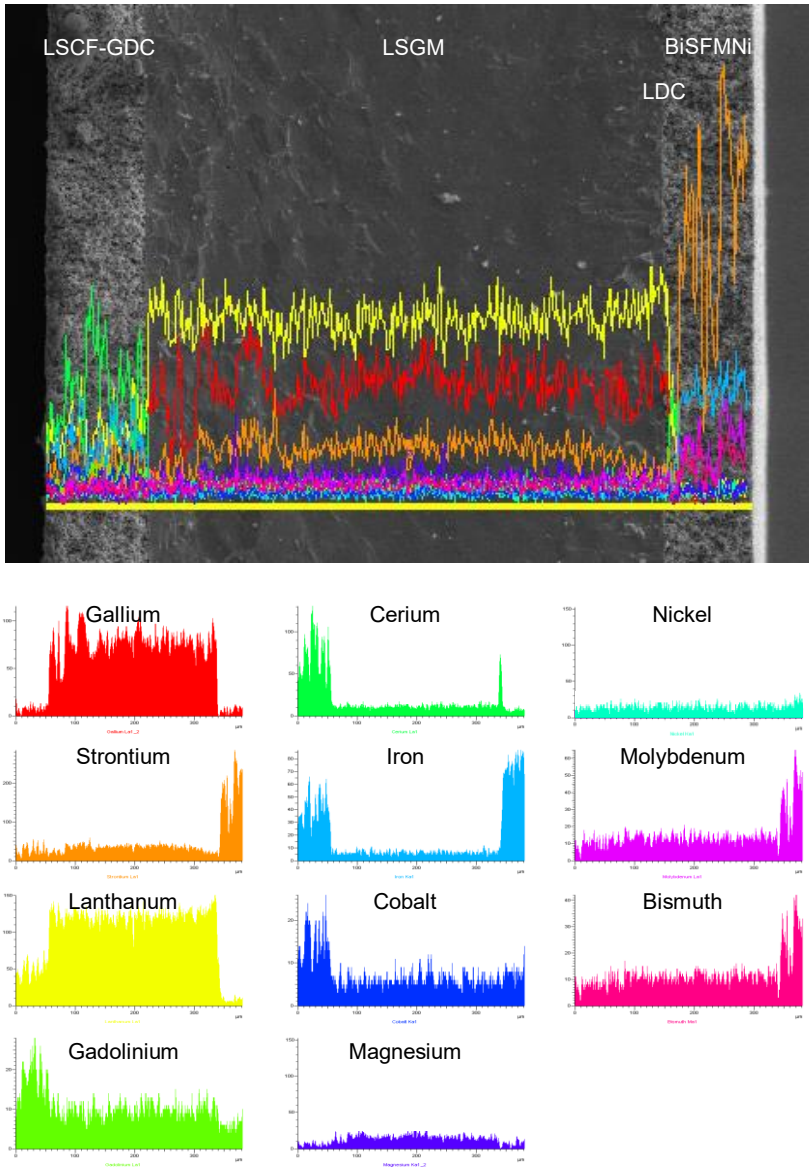


Figure 4.14. Line EDS elemental mapping across the cell cross-section.

4.6 Cell electrochemical performance

This section presents the electrochemical performance of the fabricated cell for CO_2 electrolysis using BiSFMNi and Fe–Ni@BiSFMNi as the cathode materials. A controlled sol–gel synthesis route was employed, with carefully standardized calcination and sintering steps, ensuring reproducibility in phase composition and microstructure, as confirmed by XRD and SEM. Although large-scale statistical reproducibility studies have not yet been performed, the results obtained are consistent within the fabricated batches and align well with reported performances in the literature, thereby strengthening confidence in their reliability. All cells were conditioned with the same temperature ramp (1 °C min^{-1} to 800 °C), gas purities and flow rates, reduction schedule (5% H_2/Ar, 2 h), and measurement sequence (OCV stabilization → IV curves → EIS → DRT). Geometric electrode area, contact paste, and fixture compression were held constant. Mass-flow controllers and the thermocouple were calibrated; leak-tightness was verified by OCV values within 20 mV of the Nernst potential for the CO/CO_2–air pair. Impedance spectra were collected with the same AC amplitude and frequency window.

Reproducibility was evaluated by testing three independently fabricated electrolyte-supported cells per cathode configuration under 10% CO/CO_2 and at 800 °C. Figure 4.15 shows the I–V curves of the three cells before and after adding nanoparticles, which exhibit similar trends and overlapping behavior, confirming good reproducibility of the results. While minor variations in current density (within ~0.1–0.15 A/cm^2 at 1.5 V) were observed, these are attributed to inevitable differences in cell fabrication (e.g., electrode microstructure, thickness uniformity, and contact quality). Overall, the results demonstrate that the observed performance enhancement with Fe–Ni nanoparticle exsolution is a consistent phenomenon.

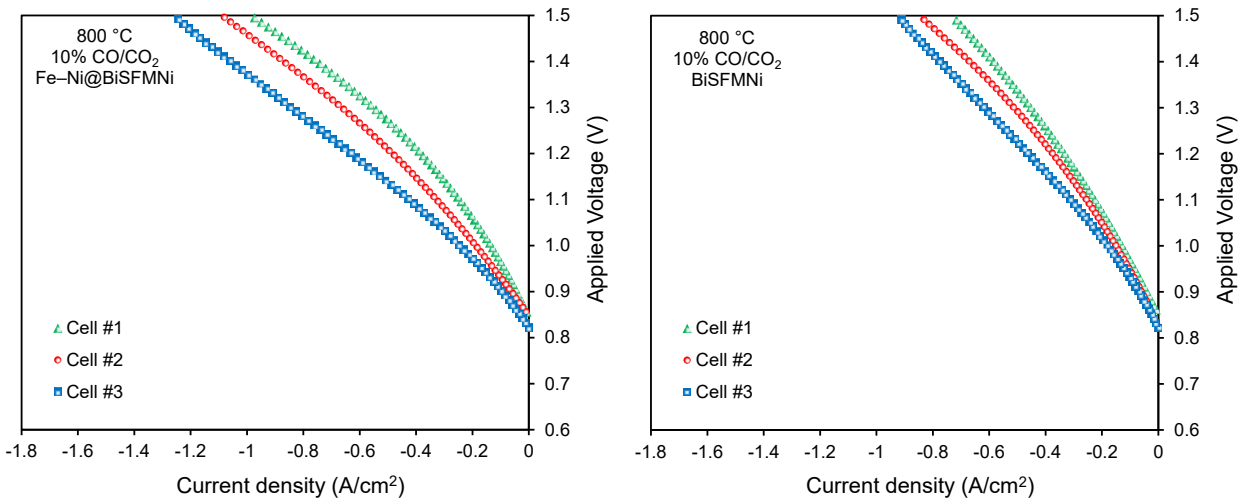


Figure 4.15. I–V characteristics of three independently fabricated cells, demonstrating reproducibility of electrochemical performance.

4.6.1 I–V Characteristics of BiSFMNi and Fe–Ni@BiSFMNi Cathodes

Figure 4.16(a) presents the I–V curves of cell using BiSFMNi and Fe–Ni@BiSFMNi materials as the cathodes for pure CO_2 electolysis.. The BiSFMNi cathode, containing Ni and Bi co-doped perovskite, shows moderate performance with a gradual increase in current density as the voltage increases. In contrast, the Fe–Ni@BiSFMNi sample, in which Fe–Ni alloy nanoparticles were exsolved through a 2-hour reduction process, delivers significantly higher current at higher voltages. At a cell voltage of 1.6 V, the current density for the Fe–Ni@BiSFMNi cathode is 1.3 A/cm^2, which is 30% higher than that of 1.0 A/cm^2 BiSFMNi. This improvement can be attributed to increased surface catalytic activity. The nanoparticles of Fe–Ni provides numerous reaction sites where CO_2 can absorb and reduce, ultimately increase the electrochemical reaction rate. This can also be explained by the fact that these nanoparticles increase the triple-phase boundary (TPB) density**,** allowing for more distributed reaction sites.

Figure 4.16(b) shows the relative improvement in current density of Fe–Ni@BiSFMNi versus BiSFMNi as a function of applied voltage. This was done to measure how much better the performance was with Fe–Ni nanoparticle exsolution. The data clearly showed that increasing the voltage led to an increase in current density. The Fe–Ni@BiSFMNi cathode always outperformed the undoped one over the entire voltage range. At low voltage around 1–1.2 V, the improvement in the current density is because of reduction in activation overpotential. However, this improvement is small as the activation overpotential has a small contribution in total overpotential. But when the voltage goes above 1.4 V, the improvement gets larger, reaching over 50% at 1.8 V. This means that the exsolved Fe–Ni nanoparticles help with charge transfer (lower ohmic resistance) and reduce concentration polarization more at higher current densities. These results support the idea that exsolution is a good way to increase the performance of SOEC cathodes, especially when they are under high load or demand.

Fe–Ni@BiSFMNi-based cell was considered for further analysis. The effect of temperature between 700 and 800 °C on the I–V curve was investigated and plotted in Figure 4.16(c). As expected, raising the operating temperature led to increased current densities at all voltages. This improvement can be attributed to faster electrochemical reaction kinetics, especially for the CO_2 reduction process, which is very thermally dependent. At 800 °C, the cell exhibits the highest performance, with a current density exceeding –1.3 A/cm² at 1.6 V. In contrast, at 750 °C and 700 °C, both activation and ohmic losses are more pronounced, leading to a significantly lower current response of –0.67 A/cm² and –0.23 A/cm², respectively.

Constant-voltage tests were performed at 1.0 V, 1.2 V, and 1.4 V for 20 minutes at 800 °C to see how stable the Fe–Ni@BiSFMNi cathode was in the short term. Figure 4.16(d) shows that all three curves start with a drop in current density in the first few seconds. After this change, the current

density remains stable, which suggests that the electrode keeps its structural and electrochemical integrity throughout the test.

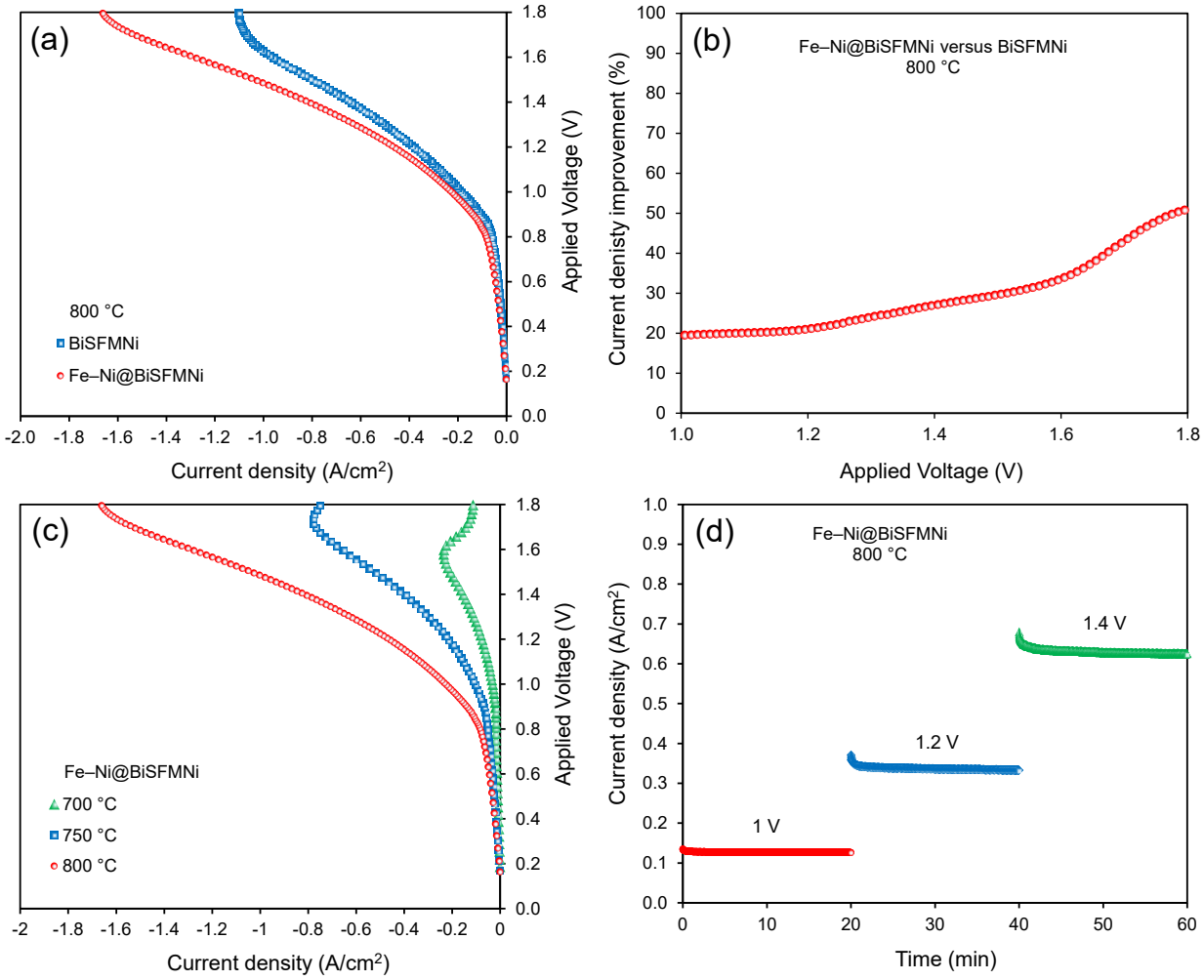


Figure 4.16. Electrochemical performance of cell under CO_2 electrolysis conditions: (a) I–V characteristics of BiSFMNi and Fe–Ni@BiSFMNi cathodes, (b) Percentage improvement in current density of Fe–Ni@BiSFMNi over BiSFMNi, (c) I–V characteristics of the Fe–Ni@BiSFMNi cathode measured at 700 °C, 750 °C, and 800 °C, and (d) Short-term electrochemical stability test under constant voltage operation at 1.0 V, 1.2 V, and 1.4 V.

4.6.2 Electrochemical Impedance Spectroscopy (EIS) Analysis

Electrochemical impedance spectroscopy (EIS) was used to investigate how the Fe–Ni@BiSFMNi-based cathode behaves under different operating conditions. The EIS measurements show how much resistance arises from different phenomena inside an operating cell. This information is very important for figuring out what steps in CO_2 electrolysis limit performance. Typically, the total resistance can be separated into two main components: R_s, the ohmic resistance, which includes the ionic resistance of the electrolyte and contact resistances; and R_p, the polarization resistance, which reflects the combined effects of charge-transfer reactions, adsorption, and mass transport limitations at the electrodes.

Figure 4.17(a) shows the EIS spectra of the Fe–Ni@BiSFMNi cathode at 800 °C at different voltages (OCV, 1.2 V, and 1.4 V). As the voltage rises, the arc diameter clearly gets smaller (lower R_p) and also shifts a bit to lower resistance (Lower R_s). This pattern shows that charge transfer and catalytic activity are better at higher operating voltages. At 1.4 V, Rs and Rp equals to 0.2 Ω cm^2 and 0.30 Ω cm^2. Figure 4.17(b) shows the Fe–Ni@BiSFMNi and BiSFMNi spectra with the ohmic resistance taken out. Fe–Ni@BiSFMNi has smaller arcs at all working voltages, which confirms that the exsolved Fe–Ni nanoparticles lower polarization resistance, from 0.38 Ω cm^2 for BiSFMNi to 0.3 Ω cm^2 at 1.4 V, by increasing the number of reaction sites on the surface and improving catalytic efficacy. Figure 4.17(c) shows how temperature affects the polarization resistance of the Fe–Ni@BiSFMNi cathode at 1.2 V. As expected, the size of the arc gets bigger resulting in R_p to increase from 0.5 Ω cm^2 to 3.6 Ω cm^2 (at 1.2 V) when temperature decreased from 800 to 700 °C. This shows that higher temperature favors the CO_2 reduction. These EIS results show that nanoparticle exsolution and higher operating temperatures both help reduce polarization losses and make the SOEC work better overall.

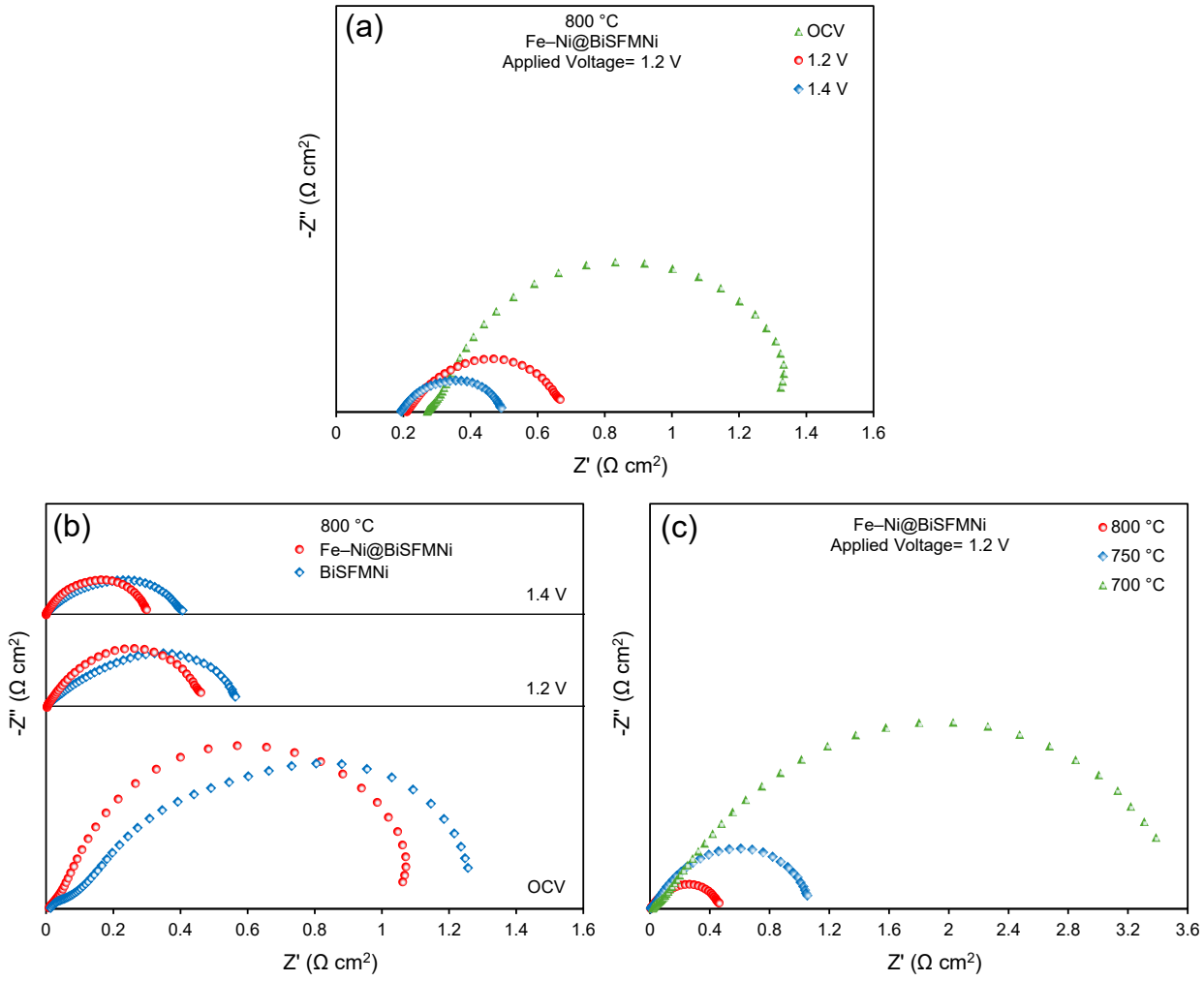


Figure 4.17. Electrochemical impedance spectra (EIS) of (a) cell with Fe–Ni@BiSFMNi at OCV, 1.2 V and 1.4V, (b) Comparison of Fe–Ni@BiSFMNi and BiSFMNi, and (c) Temperature dependence of EIS spectra of Fe–Ni@BiSFMNi at 1.2 V.

4.6.3 Distribution of Relaxation Times (DRT) Analysis

Traditional electrochemical impedance spectroscopy (EIS) is useful for measuring the total resistance of a cell, but it doesn't always have enough precision to tell among overlapping electrochemical processes. To get around this problem, the Distribution of Relaxation Times (DRT) analysis is used. DRT breaks down the impedance spectrum into separate time-constant parts, making it easier to find and assign resistive and capacitive processes in the cell. This method is

very good at breaking down contributions from electrode polarization, gas diffusion, and charge transfer at the interface. By looking at the DRT profiles of the Fe–Ni@BiSFMNi-based SOEC under different operating circumstances, it was able to learn more about how exsolved nanoparticles and temperature might improve performance.

The DRT deconvolution, Figure 4.18, shows four separate peaks, which are linked to electrochemical processes that happen at various characteristic frequencies:

- P1 and P2: is attributed to oxygen ion transfer in electrolyte and interfaces and oxygen evolution at anode [38,42,45,53].
- P3: is associated with surface processes such as CO_2 adsorption, activation, and electrochemical reduction [38,42,45].
- P4: Gass diffusion process [38,42,45].

It is observed that P1, P2, and P4 do not change significantly between samples, suggesting that they predominantly reflect bulk ionic transport and gas diffusion phenomena, which are less sensitive to surface modifications. In contrast, P3 shows a more pronounced change, indicating that it is closely related to CO_2 reduction processes at the cathode surface. The smaller P3 peak for Fe–Ni@BiSFMNi demonstrates that the exsolution of Fe–Ni nanoparticles accelerates CO_2 surface kinetics by enhancing adsorption and activation. The exsolution achieved through reduction treatment increases the number of metal–oxide interfaces and oxygen vacancies, both of which facilitate gas-phase reactions and improve electrochemical surface exchange rates. These results are consistent with the I–V and EIS studies, which showed improved current density and reduced polarization resistance.

The DRT profiles also show the effect of temperature on the performance. As the temperature drops, all the peaks move to lower frequencies and are stronger, which means that the kinetics are

slower, and the resistive losses are larger. The general pattern is that the polarization resistance goes up a lot as the temperature goes down, especially in the low-frequency range where CO_2 reduction happens. This shows how important it is to run SOECs at high temperatures to get the fastest possible reaction rates, even when using better electrodes like Fe–Ni@BiSFMNi.

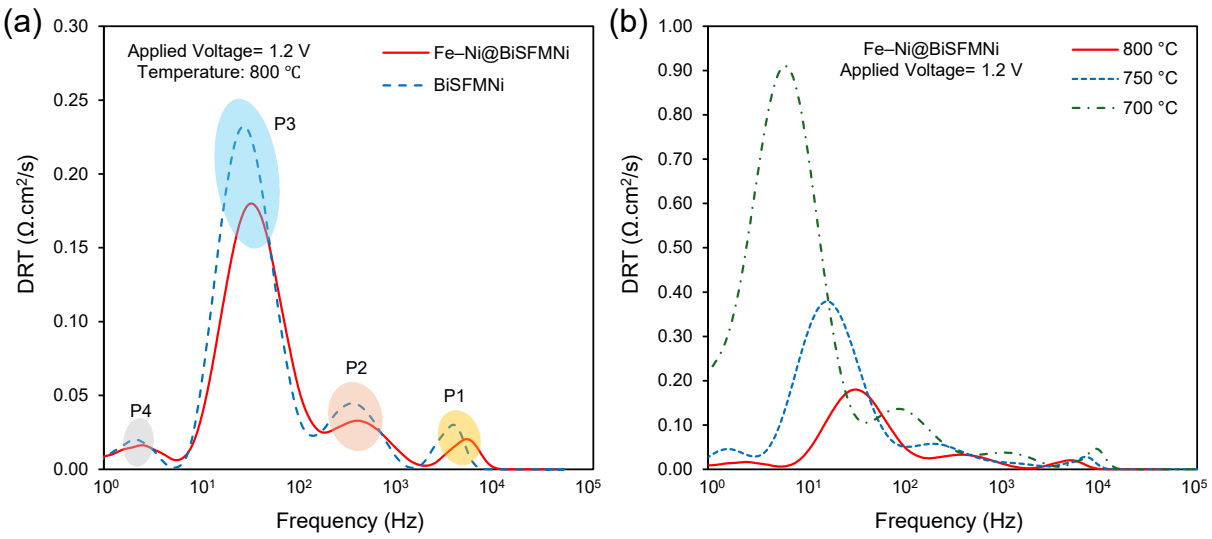


Figure 4.18. DRT spectra: (a) comparison of Fe–Ni@BiSFMNi and BiSFMNi cathodes at 800 °C and 1.2 V, and (b) DRT spectra of Fe–Ni@BiSFMNi at 800 °C, 750 °C, and 700 °C under 1.2 V applied voltage.

4.7 Long-term stability

A long-term electrolysis test was conducted to evaluate the durability of the cell under constant operating conditions. The cell was held at a fixed voltage of 1.4 V, and the current density was monitored continuously for 140 hours. As shown in **Error! Reference source not found.**, a sharp i nitial drop in current density was observed within the first few hours, which can be attributed to the early-stage stabilization of the electrode–electrolyte interfaces and possible restructuring of the electrode surface. Following this initial adjustment, the current density gradually decreased at a very slow rate, indicating minimal degradation over time. This stable performance highlights the

robustness of the cell architecture and the long-term electrochemical stability of the electrode materials under CO_2 electrolysis conditions.

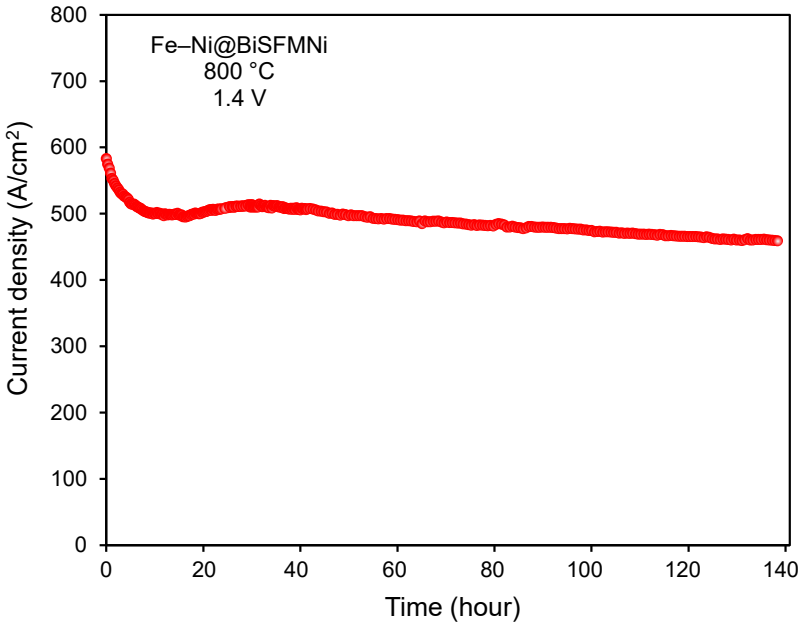


Figure 4.19. Long-term CO_2 electrolysis performance at 1.4 V over 140 hours.

4.8 Performance comparison with literature

Table 4.1 compares the CO_2 electrolysis performance of this work with representative literature reports, showing the change in current density before and after nanoparticle exsolution. In each case, the baseline cell with the pristine perovskite fuel electrode is compared with its nanoparticle-decorated counterpart under identical or comparable testing conditions at 800 °C. Across the studies, the incorporation of exsolved Fe-based alloy nanoparticles (e.g., Fe–Cu, Fe–Co, Fe–Ni, Fe–Ru) is associated with a measurable increase in current density, indicating the beneficial role of surface-active metallic nanoparticles in enhancing CO_2 reduction kinetics. In this work, the Fe–Ni@BiSFMNi electrode showed an increase in current density from 1.0 A/cm² to 1.3 A/cm² at 1.6 V, which is consistent with the improvement trends observed in the literature. It should be noted that the performance reported in this work is neither the highest nor the lowest among published

studies, but it lies within a reasonable range. Direct comparison, however, remains challenging, since even when using the same cathode materials, variations in cell fabrication methods, electrode microstructures, testing setups, and other experimental details can significantly influence the observed performance.

Table 4.1. A comparison of current densities with literature at 800 °C for pure CO_2 electrolysis.

Air electrode	Electrolyte	Fuel electrode	Current density (A/cm^2)	Reference
LSCF-SDC	LSGM	SFCuM Fe–Cu@SFCuM	1.6 at 1.5 V 2.5 at 1.5 V	[42]
BSCF	LSGM	Fe@SFM Fe@SFZnM01	0.7 at 1.5 V 1.6 at 1.5 V	[48]
BSCF-GDC	LSGM	SFMCo-GDC Fe–Co@SFMCo-GDC	0.8 at 1.6 V 1.2 at 1.6 V	[39]
LSCF-SDC	LSGM	SFMNi-F–SDC Fe–Ni@SFMNi-F–SDC	1.4 at 1.5 V 2.7 at 1.5 V	[44]
BSCF-GDC	LSGM	SFRuM-GDC Fe–Ru@SFRuM-GDC	0.9 at 1.6 V 1.3 at 1.6 V	[53]
LSCF–GDC	LSGM	SFMNi-GDC Fe–Ni@SFMNi-GDC	0.6 at 1.6 V 0.9 at 1.6 V	[38]
LSM–YSZ	YSZ	SFM-SDC Fe–Ni@SFMNi-SDC	1.1 at 1.5 V 2.2 at 1.5 V	[37]
BSCF	LSGM	SFM BiSFM	0.6 at 1.6 V 1.1 at 1.6 V	[35]
LSCF–GDC	LSGM	BiSFMNi Fe–Ni@BiSFMNi	1.0 at 1.6 V 1.3 at 1.6 V	This work

4.9 Experimental work conclusion

In conclusion, in-situ exsolution of Fe–Ni nanoparticles on the Bi- and Ni-doped BiSFMNi cathode made the solid oxide CO_2 electrolysis cell perform better, resulting in 30% higher current density. Structural investigations showed that Fe–Ni nanoparticles were successfully formed in a way that made them evenly spread out, and that the host perovskite partially changed into a Ruddlesden–Popper phase. These nanoparticles added more active sites for CO_2 adsorption and reduction, sped up surface exchange kinetics. At 1.6 V and 800 °C, the nanoparticle-decorated cathode (Fe–Ni@BiSFMNi) had a peak current density of 1.3 A/cm², which was higher than the 1.0 A/cm² of the non-nanoparticles BiSFMNi. Electrochemical impedance spectroscopy (EIS) indicated a big drop in polarization resistance, while DRT analysis showed a noticeable drop in low-frequency processes related to surface adsorption and reaction kinetics.

Chapter 5

Simulation Study of DAC-SOEC-Methanol/Synfuel Plant

5.1 Introduction

The 21st century faces an unprecedented challenge: mitigating the harmful effects of increasing atmospheric pollutants, prominently carbon dioxide (CO_2), while simultaneously meeting the escalating global demand for energy and chemicals. Carbon capture and utilization (CCU) technologies offer a promising avenue to address these dual challenges by not only reducing CO_2 emissions but also converting this greenhouse gas into valuable chemical products. Among the various CCU approaches, the integration of direct air carbon capture (DAC) and solid oxide electrolysis cells (SOEC) represents an innovative solution for the sustainable production of liquid hydrocarbons such as syncrude and methanol. DAC technology provides a means to selectively extract CO_2 from ambient air, offering a scalable and environmentally benign approach to carbon capture. The captured CO_2 can then be utilized as a feedstock for chemical synthesis processes, thereby closing the carbon cycle and mitigating the environmental impact of anthropogenic CO_2 emissions [3]. Meanwhile, SOEC technology enables the electrochemical conversion of CO_2, when mixed with water, into syngas (a mixture of carbon monoxide and hydrogen) through co-electrolysis at high temperatures.

Methanol, a versatile fuel and chemical precursor, has attracted the most attention for carbon capture and utilization (CCU) technologies, offering significant potential for sustainable fuel production. Through comparative analyses of CO_2 capture technologies, studies have underscored the cost-effectiveness and environmental benefits of methanol production from DAC [54]. Furthermore, advancements in co-electrolysis and integration with Fischer-Tropsch (FT) synthesis

have positioned methanol as a frontrunner in achieving carbon-negative fuel production by 2030. Wei et al. [55] presented an integrated process utilizing power plant flue gas for methanol production. They considered a methanol production of ~606,000 tonnes/year with low CO_2 emissions with exergy efficiency ranges from 48% to 97%, with the highest exergy destruction in the CO_2 capture unit. Economic analysis shows production costs as 0.52 $/kg that is lower production costs compared to similar renewable energy-based technologies by 65%. This process is suggested for pilot projects or high-tech parks to promote economic and sustainable production. Ferguson et al. [56] explored the feasibility of combining DAC (CO_2 capture from the atmosphere) with co-electrolysis of water and captured CO_2 using a solid oxide electrolyzer cell (SOEC). The study indicates that while methanol production could be carbon-negative, current SOEC capital costs make it unprofitable. However, it is anticipated that by 2030, SOEC capital costs could decrease by half, enabling profitable methanol production. Moreno-Gonzalez et al. [57] assessed pathways for producing syngas from CO_2 captured from air, considering net CO_2 emissions, energy efficiency, and costs. Three DAC to syngas plants are analyzed, utilizing different CO_2 reduction methods. Results showes that while gaseous CO_2-electrolysis offers no advantage over thermolytic reverse water gas shift (rWGS), DAC-(bi)carbonate electrolysis presents the best pathway in terms of net CO_2 emissions. However, it has higher syngas costs compared to other methods. Cost competitiveness could be achieved with improvements in performance and lower electricity and membrane prices. Nonetheless, all CO_2-based alternatives currently entail higher costs than current retail prices for syngas, synfuel, or methanol. Galán et al. [58] compared CO_2 capture technologies, focusing on biomass and DAC, to address rising atmospheric CO_2 levels. It evaluates the techno-economic aspects, considering methanol production as a common endpoint. Biomass offers lower costs due to renewable energy use, but requires significant land and water. Zang et al. [59]

evaluated the techno-economic and environmental aspects of producing low-carbon hydrocarbons through CO_2 capture and utilization. It analyzes integrated methanol–ethanol coproduction, integrated methanol–ammonia coproduction, and stand-alone methanol production systems using CO_2 from ethanol plants, ammonia plants, and general market supply. Greenhouse gas emissions range from 13.6 to 84.6 g CO_2-eq /MJ, compared to 91.5 g CO_2-eq/MJ for conventional methanol from natural gas. The fuel selling price of methanol ranges from \$0.61 to \$1.28/kg, depending on hydrogen price and CO_2 abatement credits. Without credits, hydrogen prices need to be \$0.77–0.95/kg for methanol to equal the average market price (around 0.65 \$/kg [60]). With a \$35/tonne CO_2 credit, the methanol price reduces to \$0.56–0.59/kg. Morimoto et al. [61] evaluated methanol, syncrude, and gasoline for their potential in carbon capture and utilization (CCU) and carbon dioxide removal (CDR) technologies. Results indicate varying levels of CO_2 reduction and product costs across the fuels, with methanol showing an average CO_2 emission reduction of 3.43 kg-$CO_2 \cdot kg^{-1}$ respect to conventional process and an average product cost of 0.82 $\$ \cdot kg^{-1}$.

Syncrude, a synthetic hydrocarbon derived from Fischer-Tropsch (FT) synthesis, represents another promising avenue for sustainable fuel production. Comparative analyses have highlighted syncrude's varying CO_2 reduction potentials and product costs across different CCU and carbon dioxide removal (CDR) technologies. Integration with DAC and renewable energy sources offers opportunities to significantly reduce greenhouse gas emissions, paving the way for its adoption as a key component in the transition to a low-carbon future. Marchese et al. [62] proposed a plant concept integrating DAC technology with Fischer-Tropsch synthesis to produce synthetic hydrocarbons. Different scenarios are analyzed, including energy supply from natural gas or electrification, and off-gas recirculation. The highest system efficiency achieved is 36.3%, with a maximum carbon dioxide conversion of 68.3%. Capital and operating costs are evaluated, with the

minimum Fischer-Tropsch waxes production cost ranging from 6.3 €/kg_{wax} to 5.05 €/kg_{wax}, depending on financial risk and market electricity costs.

D'Adamo et al. [63] studied the levelized cost of producing electrofuels (e-fuels) using renewable energy sources. The process includes DAC, electrolysis, and the Fischer-Tropsch process. The baseline scenario shows an e-fuel cost of around 3.1 €/l, mainly influenced by energy and hydrogen production. While current costs are not competitive with fossil fuels, the development of e-fuels supports environmental protection. Various strategies like incentive policies and technology development could reduce costs, aiding the transport sector's decarbonization. Liu et al. [64] assessed the greenhouse gas emissions of pairing CO_2 DAC with Fischer-Tropsch synthesis to produce diesel fuel. The system emits 0.51 g CO_2-eq per g CO_2 captured from air, or 29 g CO_2-eq per MJ of FT fuel combusted in the baseline scenario. If low carbon electricity is used, this pathway can deliver transport fuels with a lower carbon intensity than conventional diesel production and some biofuel pathways. Labunski et al. [65] analyzed the current and projected greenhouse gas (GHG) emissions of e-fuels produced through electrolysis and Fischer-Tropsch synthesis for use in Germany. Key process steps include feedstock provision, electrolysis (via solid oxide co-electrolysis; SOEC), synthesis (via Fischer-Tropsch synthesis), e-crude refining, and eventual transport and use in Germany. Scenarios for production in Germany project GHG emissions ranging from 2.78–3.47 kg CO_2-eq/L e-fuel in 2021 to 0.064–0.082 kg CO_2-eq/L e-fuel in 2050. Zang et al. [66] conducted a techno-economic analysis of producing Fischer-Tropsch liquid fuel from hydrogen and carbon dioxide using renewable electricity. Results indicate that hydrogen price has the largest impact on the minimum selling price of FT fuel. For instance, to be cost-competitive with petroleum diesel, FT fuel production requires an H_2 price of \$0.8/kg with a CO_2 price of \$17.3/tonne.

This chapter presents a techno-economic and environmental study of a novel CCU system integrating DAC, SOEC, and liquid hydrocarbon production units, with a specific focus on synfuel and methanol. The main rationale for this system configuration is the synergy between the high temperature exhaust of the DAC process and the temperature requirement for the SOEC. The primary objective of this integrated system is to harness atmospheric CO_2 for the synthesis of liquid hydrocarbons, offering a sustainable pathway towards reducing CO_2 emissions and advancing the transition towards a carbon-neutral future. Through simulations using Aspen Plus, this research investigates the techno-economic feasibility of the proposed CCU system for synfuel and methanol production, focusing on key operational parameters and economic considerations.

5.2 Process overview

The system's primary objective is to produce chemicals by capturing CO_2 from the atmosphere. This chapter explores two case studies: CO_2 to Methanol and CO_2 to synfuel. Each case study involves three main components: DAC, solid oxide electrolysis cell (SOEC), and either a methanol production plant or a Fischer-Tropsch unit. The DAC unit, based on the design by Carbon Engineering [67], draws in atmospheric air, where approximately 75% of the CO_2 is absorbed before being transferred to the SOEC unit along with steam. The SOEC unit utilizes renewable electricity to co-electrolyze CO_2 and H_2O, producing syngas (mixture of primarily CO and H_2). This syngas serves as the feedstock for chemical production, either methanol or synfuel, with specific syngas ratios tailored for each product. For methanol production the syngas ratio of $(H_2\text{-}CO_2)/(CO+ CO_2)$ is kept at 2 while for synfuel production the ratio of H_2/CO is kept at 2. An important feature of this configuration is heat recovery and integration where the hot output air from the SOEC's anode section is utilized as a heat source in the methanol production process, reducing the need for additional methane burning as a preheat source. Another feature is the

capture and utilization of any CO_2 generated during the process from natural gas oxy-combustion. In both case studies, the exhaust gas containing CO_2 is recycled to the calciner of the DAC unit. Figure 5.1 presents a simplified flow chart of the two case studies, while more detailed technical information about the Aspen Plus models is provided in subsequent sections and Table A.2 in Appendix.

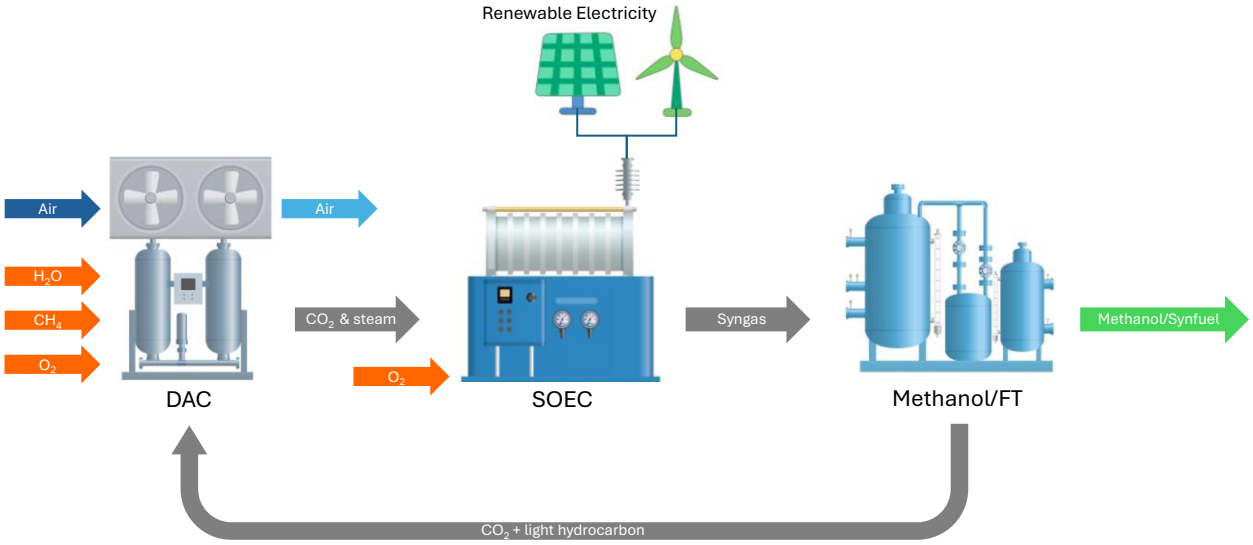


Figure 5.1. Overall direct air capture to fuel plant configuration.

5.2.1 Direct air capture (DAC) model

The DAC model is based on the design by Carbon Engineering [67]. As shown in Figure 5.2, the DAC system has two loops: the first encompasses an air contactor/absorber and a pellet reactor for CO_2 capture; the second involves the pellet reactor, a cyclone, a calciner, and a slaker reactor. In the air contactor, CO_2 (400 ppm in air) is extracted from the surrounding air using an aqueous alkali solution containing OH^-, CO_3^{2-}, K^+, resulting in K_2CO_3 (aq) formation. The capture efficiency for this component is designed as 73.5% of the CO_2 in the form of K_2CO_3(aq) [67]. The calcium loop regenerates the alkali solution through the precipitation of CO_3^{2-} reacting with Ca^{2+} from $Ca(OH)_2$ in the pellet reactor, leading to $CaCO_3$ formation. The $CaCO_3$ pellets enter an

oxygen-fired calciner (95.6% O_2, 4.4% N_2) with a $CaCO_3$-to-CaO conversion efficiency of 98%. Subsequently, the CO_2/steam stream leaving the calciner is fed to the SOEC unit. The complete combustion of natural gas the calciner thermally supports the endothermic decomposition of $CaCO_3$ pellets, facilitating adiabatic operations in the calciner. In the slaker the solid CaO is hydrated to form $Ca(OH)_2$(aq), which is then directed to the pellet bed to react with K_2CO_3.

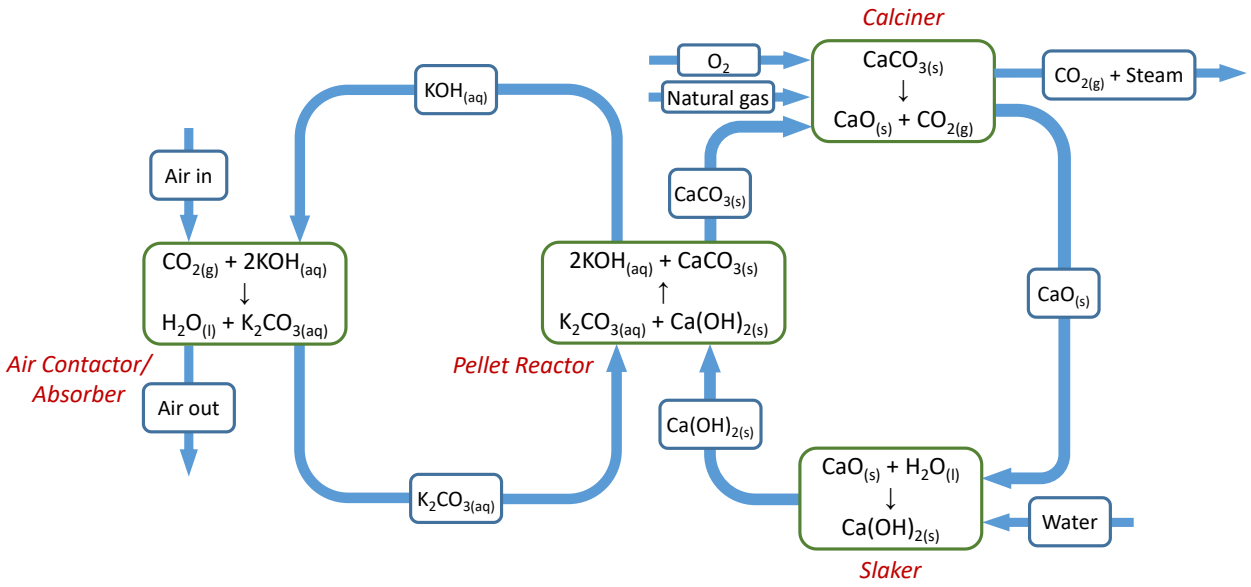


Figure 5.2. Reactions occurring in the DAC unit.

Although the DAC model is based on Carbon Engineering design [67], some changes and simplification were made in the Aspen Plus simulation. These changes made the plant become more like a pulp and paper Kraft process. For example, mixing tanks are used instead of a fluidized bed causticizer presented in the Carbon Engineering design. Also, the fluidized bed calciner was replaced with a rotary kiln.

The schematic of the DAC Aspen model is depicted in Figure 5.3. The absorber component is simulated by integrating a combination of Separator and RGibbs blocks. The causticizer is represented by an RGibbs block. A HyCyc block is utilized to simulate the hydrocyclone. The

dried cake is directed to the calciner including a rotary kiln and burner assembly using a hierarchy block comprising RStoic and Heater blocks as shown in Figure 5.4. A design specification block is employed to maintain the kiln temperature at 900°C by regulating the methane fuel burned, ensuring a net heat of 0 for the calciner (Q stream in Figure 5.4). The natural gas burner is assumed to achieve complete combustion, and a conversion rate of 98% is set for the kiln [67]. The flue gas is directed to the SOEC process. Subsequently, the slaked lime is cooled to prevent rapid boiling in the slaker. The slaker is modeled as an RStoic block with a conversion rate of 85% [67]. The resulting calcium hydroxide is recycled back to the causticizer.

The DAC system inherently requires a substantial land footprint because of the low concentration of CO_2 in the atmosphere, which limits the amount of CO_2 that can be captured per unit volume of air processed. This large footprint is a well-known characteristic of DAC technology and poses challenges in terms of land use and scalability, especially when compared to other components of the plant, which generally have more compact designs. The present study is assuming no limitation in terms of land footprint, which we acknowledge can be a major issue in some jurisdictions.

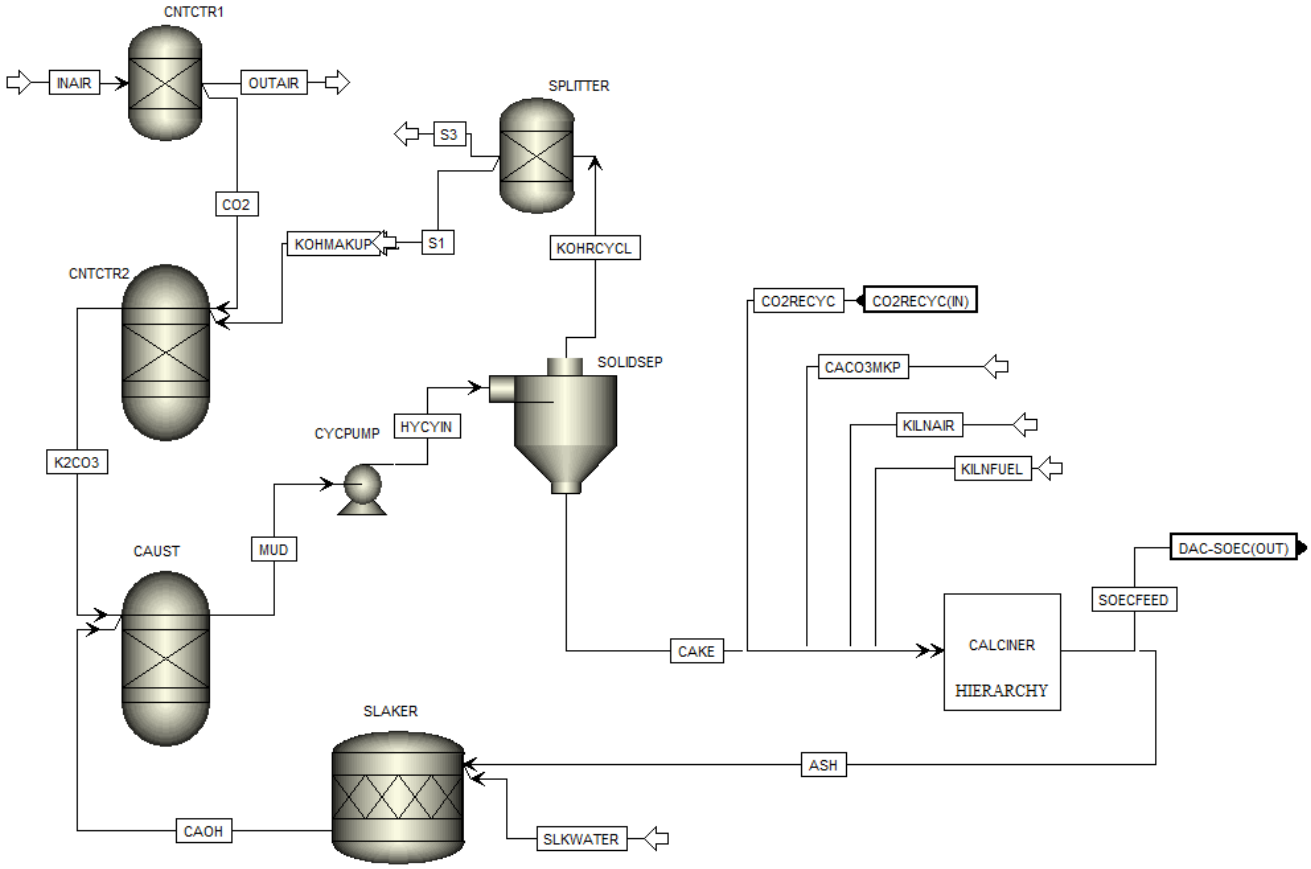


Figure 5.3. Aspen plus model of DAC.

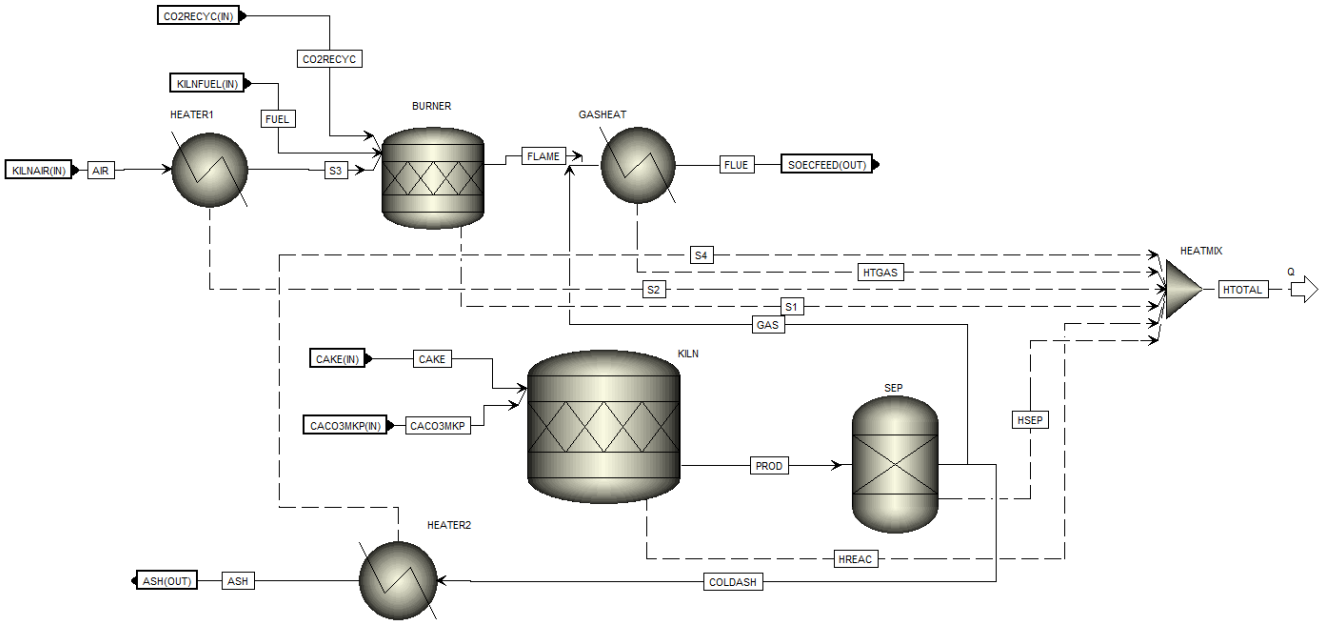


Figure 5.4. Aspen Plus model of Calciner.

5.2.2 SOEC model

Since carbon monoxide and hydrogen are needed to produce methanol/synfuel, co-electrolysis of carbon dioxide and water was chosen. In SOECs, co-electrolysis involves the simultaneous splitting of CO_2 and H_2O into their respective components: carbon monoxide (CO), hydrogen (H_2), and oxygen (O_2). This process occurs at high temperatures and is driven by applying a DC voltage across the electrodes. The reactions in anode and cathode are as follows:

Cathode:

$$H_2O + 2e^- \rightarrow H_2 + O^{2-} \quad (1)$$

$$CO_2 + 2e^- \rightarrow CO + O^{2-} \quad (2)$$

Anode:

$$2O^{2-} \rightarrow O_2 + 4e^- \quad (3)$$

Besides the electrochemical reaction, the gas at the fuel electrode will also experience the reverse water gas shift (rWGS) reaction (Eq. 4) on the surface of a porous electrode catalyst, such as a nickel (Ni).

$$H_2 + CO_2 \underset{\leftarrow WGS}{\overset{RWGS \rightarrow}{}} H_2O + CO \quad (4)$$

At the operating temperature of 800°C, the rWGS kinetics is faster than that of the CO_2 electrochemical reduction (Eq. 2) [68]. Therefore, only water electrochemical reduction was considered, CO arising only from rWGS reaction. The equations to calculate cell voltage, required power and heat and cell characteristics are presented in Table 5.1 and Table 5.2.

Table 5.1. Fundamental equations for the simulation of the SOEC [68–72].

Term	Equation	Eq.
Reversible (Nernst) voltage	$$\mathrm{U_{rev}} = \frac{-\Delta g^0(T) + RT\ln\left(\frac{\left(p_{H_2}p_{O_2}^{0.5}\right)}{p_{H_2O}}\right)}{n_e F}$$ p, $-\Delta g^0$ and F are partial pressure of components, Gibbs free energy at standard pressure and temperature and Faraday constant, respectively.	(5)
Ohmic resistance	$$V_{ohm} = j\left(\frac{\delta_{el}}{\sigma_{el}} + r_{ohmic,\mathrm{cond}}\right)$$ $$\sigma_{el} = \sigma_{0,el}e^{-\frac{E_{act,el}}{RT}}$$ $$j = \frac{i}{A_{cell}}$$ $r_{ohmic,\mathrm{cond}}$ is ohmic resistance of electron-conducting elements δ_{el} and σ_{el} are thickness and inverse of conductivity of electrolyte, respectively.	(6)
Activation overvoltage	$$V_{act,k} = \frac{2RT}{nF}\sinh^{-1}\left(\frac{j}{2j_{0,k}}\right)$$ $$j_{0,k} = \gamma_{0,k}e^{-\frac{E_{act,k}}{RT}}$$ $j_{0,k}$ is exchange current density of electrode k refers to fuel or oxygen electrode	(7)
Concentration overvoltage	$$V_{conc,FE,SOEC} = \frac{RT}{2F} * \ln\left(\frac{1 + j\left(\frac{RT}{2F}\frac{\delta_{FE}}{D_{eff,H_2O} * p_{\mathrm{H_2},bulk}}\right)}{1 - j\left(\frac{RT}{2F}\frac{\delta_{FE}}{D_{eff,H_2O} * p_{H_2O,bulk}}\right)}\right)$$ $$V_{conc,OE,SOEC} = \frac{RT}{4F} * \ln\left(1 + j\left(\frac{RT}{4F}\frac{\delta_{OE}}{D_{eff,O_2} * p_{O_2,bulk}}\right)\right)$$ δ and D_{eff} are thinknes of electrode and effective diffusion coefficient.	(8)
Power required	$$i = 4 \times \dot{n}_{O_2} \times F$$ $$V_{cell} = U_{rev} + V_{ohm} + V_{act} + V_{conc}$$ $$\dot{W} = i \times V_{cell}$$	(9)
Heat required	$$U_{tn} = -\frac{\Delta\dot{H}_{reactant} + \Delta\dot{H}_{oxidant}}{i}$$ $$\dot{Q} = i(V_{cell} - U_{tn})$$	(10)

Table 5.2. Characteristics of the SOEC stack [68–70].

Parameter	A
A_{cell}	0.1 m^2
$\gamma_{0,\mathrm{FE}}$	1.344×10^{10} A/m^2
$\gamma_{0,\mathrm{OE}}$	2.051×10^{9} A/m^2
$E_{act,\mathrm{FE}}$	100,000 J/mol
$E_{act,\mathrm{OE}}$	85,634 J/mol
$E_{act,\mathrm{el}}$	120,000 J/mol
$r_{ohmic,\mathrm{cond}}$	5.7×10^{-6} Ω.m^2
$\sigma_{0,el}$	33,330 (Ω.m)$^{-1}$
δ_{el}	1.25×10^{-5} m
δ_{FE}	3.2×10^{-5} m
δ_{OE}	1.75×10^{-5} m

The schematic of the SOEC Aspen Plus model is shown in Figure 5.5. As Aspen Plus cannot directly model an electrolyzer cell, equipment that closely mimics actual operating conditions was chosen. Since the processes inside the cell reach equilibrium, RStoic reactors are used for equilibrium processes. Electrochemical reactions were represented using an RStoic reactor, without accounting for ion formation. To obtain the amount of electricity and heat needed for the operation of the cell, a calculation block was designed in Excel and compiled into Aspen Plus software; the corresponding equations listed in Table 5.1. A separator unit was used to model the electrolyte, whose duty is to separate oxygen from other components. Since the cell operates under isothermal conditions, hot air was supplied to compensate for the heat absorbed by the reactions. For the heat balance, the heat capacity of the COOLER is equal to the sum of the heat consumed in the EQUIBOUT and the heat needed for the electrochemical reactions.

SOEC works at a high temperature of 800°C that is the same temperature as the products of the DAC process, which is an advantage of coupling these two. The air input, however, needs to be

brought to 900°C before entering the anode (a 100°C temperature drop is assumed through the cell). For this reason, three preheaters have been implemented. The hot output streams of the cathode and anode are used as the heat source for the first two preheaters. A part of the product of the cathode is mixed with a portion of the input to the cathode and oxygen at mixer B7 and then fed to a RStoic to burn and produce heat in the preheater 2 and then sent back to the cathode.

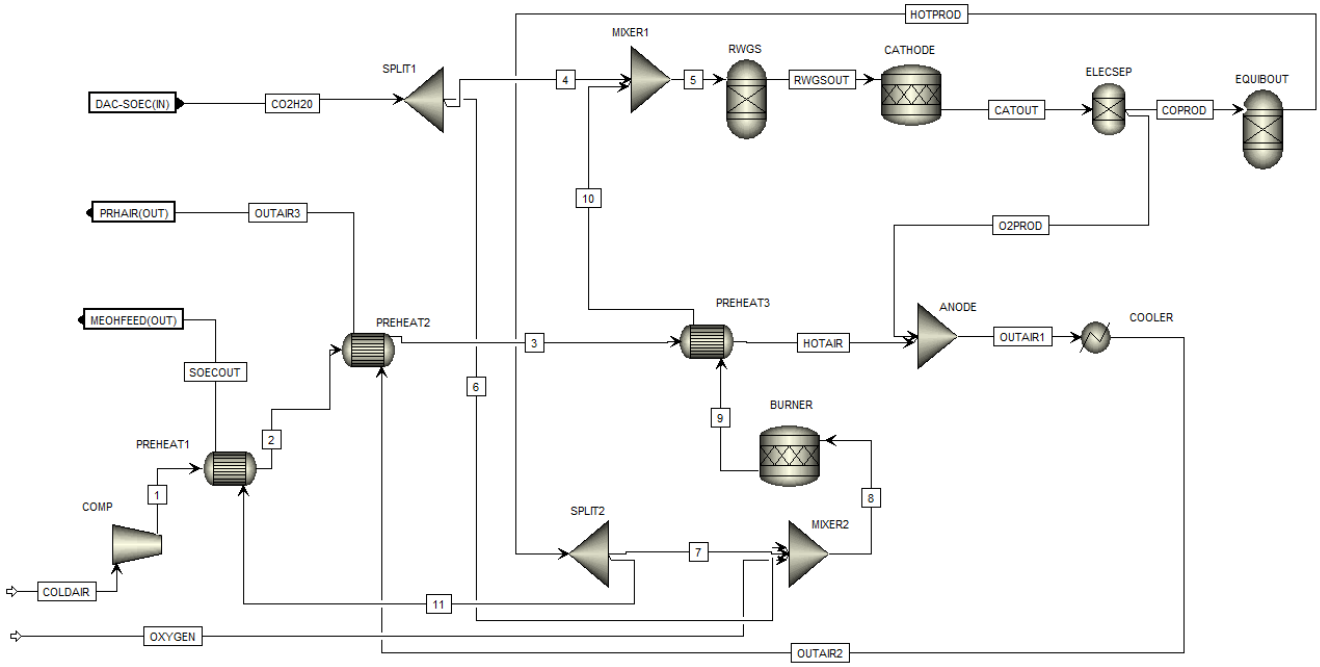


Figure 5.5. SOEC Aspen Plus Model.

5.2.3 Methanol production model

Figure 5.6 shows the Aspen Plus flowsheet of the methanol production process. Before the output stream of the SOEC enters the methanol production reactor, the excess water should first be removed with the help of a flash distillation unit. Then, the pressure of the stream is increased to 70 bar [73] (with a resulting increase in temperature to 232°C). A packed-bed reactor is considered for the methanol reactor. The product of the reactor then enters a cooler and transfers its heat to water and leaves it at 40°C. The output stream of the reactor contains CO, H_2 and CO_2 along with

methanol and water. Using flash distillation, the unreacted gaseous components are separated and recirculated into the reactor again. This stream is first preheated in PREHEAT1 and then heated up further by the hot air coming from the SOEC.

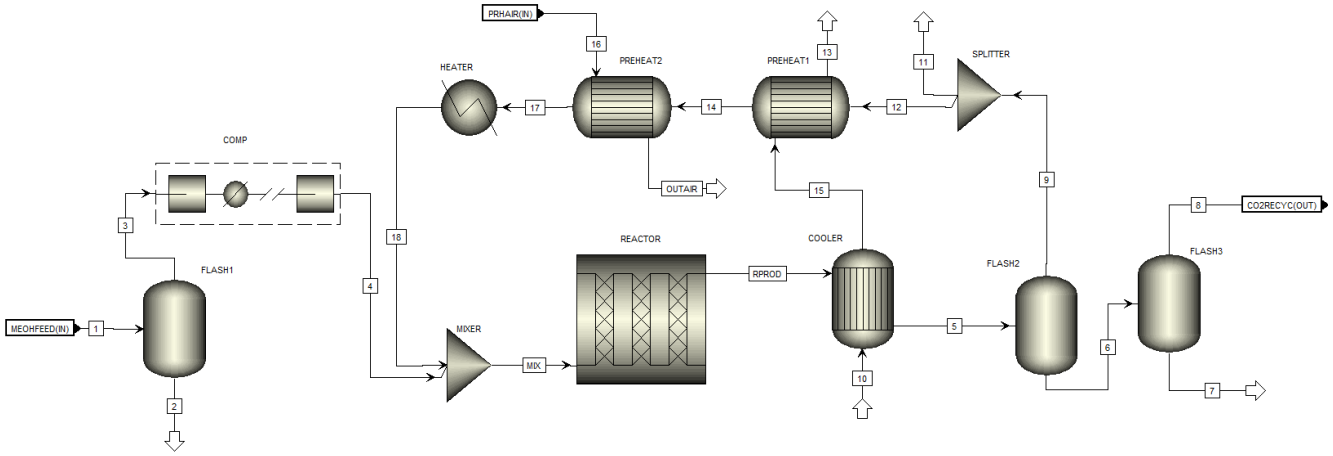


Figure 5.6. Methanol production Aspen model.

The reactions carried out in the methanol reactor are as follows:

$$CO + 2H_2 \leftrightarrow CH_3OH$$

$$CO_2 + 3H_2 \leftrightarrow CH_3OH + H_2O \quad (11)$$

$$CO_2 + H_2 \leftrightarrow CO + H_2O$$

The following kinetics are used in the simulation [74]:

$$r_{CO} = \frac{k_1 K_{CO}\left[f_{CO} f_{H_2}^{3/2} - \frac{f_{CH_3OH} f_{H_2}^{1/2}}{K_{P1}}\right]}{\left(1 + K_{CO} f_{Co} + K_{CO_2} f_{CO_2}\right)\left[f_{H_2}^{1/2} + \left(\frac{K_{H_2O}}{K_{H_2}^{1/2}}\right) f_{H_2O}\right]} \quad (12)$$

$$r_{CO_2} = \frac{k_2 K_{CO_2}\left[f_{CO_2} f_{H_2}^{3/2} - \frac{f_{CH_3OH} f_{H_2}^{1/2}}{K_{P2}}\right]}{\left(1 + K_{CO} f_{Co} + K_{CO_2} f_{CO_2}\right)\left[f_{H_2}^{1/2} + \left(\frac{K_{H_2O}}{K_{H_2}^{1/2}}\right) f_{H_2O}\right]} \quad (13)$$

$$r_{gas\ shift} = \frac{k_3 K_{CO_2}\left[f_{CO_2} f_{H_2} - \frac{f_{H_2O} f_{Co}}{K_{P3}}\right]}{\left(1 + K_{CO} f_{Co} + K_{CO_2} f_{CO_2}\right)\left[f_{H_2}^{1/2} + \left(\frac{K_{H_2O}}{K_{H_2}^{1/2}}\right) f_{H_2O}\right]} \quad (14)$$

The constants for the above equations are presented in Table 5.3.

Table 5.3. Kinetic constants for methanol production reactions [74].

Parameter	A	B
k_1	4.89e7	-11300
k_2	1.09e5	-87500
k_3	9.64e11	-152900
K_{CO}	2.16e-5	46800
K_{CO_2}	7.05e-7	61700
$K_{CO}/K_{H_2}^{1/2}$	6.37e-9	84000
K_{P1}	5139	12.621
K_{P2}	3066	10.592
K_{P3}	2073	-2.029
$k = Aexp(^{B}/_{RT})$		
$K = Aexp(^{B}/_{RT})$		
$K_P = 10^{\frac{A}{T}-B}$		

5.2.4 Fischer-Tropsch model

Figure 5.7 shows the flowsheet of the Fischer–Tropsch process. Eqs. (15-17) provides the main reactions of the Fischer–Tropsch synthesis.

$$nCO + (2n+1)H_2 \rightarrow C_nH_{2n+2} + nH_2O \quad (15)$$

$$nCO + 2nH_2 \rightarrow C_nH_{2n} + nH_2O \quad (16)$$

$$CO + H_2O \rightarrow CO_2 + H_2 \quad (17)$$

The FT reactor with low temperature conditions was operated at a temperature of 230℃ and a pressure of 25 bar. The syngas feed was transformed into synthetic hydrocarbons through catalytic

reactions involving CO and H_2. Prior to entering the FT reactor, the syngas underwent compression to reach the desired operating pressure.

The Fischer–Tropsch (FT) products were modeled using a modified Anderson–Schulz–Flory (ASF) distribution, as described by Eq. (18) [75]. This modified version accounts for increased methane (CH_4) production, decreased ethylene (C_2H_4) formation, and a more linear distribution for hydrocarbons with carbon numbers above C_{20}, compared to the classical ASF theory. The key design parameter in this model is the chain growth probability (α), which determines the product spectrum of the FT reactor. According to FT kinetics, the maximum yield of C_{10}–C_{20} hydrocarbons is approximately 40% when α = 0.85. For enhanced production of long-chain hydrocarbons, a higher α value is required - in this simulation, α = 0.94 was selected [76].

$$W_n = n\alpha^{(n-1)}(1-\alpha)^2 \tag{18}$$

The ASF distribution does not differentiate between olefins and paraffins; instead, it predicts the overall fraction W_n of products with carbon number *n*, which includes both n-sized paraffins and olefins. The molar ratio between olefins and paraffins at a given chain length *n* is determined using an exponential decay relationship shown in Eq. (19):

$$\frac{W_{n,O}}{W_{n,P}} = e^{-0.3n} \tag{19}$$

A single-pass CO conversion of 90% was assumed [72], with an H_2/CO feed ratio of 2:1 into the FT reactor. The reactor effluent contained unreacted CO, H_2, CO_2, steam, and a range of hydrocarbon products — including alkanes up to C_{50} and alkenes up to C_{20}. A three-phase separator operating at FT reactor pressure and ambient temperature was used to split the effluent into three streams: (i) light FT off-gases (C_1–C_7 hydrocarbons along with CO, CO_2, and H_2), (ii) liquid hydrocarbon products, and (iii) water. The FT off-gas was directed to the DAC section, where hydrocarbons were combusted to generate energy and the resulting CO_2 was captured.

A 90% CO conversion per-pass was considered [77], with an H_2/CO feed ratio of 2:1 into the FT reactor. The reactor effluent contained unreacted CO, H_2, CO_2, steam, and a range of hydrocarbon products — including alkanes up to C_{50} and alkenes up to C_{20}. A three-phase separator operating at FT reactor pressure and ambient temperature was used to split the effluent into three streams: (i) light FT off-gases (C_1–C_7 hydrocarbons along with CO, CO_2, and H_2), (ii) liquid hydrocarbon products, and (iii) water. The FT off-gas was directed to the DAC section, where hydrocarbons were combusted to generate energy and the resulting CO_2 was captured.

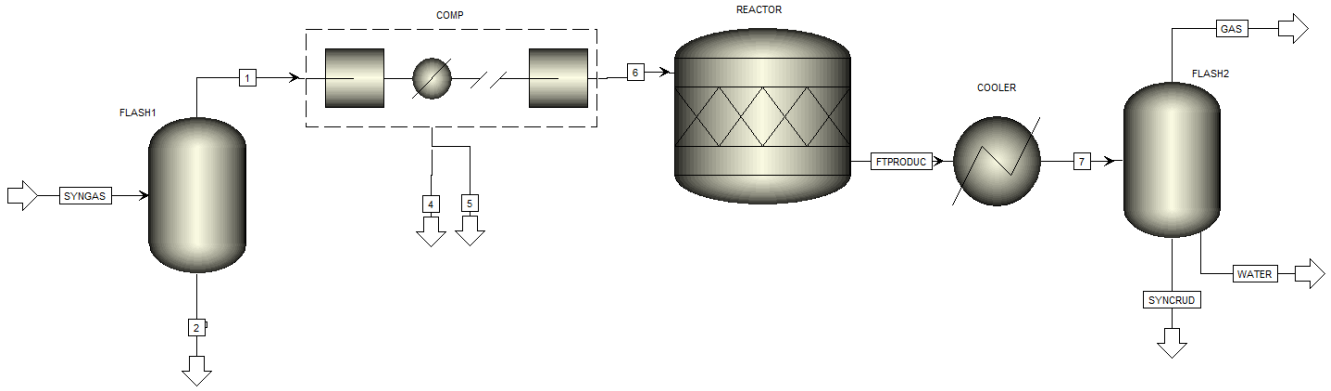


Figure 5.7. Aspen Plus model of Fischer-Tropsch unit.

5.3 Methodology

The primary methodology for this study involved the simulation of the system using Aspen Plus software. For most sections of the process, the Non-Random Two-Liquid (NRTL) property method was used. However, for the DAC unit, which involves solid components, the SOLIDS property method was employed to represent the thermodynamic behavior of solid-liquid-gas interactions. In the DAC unit, a design specification was used to maintain the correct mass balance within the KOH loop. Additionally, in the SOEC section, a design specification adjusted the cold air inlet flow rate to ensure that the inlet temperature to the cell was maintained at 900°C. Following the system simulation, an economic analysis was conducted to evaluate the financial viability of the

process. This analysis included estimating the capital costs for equipment, calculating the operational cost such as utilities and operating and maintenance. Then, sensitivity analysis was performed to understand the impact of key economic parameters on the overall feasibility. Finally, to evaluate the environmental impacts of the process, net CO_2 emission was determined.

5.3.1 Economic analysis

All costs reported here are in 2023 US dollars. For the economic analysis, we consider two main sources of expenses: cost of equipment and operating costs. For equipment costs, either a cost equation is used or, when knowing an equipment cost for a certain size, it is estimated by Eq. (20):

$$Z_{equip} = Z_{ref} \times \left(\frac{A}{A_{ref}}\right)^{m} \tag{20}$$

where Z_{ref} and A_{ref} are the installed cost and size of the reference equipment, m is a scaling factor around 0.6-1. Table 5.4 presents the cost parameters for each equipment. Then, the costs are updated to the current year using the cost index:

$$Z_{equip,present} = Z_{equip} \times \frac{CEPCI_{2023}}{CEPCI_{ref}} \tag{21}$$

where CEPCI is the chemical engineering plant cost index. To convert the investment cost to an annual cost accounting for the entire lifetime of the equipment, the depreciation cost is calculated:

$$C_{equip,annual} = Z_{equip,present} \times \frac{i \times (i+1)^{n}}{(i+1)^{n} - 1} \tag{22}$$

where $C_{equip,annual}$ is the annualized capital cost (\$), i is the annual interest rate and n is the plant lifetime.

It is assumed that the DAC and Methanol/FT unit won't need to be replaced during the 25 years project life. However, the SOEC system is a newer technology and currently cannot last 25 years. It is assumed for the base case that the SOEC cells have a lifespan of 5 years, requiring replacement

4 times over the 25-year plant lifetime. However, to account for advancements in technology and economies of scale, a 30% reduction in the cost of SOEC cells is assumed every 5 years. This means that with each replacement, the cells become progressively cheaper. All the necessary economics parameters for annualized capital cost calculation are presented in Table 5.5. These values are considered for the base case, which will be looked at in more detail in parametric analysis.

Table 5.4. Equipment purchase cost.

Equipment	Base cost (Million $)	Base capacity	Scaling factor	Year-Reference
DAC	786.2	0.98 Mt-CO_2/year	0.8	2018-[67]
SOEC	1198	2000 MW	1	2023-[78]
Methanol	19.8	131 (tonne/day)	0.8	2023-[79]
FT unit	55.4	351 (tonne/day)	0.8	2021-[66]

Table 5.5. Economic parameters assumed in the base case.

Term	Value
Plant lifetime	25 years
Interest rate	10%
SOEC lifespan	5 years
SOEC price reduction	30%/5-years

Operating cost:

The operating cost consists of utilities like natural gas, electricity and water and also operation and maintenance costs. It is assumed that the electricity is generated from non-to low-CO2 emitting sources. The price for these utilities is presented in Table 5.5.

To account for operation and maintenance cost (O&M), 2% of equipment cost is added to the annual costs.

$$C_{op} = C_{utility} + 0.02 * Z_{equip,present} \quad (23)$$

Table 5.6. Electricity market price of different renewable sources.

Sources	Value	Reference
Natural gas	9.87 ($/MWh)	[80]
Process water	0.48 ($/tonne)	[81]
Electricity:		
Ontario grid	72.3 ($/MWh)	[82]
Photovoltaic	64.15 ($/MWh)	[62]
Hydropower	44.34 ($/MWh)	[62]
Geothermal	58.07 ($/MWh)	[62]
Wind	48.6 ($/MWh)	[62]
Concentrated solar power	171.70 ($/MWh)	[62]

5.3.2 Net CO2 equivalent emission assessment

CO_2 equivalent (CO_2-eq) is a widely used metric to quantify the greenhouse gas (GHG) emissions associated with input resources such as electricity and natural gas. The use of CO_2-eq for input resources provides an assessment of the environmental impact in production and distribution. Table 5.7 presents the emission factors used in this research. CO_2-eq emissions from electricity are dependent on the energy mix used in the regional grid (e.g., coal, natural gas, renewable sources) or each renewable sources.

Table 5.7. Emission factors of resources used in this research.

Resource	Emission factor	Reference
Electricity		
Ontario grid (gCO_2-eq /kWh)	30	[83]
Solar PV (gCO_2-eq /kWh)	33	[83]
Solar thermal (gCO_2-eq /kWh)	23	[83]
Wind (gCO_2-eq /kWh)	12	[83]
Hydropower (gCO_2-eq /kWh)	4	[83]
Geothermal (gCO_2-eq /kWh)	37	[83]
Process water	0.32	[83]
Natural gas (gCO_2-eq /kg)	2955	[84]

5.3.3 Key performance indicators

To measure the performance of a new plant, we should consider a series of performance indicators to assess the advantage of the new plant over conventional ones. For the proposed plant the following three performance indicators are considered:

- The first performance indicator is for the plant to be carbon negative. This means that the amount of carbon input to the plant is greater than the output amount and the difference has been converted into a useful product.
- The second one is the energy efficiency of the system. It considers the ratio of output to input energy and shows how a system is performing.
- The third performance indicator, which is often the most important and determines the implementation of a new idea, is that the manufactured product should compete with the product of other manufacturers in terms of price.

To assess the performance of the system with respect to CO_2 emission, an environmental indicator is defined as CO_2 capture per amount of product, or CCPP, with the unit of kilogram of

captured CO_2 per kilogram of the methanol or synfuel production.

$$CCPP = \frac{Carbon\ entering\ the\ systems - carbon\ exiting\ the\ system}{Chemicals\ produced} \quad (24)$$

The specific energy consumption (SEC) was estimated in terms of products (methanol or synfuel), and expressed as GWh/$kt_{product}$:

$$SEC_{product} = \frac{\dot{m}_{NG}.LHV_{NG} + PEF * W_{elec}}{\dot{m}_{product}} \quad (25)$$

where $\dot{m}$ and W_{elec} are mass flow rate (kg/s) and electricity (kW), respectively. Primary energy factor (PEF) describes the efficiency of converting energy from primary sources (e.g. coal, natural gas) to a secondary energy carrier (electricity). From the Ontario grid mix [85] and the PEF factor for each technology [86], the weighted PEF is 2. The subscripts *product* and *NG* refers to the fuel produced (methanol or synfuel) and natural gas input, respectively. The economic indicator is the levelized production cost (LPC), represented as the ratio of the total annual cost per unit mass of chemical produced:

$$LPC = \frac{C_{equip,annual} + C_{opt}}{\dot{m}_{product}} \quad (26)$$

5.4 Results and discussion

The overall simulation was based on a DAC capacity to capture 250,000 tonnes of CO_2 per year. In this study, a base case (Table 5.5) is considered to serve as the reference configuration for our parametric analysis.

5.4.1 Base case results

The results for the base case detailing the utility requirements are presented in Table 5.8, providing insights into the energy consumption and resource utilization of the system. In the DAC-SOEC-

MeOH case, the production process demands 403 MW of electricity and 10.9 tonnes per hour of natural gas. Compared with the synfuel case, the methanol production system requires less utilities because of the smaller size of the plant. Conversely, in synfuel production, a greater amount of CO_2 is recycled, necessitating higher utility usage. However, methanol production entails a larger CO_2 purge, resulting in less CO_2 being recycled. In the methanol case, the production rate amounts to 36.4 tonne/hr of methanol, with the product stream containing approximately 87% of all carbon introduced into the system (from direct air capture and burnt natural gas), whereas for the synfuel case, the production is 15.1 tonne/hr with only 1% purged carbon.

To gauge the energy efficiency of the production process, the SEC indicator is provided in Table 8. The SEC for methanol production is calculated at 26.0 kWh per kilogram of methanol, while for synfuel, it stands at 53.9 kWh per kilogram of synfuel.

Table 5.8. Required supplies and production for the base case.

Parameter	Methanol	Synfuel
Electricity input (MW)	403	360
Natural gas input (tonne/hr)	10.9	7.09
Process water (m^3)	68.8	60.7
Production (tonne/hr)	36.4	15.1
SEC (kWh/kg-product)	26.0	53.9

5.4.2 Economic analysis results

Table 5.9 and Figure 5.8 present both equipment and operating costs to produce methanol and synfuel. The total annual cost for methanol production amounts to 346 million dollars, while for synfuel, it stands at 301 million dollars. As seen in Figure 5.8, a breakdown reveals that approximately 64.9% of the total annual cost is attributed to utilities, 29.7% to utilities, and the remaining 5.4% to operations and maintenance (O&M) expenses. Interestingly, the solid oxide

electrolysis cell (SOEC) accounts for 65-67% of the equipment cost, whereas DAC technology represents 24-28%. This distribution is expected, considering that SOEC and DAC technologies are relatively new compared to the established Methanol and Fischer-Tropsch production units. The levelized cost of production for methanol and synfuel are calculated at 1.32 dollars per kilogram of methanol and 2.78 dollars per kilogram of synfuel, respectively. The results of the simulation indicate that the production costs for methanol and synfuel are higher than current market prices, which are $0.65/kg [60] (103% higher) and $1.92/kg [87] (45% higher), respectively. This suggests that the simulated plant design, utilizing novel technology, is efficient and cost-effective. The lower prices demonstrate the potential for the plant to be competitive in the real world, offering a more economical alternative to existing production methods while maintaining performance standards. Other studies provide a range of costs for similar technologies. D'Adamo et al. [63] reports synfuel production costs of $3/l (our case: $2.1/l), and Fulham et al. [54] estimates methanol production costs at $0.96/kg (our case: $1.32/kg). The lower LCP in their research compared to the present work is primarily due to the electricity source they chose, being a wind farm as part of their facility. In that way, their electricity cost was much lower than this work. These differences can also arise from factors such as the scale of production and the specific technologies used.

Table 5.9. Investment cost of different units and levelized cost of production.

Unit	Methanol	Synfuel
Total installed capital cost (Million $)	931	822
Annualized equipment cost (Million $/yr):		
DAC	25.1	25.1
SOEC	68.5	59.2
MeOH	9.07	-
FT	-	6.25
Utilities (Million $/yr)	224	194
O&M (Million $/yr)	18.6	16.4
Total Annual cost (Million $/yr)	346	301
LCP ($/kg)	1.32	2.78

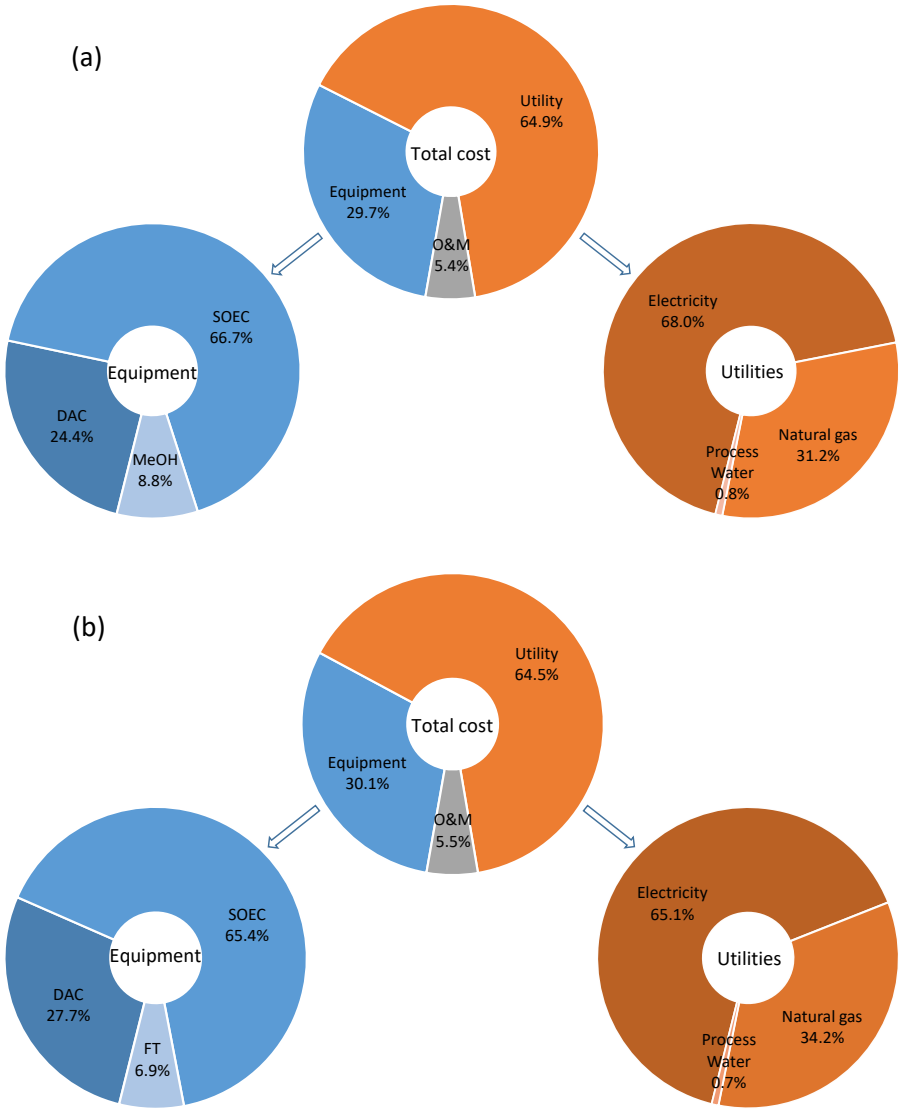


Figure 5.8. Contribution of each part to the capital cost for (a) methanol and (b) synfuel case studies.

The choice of the source of electricity significantly impacts the operational costs of industrial plants. Renewable energy, such as wind and solar, can offer long-term cost savings through fixed-price contracts and reduced dependence on fluctuating fossil fuel prices. Moreover, investments in renewable energy technologies can support the resilience of industrial operations against future energy price shocks and carbon pricing mechanisms, positioning them favorably in the transition to a sustainable energy future.

The results shown in Table 8 are for the base case, where some parameters, such as replacement period of SOEC, may be considered conservative. A sensitivity analysis of key parameters is, therefore, necessary to understand the possible future LCP for such a process. Figure 5.9 shows the effect of using different sources of electricity on the LCP, based on the cost data lsited in Table 5.6. As shown in Figure 5.9, the LCP is the lowest when Hydropower is used. The other renewable energy sources like wind, geothermal and photovoltaic result in comparable LCP to Hydropower. However, concentrated solar power has an unreasonable effect on the LCP. On the other hand, the benefits of these renewable energies will be evident in the environmental analysis in the next section.

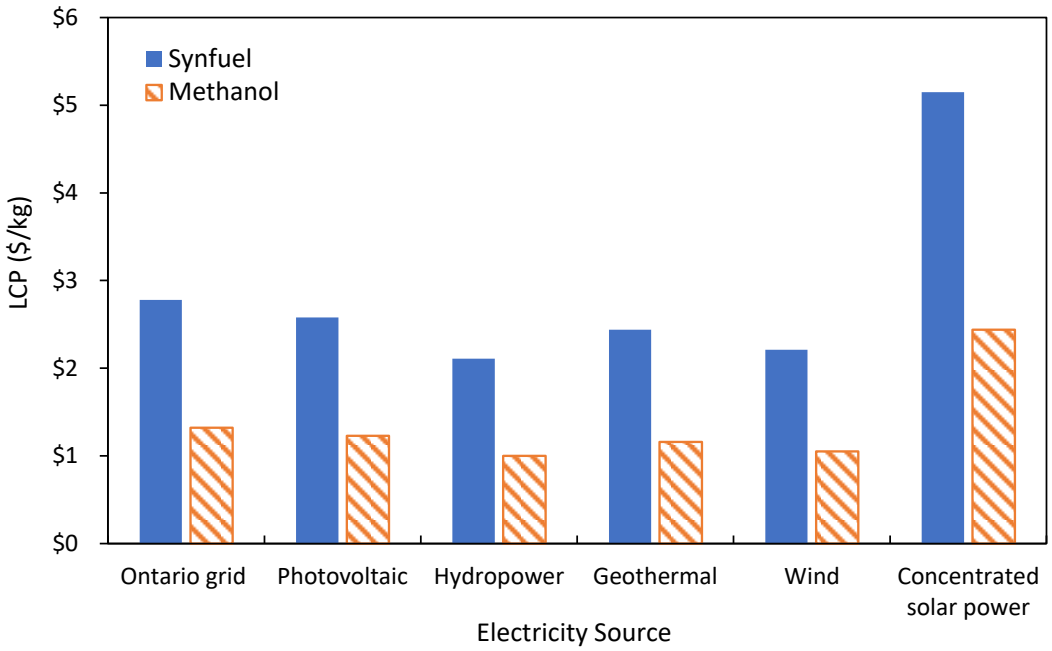


Figure 5.9. Effect of electricity sources on the levelized cost of production. Ontario grid was the base case scenario.

The replacement period of cells in a solid oxide electrolysis plant is a crucial factor influencing plant costs. Longer replacement period will reduce the purchase cost of the equipment significantly

and also typically result in reduced maintenance expenses and downtime associated with cell replacements, leading to improved operational efficiency and lower overall operating costs. However, extending the replacement period too far may risk performance degradation or failure of aging cells, potentially increasing maintenance costs and jeopardizing production reliability.

In Figure 5.10, the impact of the solid oxide electrolysis cell (SOEC) replacement period on the LCP is illustrated. As the replacement period is extended from 2 to 4 years, 4 to 8 years, and 8 to 12 years, there is a notable reduction in the LCP by 18.5%, 11.4% and 4.3%, respectively. However, beyond an 8-year replacement period, the reduction in LCP becomes less significant. This suggests that while increasing the replacement period up to 8 years leads to substantial cost savings, further extension beyond this point yields is much less impactful on the LCP.

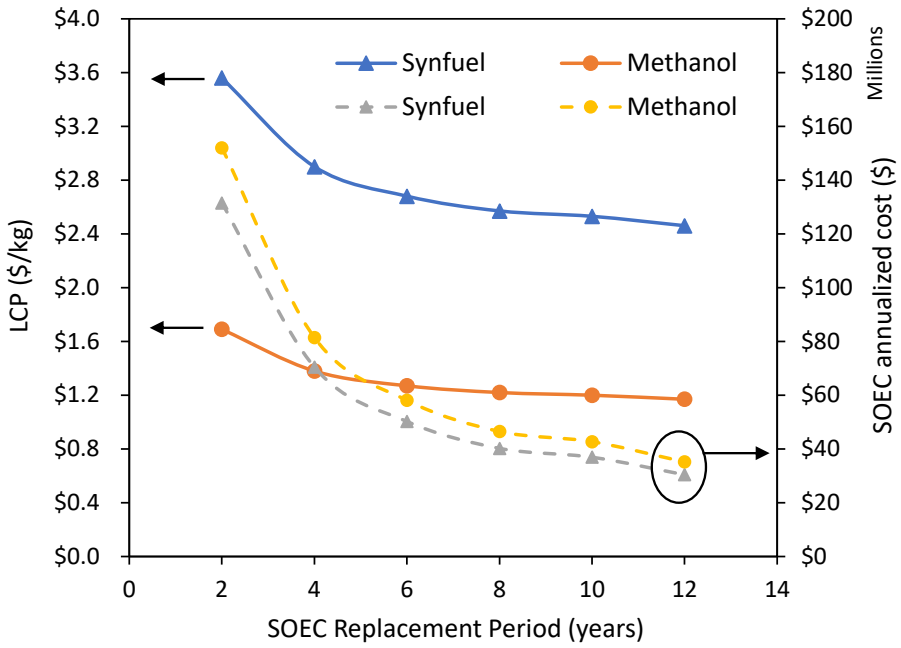


Figure 5.10. Effect of SOEC replacement period on the levelized cost of production.

Figure 5.11 illustrates the LCP for various scenarios of SOEC price reduction. In the least favorable scenario, where only a 10% reduction in SOEC price occurs, the LCP is estimated to be

around $1.47 and $3.08 per kilogram for methanol and synfuel, respectively. Conversely, in the most optimistic scenario with a 50% reduction in SOEC price, the LCP decreases to $1.23 and $2.58 per kilogram for methanol and synfuel, respectively. These findings underscore the critical importance of accurately forecasting and managing SOEC price, as they directly impact the economic viability and competitiveness of producing methanol and synfuel through solid oxide electrolysis. Additionally, they highlight the potential range of outcomes based on different levels of cost reduction, emphasizing the need for strategic planning and flexibility in adapting to changing cost dynamics over time.

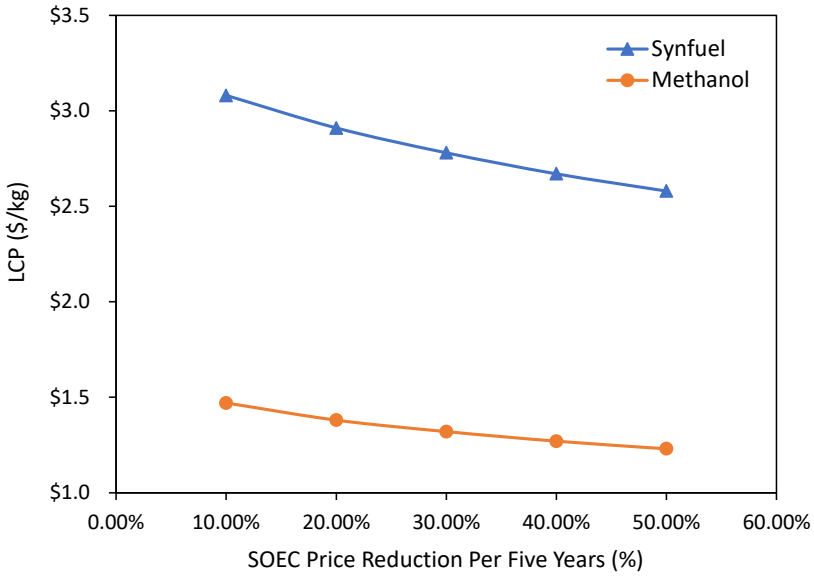


Figure 5.11. Effect of SOEC cost reduction per five years on the levelized cost of production.

Interest rates directly influence the operational and investment costs of industrial plants. For the base case scenario, a 10% interest rate was used. This can affect the cost of production greatly. As Figure 5.12 shows, by increasing the interest rate by 10% point, the LCP increases by 25% for both cases.

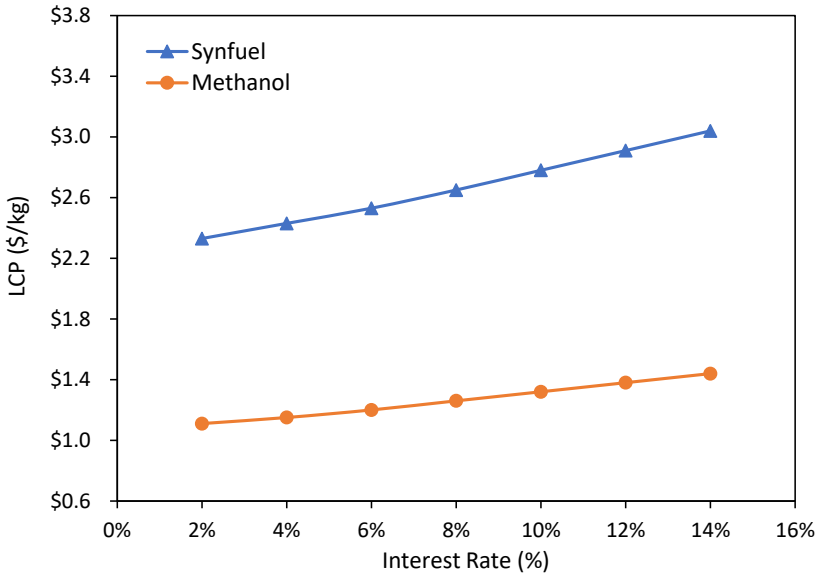


Figure 5.12. Effect of interest rate on the levelized cost of production.

5.4.3 Environmental analysis

To be able to measure how compatible the designed plant is with the environment, the amount of carbon output and input to the system should be considered. The main goal of designing this system is to achieve a system that recycles carbon in the air and turns it into a product, resulting, in principle, in significant overall reduction in greenhouse gas emissions. To quantify how this goal is achieved, the amount of carbon dioxide entering the system should be compared with the amount of carbon in the produced fuel and the purged carbon dioxide/monoxide. As presented in Table 5.10, for the methanol case, 647.7 kmol/hr CO_2 is absorbed in the DAC unit. Besides that, 659.6 kmol/hr CO_2 is the byproduct of natural gas combustion in the Kiln. Altogether, 1307.3 kmol/hr CO_2, either captured or generated within the process, need to be converted to useful fuel. An amount of 171.2 kmol/hr CO_2 is purged back to atmosphere through process and the rest, 1136.3 kmol/hr, is converted to methanol. The CO_2 capture per amount of product (CCPP) for the methanol case is 0.58 kg-CO_2/kg-MeOH. In synfuel case 647.7 kmol/hr CO_2 is absorbed in the DAC unit and 442.0 kmol/hr CO_2 is generated by combusting natural gas. Out of the resulting

1089.7 kmol/hr CO_2, only 3.21 kmol/hr CO_2 is purged to the atmosphere and the rest is converted to synfuel. The CCPP for the synfuel case is 1.88 kg-CO_2/kg-synfuel.

The impact of greenhouse gas (GHG) emissions on global warming is a critical concern in today's climate discourse. We assess how the emissions from the proposed plant contribute to this phenomenon, measured in carbon dioxide equivalent (CO_2-eq). In this study, Ontario's electricity grid was used for GHG calculations. Ontario's grid is among the cleanest globally, with 91% of its supply coming from low-carbon sources like nuclear, hydro, and renewables [85]. This contributes to the low GHG emissions calculated. However, grids in regions reliant on coal or other fossil fuels would result in significantly higher emissions, underscoring the impact of regional electricity supply on environmental performance.

When considering Ontario's grid and natural gas for GHG calculations, as depicted in Figure 5.13, the greenhouse gas (GHG) emissions for methanol production amount to 31.1 g-CO_2-eq/MJ-MeOH. The conventional methanol production system using natural gas exhibits a higher carbon footprint of 40 g-CO_2-eq/MJ-MeOH [88] This is primarily due to its reliance on fossil fuels. Wei et al. [55] proposed a similar system and calculated a carbon footprint of 0.61 kg-CO_2-eq/kg-MeOH, which is very close to our value of 0.60 kg-CO_2-eq/kg-MeOH. As shown in Figure 5.13, the greenhouse gas (GHG) emissions for synfuel production stands at 5.2 g CO_2-eq/MJ-synfuel, which is one-sixth of conventional systems at 29 g-CO_2-eq/MJ-synfuel [64]. These emissions can be notably reduced by transitioning to renewable sources of electricity. Figure 5.14 illustrates the GHG emissions associated with different electricity sources. Notably, hydropower exhibits the lowest global warming impact, with emissions of 17.4 g-CO_2-eq/MJ-MeOH and -20.3 g-CO_2-eq /MJ-synfuel. This implies that when hydropower is utilized for synfuel production, the overall net CO_2 emissions are negative, indicating a reduction in atmospheric CO_2 levels. However, it should

be noted that hydropower is geographically a limited source of energy. In addition to hydropower, wind energy emerges as a favorable option, resulting in negative emissions for synfuel production. These findings underscore the potential of renewable energy sources to significantly mitigate GHG emissions associated with industrial processes, highlighting the importance of transitioning towards sustainable energy solutions to address climate change effectively.

Table 5.10. Carbon balance for methanol and synfuel production.

Term	Methanol	Synfuel
Carbon entering the system (kmol/hr):		
Atmospheric CO_2	648	648
Kiln fuel	660	442
Carbon exiting the system (kmol/hr):		
Purged CO_2	171	3.21
Fuel produced	1137	1087
CO_2 captured (kmol/hr) (Atmospheric CO_2 captured – purged CO_2)	477	645
CCPP (kg-$CO_{2captured}$/kg-product)	0.58	1.88

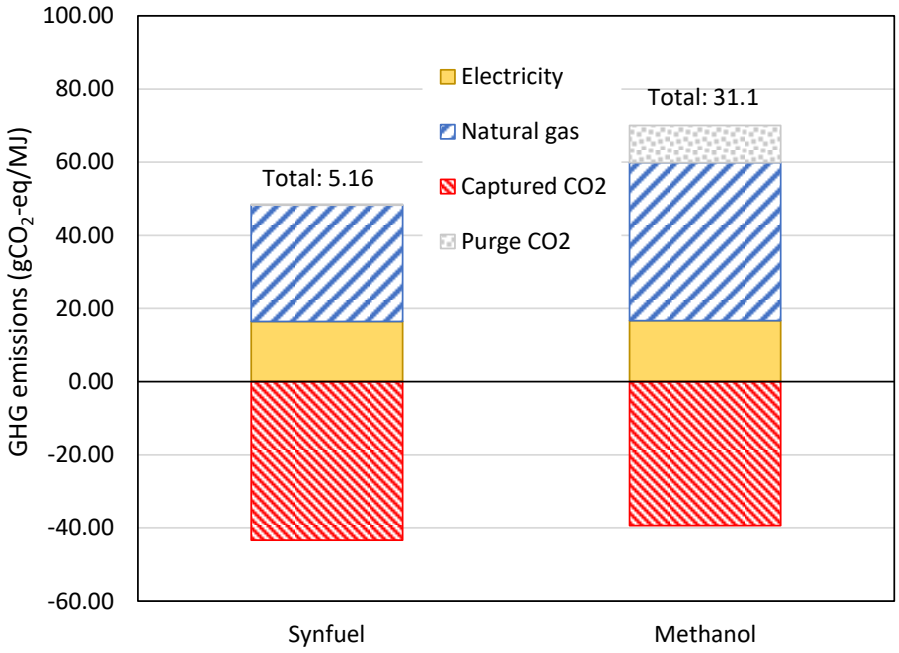


Figure 5.13. GHG emissions contributors for both case studies.

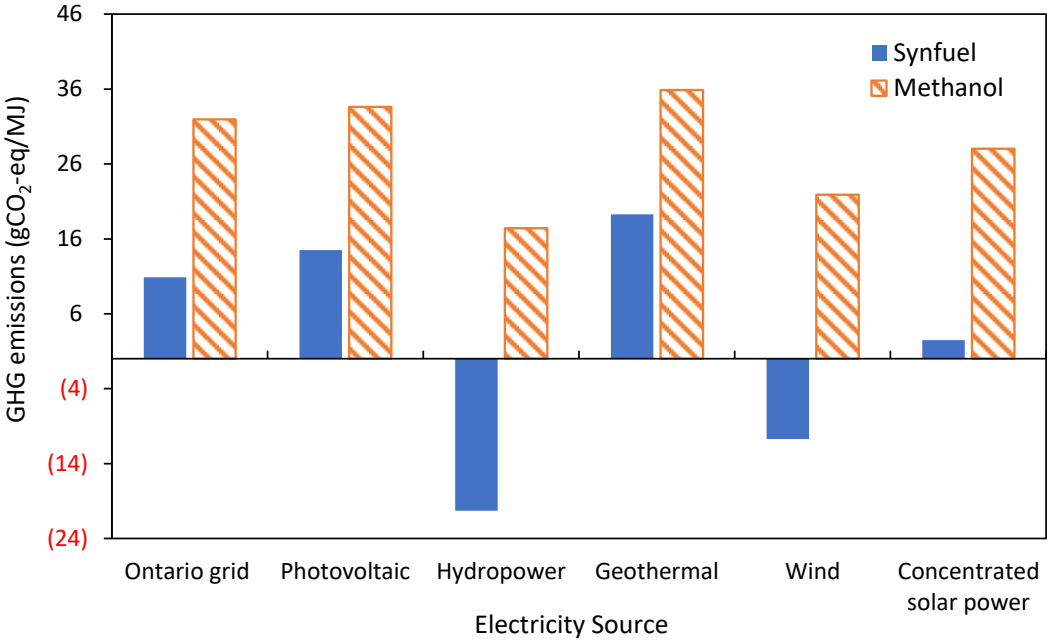


Figure 5.14. GHG emissions for different sources of electricity.

5.5 Simulation study conclusion

The simulation study presents a detailed analysis of a system designed to produce chemicals by capturing CO_2 from the atmosphere, leveraging synergies between DAC and SOEC technologies. The system, based on a DAC capacity of 250,000 tonnes CO_2 per year, achieves production rates of 36.4 tonnes/hour of methanol or 15.1 tonnes/hour of synfuel. Methanol production requires 403 MW of electricity and 10.9 tonnes/hour of natural gas, with a specific energy consumption of 26.0 kWh/kg. Synfuel production demands higher energy at 53.9 kWh/kg but offers lower CO_2 emissions per unit product.

Economic analysis indicates levelized production costs of $1.32/kg for methanol (double the current cost) and $2.78/kg for synfuel (45% higher than current cost). Using Ontario's grid, environmental assessment shows emissions of 31.1 gCO_2-eq/MJ for methanol (22% lower than current emission) and 5.2 gCO_2-eq/MJ for synfuel (one-sixth of the current emission). Clearly, the synfuel case shows more promises than the methanol case. Transitioning to renewable electricity sources can significantly reduce these emissions, even achieving negative emissions for synfuel when powered by hydropower or wind.

While the system faces challenges such as high initial investment costs, advancements in SOEC technology and the adoption of renewable energy sources provide a pathway to cost-effective and environmentally sustainable chemical production. This highlights the system's potential to contribute to global decarbonization efforts.

Chapter 6

Conclusions and Recommendations for Future Work

6.1 Conclusion

This PhD thesis set out to fill in two important gaps in the field of solid oxide CO_2 electrolysis: how to make cathode materials that are both efficient and stable, and to assess the benefits of combining SOECs with other technologies to make carbon-neutral fuel. SOECs show decent performance, but for them to be commercially viable, they need to have both performance and stability, especially at the cathode, and show that they are techno-economically feasible at the system level. This work helps both sides by suggesting a nanoparticle-decorated perovskite cathode and testing its performance in the lab, as well as simulating a whole DAC-SOEC-fuel production process to see how well it could operate on a larger scale.

The first half of the thesis was about the cathode side of the SOEC, which is still the major problem with CO_2 electrolysis. $Sr_2Fe_{1.5}Mo_{0.5}O_{6-\delta}$ (SFM), a double perovskite that has been extensively researched, was modified by adding bismuth and nickel to make $Bi_{0.1}Sr_{1.9}Fe_{1.4}Ni_{0.1}Mo_{0.5}O_{6-\delta}$ (BiSFMNi). Under reducing conditions, the phases changed partially and Fe–Ni nanoparticles were exsolved out of the material in-situ. XRD, Rietveld refinement, and microscopy all showed that there were metallic nanoparticles with a mixed-phase structure.

These exsolved nanoparticles added more active sites, made it easier for CO_2 to adsorb to the surface and be activated, as well as speeding up the surface exchange kinetics. The nanoparticle-decorated cathode performed better, reaching a current density of 1.3 A/cm^2 at 1.6 V and 800 °C, compared to 1.0 A/cm^2 for the undoped sample. Electrochemical impedance spectroscopy and DRT demonstrated lower polarization resistance, from 0.38 0.3 Ω cm^2 for BiSFMNi to 0.3 for Fe–

Ni@BiSFMNi at 1.4 V. These results show how important nanoparticle exsolution is for getting around kinetic barriers and making SOEC cathodes work better.

The second half of the thesis is about the use process modelling (Aspen Plus here) to model and test the viability of a fully integrated system that combines direct air capture (DAC), SOEC-based H_2O/CO_2 co-electrolysis, and chemical synthesis of methanol and synthetic fuel (synfuel) downstream. The system was designed to capture 250,000 tons of CO_2 per year from the air. The simulation revealed that methanol could be made at a rate of 36.4 tonnes per hour and synfuel at a rate of 15.1 tonnes per hour.

The techno-economic study showed that methanol and synfuel could be made at $1.32/kg and $2.78/kg, respectively. These prices are higher than the market price (about double), yet the environmental performance is significantly better, even though it is highly dependent on the source of electricity. Using electrical grid in Ontario, Canada, equivalent CO_2 emissions for production were calculated as 31.1 gCO_2-eq/MJ for methanol (22% lower than current emission) and 5.2 gCO_2-eq/MJ for synfuel (one-sixth of the current emission). The synfuel pathway can even have net-negative production emissions when it gets its energy from renewable sources like wind or water. The high initial cost is still a problem, but these results show that technology could be a long-term solution for fuel production that doesn't add to carbon emissions or even takes them aways.

The experimental and simulation results in this thesis show how new ideas in material engineering and process integration can give a broader picture to solve important problems in CO_2 electrolysis.

6.2 Recommendations for future work

Although this thesis contributes to the advancement of SOECs for CO_2 electrolysis, several areas remain open for future research:

- Long-term stability:

Fe–Ni nanoparticle exsolution improved short-term performance, but it is needed to look at how long it lasts under cyclic redox circumstances, including particles agglomeration, reoxidation behavior, and phase evolution over time.

- Cathode microstructure engineering:

Future studies could investigate optimization of porosity, particle size distribution, and triple phase boundary length to further enhance mass transport and reaction kinetics.

- Scalability of cathode fabrication:

The sol-gel and screen-printing methods used here are lab-scale. Scalable and cost-effective fabrication techniques, such as tape-casting, for nanoparticle-decorated perovskites should be developed for commercial viability.

- Investigating the co-electrolysis of CO_2 and H_2O to produce syngas:

This process would allow the simultaneous reduction of both CO_2 and steam, leading to a tunable syngas ratio (CO/H_2) suitable for downstream fuel synthesis via Fischer–Tropsch or other catalytic routes. Exploring this pathway would also provide insights into electrode stability, reaction kinetics, and long-term durability under more complex operating conditions compared to pure CO_2 electrolysis.

- Full cell integration and stack testing:

This work focuses on single-cell performance, however validating the cathode material in a multi-cell stack and under more realistic operating conditions would be essential.

- System-level optimization:

Further optimize operating parameters and explore alternative CO_2 capture methods, such as absorption and adsorption methods, to identify more efficient and flexible system configurations.

- Techno-economic sensitivity under market dynamics:

Extending the economic analysis to include future electricity cost projections, carbon pricing mechanisms, and policy incentives could help determine under what conditions DAC–SOEC–synfuel systems become competitive. This should also include evaluating different DAC technologies, integration with point-source CO_2 capture from hard-to-abate industries such as steel or cement.

- Alternative Fuels

The current system focuses on methanol and synfuel production. Downstream synthesis of other chemicals such as ethanol, or aviation fuel could diversify product streams and improve overall economics.

References

[1] Daily CO2 n.d. https://co2.earth/daily-co2 (accessed March 10, 2025).

[2] Wu XY, Ghoniem AF. Mixed ionic-electronic conducting (MIEC) membranes for thermochemical reduction of CO2: A review. Prog Energy Combust Sci 2019;74:1–30. https://doi.org/10.1016/J.PECS.2019.04.003.

[3] Barahimi V, Ho M, Croiset E. From Lab to Fab: Development and Deployment of Direct Air Capture of CO2. Energies 2023, Vol 16, Page 6385 2023;16:6385. https://doi.org/10.3390/EN16176385.

[4] Goksu A, Li H, Liu J, Duyar MS. Nanoreactor Engineering Can Unlock New Possibilities for CO2 Tandem Catalytic Conversion to C-C Coupled Products. Global Challenges 2023;7:2300004. https://doi.org/10.1002/GCH2.202300004.

[5] Kim SJ, Choi GM. Stability of LSCF electrode with GDC interlayer in YSZ-based solid oxide electrolysis cell. Solid State Ion 2014;262:303–6. https://doi.org/10.1016/J.SSI.2014.01.001.

[6] Li Y, Chen X, Yang Y, Jiang Y, Xia C. Mixed-Conductor Sr2Fe1.5Mo0.5O6-δ as Robust Fuel Electrode for Pure CO2 Reduction in Solid Oxide Electrolysis Cell. ACS Sustain Chem Eng 2017;5:11403–12. https://doi.org/10.1021/ACSSUSCHEMENG.7B02511

[7] Ebbesen SD, Jensen SH, Hauch A, Mogensen MB. High temperature electrolysis in alkaline cells, solid proton conducting cells, and solid oxide cells. Chem Rev 2014;114:10697–734. https://doi.org/10.1021/CR5000865.

[8] Reytier M, Di Iorio S, Chatroux A, Petitjean M, Cren J, De Saint Jean M, et al. Stack performances in high temperature steam electrolysis and co-electrolysis. Int J Hydrogen Energy 2015;40:11370–7. https://doi.org/10.1016/J.IJHYDENE.2015.04.085.

[9] Jiang Y, Chen F, Xia C. A review on cathode processes and materials for electro-reduction of carbon dioxide in solid oxide electrolysis cells. J Power Sources 2021;493:229713. https://doi.org/10.1016/j.jpowsour.2021.229713.

[10] Zhang L, Hu S, Zhu X, Yang W. Electrochemical reduction of CO 2 in solid oxide electrolysis cells. Journal of Energy Chemistry 2017;26:593–601.

https://doi.org/10.1016/j.jechem.2017.04.004.

[11] Hussain S, Yangping L. Review of solid oxide fuel cell materials: cathode, anode, and electrolyte. Energy Transitions 2020 4:2 2020;4:113–26. https://doi.org/10.1007/S41825-020-00029-8.

[12] He S, Zou Y, Chen K, Jiang SP. A critical review of key materials and issues in solid oxide cells. Interdisciplinary Materials 2023;2:111–36. https://doi.org/10.1002/IDM2.12068.

[13] Ishihara T, Matsuda H, Takita Y. Doped LaGaO3 Perovskite Type Oxide as a New Oxide Ionic Conductor. J Am Chem Soc 1994;116:3801–3. https://doi.org/10.1021/JA00088A016/ASSET/JA00088A016.FP.PNG_V03.

[14] Curi M, da Silva ER, de Furtado JGM, Ferraz HC, Secchi AR. Anodes for SOFC: Review of material selection, interface and electrochemical phenomena. Quim Nova 2021;44:86–97. https://doi.org/10.21577/0100-4042.20170652.

[15] Shen M, Ai F, Ma H, Xu H, Zhang Y. Progress and prospects of reversible solid oxide fuel cell materials. IScience 2021;24:103464. https://doi.org/10.1016/J.ISCI.2021.103464.

[16] Jiang SP, Chan SH. A review of anode materials development in solid oxide fuel cells. Journal of Materials Science 2004 39:14 2004;39:4405–39. https://doi.org/10.1023/B:JMSC.0000034135.52164.6B.

[17] Xu X, Zhong Y, Shao Z. Double Perovskites in Catalysis, Electrocatalysis, and Photo(electro)catalysis. Trends Chem 2019;1:410–24. https://doi.org/10.1016/J.TRECHM.2019.05.006.

[18] Shu L, Sunarso J, Hashim SS, Mao J, Zhou W, Liang F. Advanced perovskite anodes for solid oxide fuel cells: A review. Int J Hydrogen Energy 2019;44:31275–304. https://doi.org/10.1016/J.IJHYDENE.2019.09.220.

[19] George G, Ede SR, Luo Z. Fundamentals of Perovskite Oxides : Synthesis, Structure, Properties and Applications. Fundamentals of Perovskite Oxides 2020. https://doi.org/10.1201/9780429351419.

[20] Sun H, Xu X, Song Y, Shao Z. Recent Progress in Sr2Fe1.5Mo0.5O6-δ-Based Multifunctional Materials for Energy Conversion and Storage. Adv Funct Mater

2024;34:2411622. https://doi.org/10.1002/ADFM.202411622.

[21] Qiu P, Sun S, Li J, Jia L. A review on the application of Sr2Fe1.5Mo0.5O6-based oxides in solid oxide electrochemical cells. Sep Purif Technol 2022;298:121581. https://doi.org/10.1016/j.seppur.2022.121581.

[22] Li Y, Li P, Hu B, Xia C. A nanostructured ceramic fuel electrode for efficient CO2/H2O electrolysis without safe gas. J Mater Chem A Mater 2016;4:9236–43. https://doi.org/10.1039/C6TA02830F.

[23] Li Y, Chen X, Yang Y, Jiang Y, Xia C. Mixed-Conductor Sr2Fe1.5Mo0.5O6-δ as Robust Fuel Electrode for Pure CO2 Reduction in Solid Oxide Electrolysis Cell. ACS Sustain Chem Eng 2017;5:11403–12. https://doi.org/10.1021/ACSSUSCHEMENG.7B02511.

[24] Lv H, Zhou Y, Zhang X, Song Y, Liu Q, Wang G, et al. Infiltration of Ce0.8Gd0.2O1.9 nanoparticles on Sr2Fe1.5Mo0.5O6- cathode for CO2 electroreduction in solid oxide electrolysis cell. Journal of Energy Chemistry 2019;35:71–8. https://doi.org/10.1016/j.jechem.2018.11.002.

[25] Xi X, Liu J, Luo W, Fan Y, Zhang J, Luo J-L, et al. Unraveling the Enhanced Kinetics of Sr2Fe1+xMo1-xO6-δ Electrocatalysts for High-Performance Solid Oxide Cells. Adv Energy Mater 2021;11:2102845. https://doi.org/10.1002/AENM.202102845.

[26] Li Y, Zhan Z, Xia C. Highly efficient electrolysis of pure CO_2 with symmetrical nanostructured perovskite electrodes. Catal Sci Technol 2018;8:980–4. https://doi.org/10.1039/C7CY02324C.

[27] Wang Y, Liu T, Fang S, Chen F. Syngas production on a symmetrical solid oxide H2O/CO2 co-electrolysis cell with Sr2Fe1.5Mo0.5O6–Sm0.2Ce0.8O1.9 electrodes. J Power Sources 2016;305:240–8. https://doi.org/10.1016/j.jpowsour.2015.11.097.

[28] Hou S, Xie K. Enhancing the performance of high-temperature H2O/CO2 co-electrolysis process on the solid oxide Sr2Fe1.6Mo0.5O6-δ-SDC/LSGM/Sr2Fe1.5Mo0.5O6-δ-SDC cell. Electrochim Acta 2019;301:63–8. https://doi.org/10.1016/j.electacta.2019.01.164.

[29] Xu X, Mace B, Enriquez E, Bao S, Harrell Z, Chen C, et al. Roles of reaction kinetics of CO2 on a PrBaCo2O5.5+δ surfaces. RSC Adv 2017;7:40558–62. https://doi.org/10.1039/C7RA06362H.

[30] Niu B, Lu C, Yi W, Luo S, Li X, Zhong X, et al. In-situ growth of nanoparticles-decorated double perovskite electrode materials for symmetrical solid oxide cells. Appl Catal B 2020;270:118842. https://doi.org/10.1016/j.apcatb.2020.118842.

[31] Jiang Y, Yang Y, Xia C, Bouwmeester HJM. Sr2Fe1.4Mn0.1Mo0.5O6−δ perovskite cathode for highly efficient CO2 electrolysis. J Mater Chem A Mater 2019;7:22939–49. https://doi.org/10.1039/C9TA07689A.

[32] Xu C, Zhen S, Ren R, Chen H, Song W, Wang Z, et al. Cu-Doped Sr2Fe1.5Mo0.5O6−δ as a highly active cathode for solid oxide electrolytic cells. Chemical Communications 2019;55:8009–12. https://doi.org/10.1039/C9CC03455B.

[33] Xi X, Liu J, Fan Y, Wang L, Li J, Li M, et al. Reducing d-p band coupling to enhance CO2 electrocatalytic activity by Mg-doping in Sr2FeMoO6-δ double perovskite for high performance solid oxide electrolysis cells. Nano Energy 2021;82:105707. https://doi.org/10.1016/J.NANOEN.2020.105707.

[34] Sun C, Bian L, Qi J, Yu W, Li S, Hou Y, et al. Boosting CO2 directly electrolysis by electron doping in Sr2Fe1.5Mo0.5O6-δ double perovskite cathode. J Power Sources 2022;521:230984. https://doi.org/10.1016/j.jpowsour.2022.230984.

[35] Yang M, Yao Z, Liu S, Wang J, Sun A, Xu H, et al. Bismuth doped Sr2Fe1.5Mo0.5O6-double perovskite as a robust fuel electrode in ceramic oxide cells for direct CO2 electrolysis. J Mater Sci Technol 2023;164:160–7. https://doi.org/10.1016/j.jmst.2023.04.061.

[36] Metallography and Microstructures. Metallography and Microstructures 2004. https://doi.org/10.31399/ASM.HB.V09.9781627081771.

[37] Li Y, Hu B, Xia C, Xu WQ, Lemmon JP, Chen F. A novel fuel electrode enabling direct CO2 electrolysis with excellent and stable cell performance. J Mater Chem A Mater 2017;5:20833–42. https://doi.org/10.1039/C7TA05750D.

[38] Lv H, Lin L, Zhang X, Gao D, Song Y, Zhou Y, et al. In situ exsolved FeNi3 nanoparticles on nickel doped Sr2Fe1.5Mo0.5O6−δ perovskite for efficient electrochemical CO2 reduction reaction. J Mater Chem A Mater 2019;7:11967–75. https://doi.org/10.1039/C9TA03065D.

[39] Lv H, Lin L, Zhang X, Song Y, Matsumoto H, Zeng C, et al. In Situ Investigation of Reversible Exsolution/Dissolution of CoFe Alloy Nanoparticles in a Co-Doped Sr2Fe1.5Mo0.5O6−δ Cathode for CO2 Electrolysis. Advanced Materials 2020;32:1906193. https://doi.org/10.1002/ADMA.201906193.

[40] Chen L, Xu J, Wang X, Xie K. Sr2Fe1.5+xMo0.5O6-δ cathode with exsolved Fe nanoparticles for enhanced CO2 electrolysis. Int J Hydrogen Energy 2020;45:11901–7. https://doi.org/10.1016/j.ijhydene.2020.02.140.

[41] Zhang BW, Zhu MN, Gao MR, Xi X, Duan N, Chen Z, et al. Boosting the stability of perovskites with exsolved nanoparticles by B-site supplement mechanism. Nature Communications 2022 13:1 2022;13:1–12. https://doi.org/10.1038/s41467-022-32393-y.

[42] Xi X, Fan Y, Zhang J, Luo JL, Fu XZ. In situ construction of hetero-structured perovskite composites with exsolved Fe and Cu metallic nanoparticles as efficient CO2 reduction electrocatalysts for high performance solid oxide electrolysis cells. J Mater Chem A Mater 2022;10:2509–18. https://doi.org/10.1039/D1TA07678G.

[43] Lv H, Lin L, Zhang X, Song Y, Li R, Li J, et al. Redox-manipulated RhO nanoclusters uniformly anchored on Sr2Fe1.45Rh0.05Mo0.5O6–δ perovskite for CO2 electrolysis. Fundamental Research 2022. https://doi.org/10.1016/j.fmre.2022.07.010.

[44] Zhang S, Jiang Y, Han H, Li Y, Xia C. Perovskite Oxyfluoride Ceramic with In Situ Exsolved Ni-Fe Nanoparticles for Direct CO2Electrolysis in Solid Oxide Electrolysis Cells. ACS Appl Mater Interfaces 2022;14:28854–64. https://doi.org/10.1021/ACSAMI.2C05324/.

[45] Zhang BW, Zhu MN, Gao MR, Chen J, Xi X, Shen J, et al. Phase Transition Engineering of Host Perovskite toward Optimal Exsolution-facilitated Catalysts for Carbon Dioxide Electrolysis. Angewandte Chemie International Edition 2023;62:e202305552. https://doi.org/10.1002/ANIE.202305552.

[46] Shen Y, Liu T, Li R, Lv H, Ta N, Zhang X, et al. In situ electrochemical reconstruction of Sr2Fe1.45Ir0.05Mo0.5O6-δ perovskite cathode for CO2 electrolysis in solid oxide electrolysis cells. Natl Sci Rev 2023;10. https://doi.org/10.1093/NSR/NWAD078.

[47] Hu F, Ling Y, Fang S, Sui L, Xiao H, Huang Y, et al. Engineering dual-exsolution on self-

assembled cathode to achieve efficient electrocatalytic CO2 reduction. Appl Catal B 2023;337:122968. https://doi.org/10.1016/j.apcatb.2023.122968.

[48] Liu S, Yang M, Xu R, Xiang X, Yang G, Xu H, et al. In situ passivation of Fe nanoparticles exsolved from perovskite cathodes through zinc doping for CO2 electrolysis. Green Chemistry 2023;25:9826–36. https://doi.org/10.1039/D3GC03518B.

[49] Tan T, Wang Z, Qin M, Zhong W, Hu J, Yang C, et al. In Situ Exsolution of Core-Shell Structured NiFe/FeOx Nanoparticles on Pr0.4Sr1.6(NiFe)1.5Mo0.5O6-δ for CO2 Electrolysis. Adv Funct Mater 2022;32:2202878. https://doi.org/10.1002/ADFM.202202878.

[50] López-García A, Almar L, Escolástico S, Hungría AB, Carrillo AJ, Serra JM. Tuning Ternary Alloyed Nanoparticle Composition and Morphology by Exsolution in Double Perovskite Electrodes for CO2Electrolysis. ACS Appl Energy Mater 2022;5:13269–83. https://doi.org/10.1021/ACSAEM.2C01829.

[51] Pfeifer M. Manufacturing Process Considerations. Materials Enabled Designs 2009:115–60. https://doi.org/10.1016/B978-0-7506-8287-9.00005-7.

[52] Fouzaï I, Gentil S, Bassetto VC, Silva WO, Maher R, Girault HH. Catalytic layer-membrane electrode assembly methods for optimum triple phase boundaries and fuel cell performances. J Mater Chem A Mater 2021;9:11096–123. https://doi.org/10.1039/D0TA07470E.

[53] Lv H, Lin L, Zhang X, Li R, Song Y, Matsumoto H, et al. Promoting exsolution of RuFe alloy nanoparticles on Sr2Fe1.4Ru0.1Mo0.5O6−δ via repeated redox manipulations for CO2 electrolysis. Nat Commun 2021;12:1–11. https://doi.org/10.1038/S41467-021-26001-8.

[54] Fulham GJ, Mendoza-Moreno P V., Marek EJ. Managing intermittency of renewable power in sustainable production of methanol, coupled with direct air capture. Energy Environ Sci 2024;17:4594–621. https://doi.org/10.1039/D4EE00933A.

[55] Wei H, Su C, Dai J, Albdeiri MS, Alsenani TR, Elattar S, et al. Towards a sustainable, and economic production future: Proposing a new process for methanol production based on renewable hydrogen. J Clean Prod 2023;389:135976. https://doi.org/10.1016/j.jclepro.2023.135976.

[56] Ferguson KM, Saafan H, Wildeboer EK, Reeves T, Croiset E. Production of Carbon Neutral Methanol Using Co-Electrolysis of CO 2 and Steam in Solid Oxide Electrolysis Cell in Tandem with Direct Air Capture . ECS Trans 2021;103:663–76. https://doi.org/10.1149/10301.0663ECST/XML.

[57] Moreno-Gonzalez M, Berger A, Borsboom-Hanson T, Mérida W. Carbon-neutral fuels and chemicals: Economic analysis of renewable syngas pathways via CO2 electrolysis. Energy Convers Manag 2021;244:114452. https://doi.org/10.1016/j.enconman.2021.114452.

[58] Galán G, Martín M, Grossmann IE. Systematic comparison of natural and engineering methods of capturing CO2 from the air and its utilization. Sustain Prod Consum 2023;37:78–95. https://doi.org/10.1016/J.SPC.2023.02.011.

[59] Zang G, Sun P, Elgowainy A, Wang M. Technoeconomic and Life Cycle Analysis of Synthetic Methanol Production from Hydrogen and Industrial Byproduct CO2. Environ Sci Technol 2021;55:5248–57. https://doi.org/10.1021/ACS.EST.0C08237.

[60] Pricing - Methanex | Methanex n.d. https://www.methanex.com/about-methanol/pricing/ (accessed March 3, 2024).

[61] Morimoto S, Kitagawa N, Bensebaa F, Kumar A, Kataoka S, Taniguchi S. Scenario assessment of introducing carbon utilization and carbon removal technologies considering future technological transition based on renewable energy and direct air capture. J Clean Prod 2023;402:136763. https://doi.org/10.1016/j.jclepro.2023.136763.

[62] Marchese M, Buffo G, Santarelli M, Lanzini A. CO2 from direct air capture as carbon feedstock for Fischer-Tropsch chemicals and fuels: Energy and economic analysis. Journal of CO2 Utilization 2021;46:101487. https://doi.org/10.1016/j.jcou.2021.101487.

[63] D'Adamo I, Gastaldi M, Giannini M, Nizami A-S. Environmental implications and levelized cost analysis of E-fuel production under photovoltaic energy, direct air capture, and hydrogen. Environ Res 2024;246:118163. https://doi.org/10.1016/j.envres.2024.118163.

[64] Liu CM, Sandhu NK, McCoy ST, Bergerson JA. A life cycle assessment of greenhouse gas emissions from direct air capture and Fischer–Tropsch fuel production. Sustain Energy Fuels 2020;4:3129–42. https://doi.org/10.1039/C9SE00479C.

[65] Labunski F, Schnurr B, Pössinger J, Götz T. Environmental Impact of e-Fuels via the Solid Oxide Electrolyzer Cell (SOEC) and Fischer–Tropsch Synthesis (FTS) Route for Use in Germany. Energies 2024, Vol 17, Page 1078 2024;17:1078. https://doi.org/10.3390/EN17051078.

[66] Zang G, Sun P, Elgowainy AA, Bafana A, Wang M. Performance and cost analysis of liquid fuel production from H2 and CO2 based on the Fischer-Tropsch process. Journal of CO2 Utilization 2021;46:101459. https://doi.org/10.1016/j.jcou.2021.101459.

[67] Keith DW, Holmes G, St. Angelo D, Heidel K. A Process for Capturing CO2 from the Atmosphere. Joule 2018;2:1573–94. https://doi.org/10.1016/j.joule.2018.05.006.

[68] Diaz Rodriguez S. Design and modeling of an energy storage system based on solid oxide reversible cells with syngas as fuel and co-electrolysis of CO2 and H2O 2018.

[69] Buttler A, Koltun R, Wolf R, Spliethoff H. A detailed techno-economic analysis of heat integration in high temperature electrolysis for efficient hydrogen production. Int J Hydrogen Energy 2015;40:38–50. https://doi.org/10.1016/J.IJHYDENE.2014.10.048.

[70] Hauck M, Herrmann S, Spliethoff H. Simulation of a reversible SOFC with Aspen Plus. Int J Hydrogen Energy 2017;42:10329–40. https://doi.org/10.1016/J.IJHYDENE.2017.01.189.

[71] Emadi MA, Chitgar N, Oyewunmi OA, Markides CN. Working-fluid selection and thermoeconomic optimisation of a combined cycle cogeneration dual-loop organic Rankine cycle (ORC) system for solid oxide fuel cell (SOFC) waste-heat recovery. Appl Energy 2020;261:114384. https://doi.org/https://doi.org/10.1016/j.apenergy.2019.114384.

[72] Chitgar N, Emadi MA. Development and exergoeconomic evaluation of a SOFC-GT driven multi-generation system to supply residential demands: Electricity, fresh water and hydrogen. Int J Hydrogen Energy 2021;46:17932–54. https://doi.org/10.1016/J.IJHYDENE.2021.02.191.

[73] Lacerda de Oliveira Campos B, John K, Beeskow P, Herrera Delgado K, Pitter S, Dahmen N, et al. A Detailed Process and Techno-Economic Analysis of Methanol Synthesis from H2 and CO2 with Intermediate Condensation Steps. Processes 2022;10:1535. https://doi.org/10.3390/PR10081535/S1.

[74] Graaf GH, Stamhuis EJ, Beenackers AACM. Kinetics of low-pressure methanol synthesis.

Chem Eng Sci 1988;43:3185–95. https://doi.org/10.1016/0009-2509(88)85127-3.

[75] Förtsch D, Pabst K, Groß-Hardt E. The product distribution in Fischer–Tropsch synthesis: An extension of the ASF model to describe common deviations. Chem Eng Sci 2015;138:333–46. https://doi.org/10.1016/J.CES.2015.07.005.

[76] Cinti G, Baldinelli A, Di Michele A, Desideri U. Integration of Solid Oxide Electrolyzer and Fischer-Tropsch: A sustainable pathway for synthetic fuel. Appl Energy 2016;162:308–20. https://doi.org/10.1016/j.apenergy.2015.10.053.

[77] Bukur DB, Pan Z, Ma W, Jacobs G, Davis BH. Effect of CO conversion on the product distribution of a Co/Al 2O3 fischer-tropsch synthesis catalyst using a fixed bed reactor. Catal Letters 2012;142:1382–7. https://doi.org/10.1007/S10562-012-0908-Z.

[78] Prosser JH, James BD, Murphy BM, Wendt DS, Casteel MJ, Westover TL, et al. Cost analysis of hydrogen production by high-temperature solid oxide electrolysis. Int J Hydrogen Energy 2024;49:207–27. https://doi.org/10.1016/j.ijhydene.2023.07.084.

[79] Pratschner S, Radosits F, Ajanovic A, Winter F. Techno-economic assessment of a power-to-green methanol plant. Journal of CO2 Utilization 2023;75:102563. https://doi.org/10.1016/j.jcou.2023.102563.

[80] Natural gas prices for industry by country 2020 | Statista n.d. https://www.statista.com/statistics/253047/natural-gas-prices-in-selected-countries/ (accessed March 4, 2024).

[81] Zhang H, Wang L, Pérez-Fortes M, Van herle J, Maréchal F, Desideri U. Techno-economic optimization of biomass-to-methanol with solid-oxide electrolyzer. Appl Energy 2020;258:114071. https://doi.org/10.1016/j.apenergy.2019.114071.

[82] Industrial electricity prices in major Canadian cities | Statista n.d. https://www.statista.com/statistics/579159/average-industrial-electricity-prices-canada-by-major-city/ (accessed March 4, 2024).

[83] Life Cycle Upstream Emissions Factors 2024 - Data product - IEA n.d. https://www.iea.org/data-and-statistics/data-product/life-cycle-upstream-emissions-factors-2024-2 (accessed October 12, 2024).

[84] Emission factors and reference values - Canada.ca n.d. https://www.canada.ca/en/environment-climate-change/services/climate-change/pricing-pollution-how-it-will-work/output-based-pricing-system/federal-greenhouse-gas-offset-system/emission-factors-reference-values.html (accessed October 12, 2024).

[85] CER – Provincial and Territorial Energy Profiles – Ontario n.d. https://www.cer-rec.gc.ca/en/data-analysis/energy-markets/provincial-territorial-energy-profiles/provincial-territorial-energy-profiles-ontario.html (accessed October 14, 2024).

[86] Uwe R. Fritsche H-WGI. Development of the Primary Energy Factor of Electricity Generation in the EU-28 from 2010-2013 2015.

[87] Zang G, Sun P, Elgowainy AA, Bafana A, Wang M. Performance and cost analysis of liquid fuel production from H2 and CO2 based on the Fischer-Tropsch process. Journal of CO2 Utilization 2021;46:101459. https://doi.org/10.1016/J.JCOU.2021.101459.

[88] The carbon footprint of methanol produced from various feedstocks > studio Gear Up n.d. https://www.studiogearup.com/the-carbon-footprint-of-methanol-produced-from-various-feedstocks/ (accessed January 8, 2025).

Appendix

Table A.1. Calculation of reagent quantities for sol–gel synthesis of $Bi_{0.1}Sr_{1.9}Fe_{1.4}Ni_{0.1}Mo_{0.5}O_{6-\delta}$ Perovskite.

Perovskite components:	Formula:	stoichiometric ratio	Mass of nitrate (g)
Strontium	SrN_2O_6	1.90	19.36
Iron	$FeN_3O_9 \cdot 9H_2O$	1.40	27.23
Nickel	$NiN_2O_6.6H_2O$	0.10	1.40
Molybdenum	$Mo_7N_6H_{24}O_{24}$	0.50	4.25
Bismuth	$Bi(NO_3)_3.5H_2O$	0.10	2.34
	Value	Unit	
EDTA/water:	0.5	g/g	
EDTA/metal:	1	mol/mol	
Ammonia/EDTA:	1	g/g	
Citric acid/metal:	1.5	mol/mol	
Final mass of perovskite:	20	grams	
Mass of EDTA:	56.28	grams	
Mass of ammonia for EDTA:	56.28	grams	
Mass of water for EDTA:	112.56	g/mol	
Mass of citric acid:	55.50	grams	
Water solubility factor:	1.2		
Mass of water for nitrates:	72.83	grams	

Table A.2. Carbon Aspen PLUS™ simulation block types and parameters.

Name	Aspen block type	Parameters
DAC		
CNTCTR1	Sep	CO2 separation: 73.5%
CNTCTR2	RGibbs	Pressure: 1 bar Temperature: 25°C
CAUST	RGibbs	Pressure: 1 bar Heat duty: 0 MW
CYCPUMP	Pump	Discharge pressure: 2.5 bar
SOLIDSEP	HyCyc	Model: solids separator Liquid load of solid outlet: 0.95 Pressure: 1.1 bar Heat duty: 0 MW
SLAKER	RStoic	Pressure: 1.1 bar Heat duty: 0 MW Reaction: $CaO(s) + H_2O(l) \rightarrow Ca(OH)_2(s)$
CALCINER-BURNER	RStoic	Pressure: 1 bar Temperature: 2500°C Reaction: $CH_4(g) + 2O_2(g) \rightarrow CO_2(g) + 2H_2O(g)$
CALCINER-KILN	RStoic	Pressure: 1 bar Temperature: 900°C Reaction: $CaCO_3(s) \rightarrow CO_2(g) + CaO(s)$
SOEC		
SPLIT1	FSplit	Split fraction: 0.36
SPLIT2	FSplit	Split fraction: 0.18
PREHEAT1	HeatX	Hot stream outlet temperature: 200°C
PREHEAT2	HeatX	Hot stream outlet temperature: 400°C
PREHEAT3	HeatX	Cold stream outlet temperature: 900°C
COMP	Compr	Isentropic, Discharge pressure: 1.1 bar

BURNER	RStoic	Pressure: 1 bar Heat duty: 0 MW Reactions: $CH4(g) + 2O_2(g) \rightarrow CO_2(g) + 2H_2O(g)$ $H_2(g) + 0.5O_2(g) \rightarrow H_2O(g)$ $CO(g) + 0.5O_2(g) \rightarrow CO_2(g)$
CATHODE	RGibbs	Pressure: 1 bar Temperature: 800°C
RWGS	RStoic	Pressure: 1 bar Temperature: 800°C Reaction: $2H_2O(g) \rightarrow O_2(g) + 2H_2(g)$
ANODE	MIXER	Pressure: 1 bar
ELECSEP	Sep	O2 separation: 100%
EQUIBOUT	RGibbs	Pressure: 1 bar Temperature: 800°C
Methanol		
FLASH1	Flash2	Pressure: 1 bar Temperature: 40°C
FLASH2	Flash2	Pressure: 1 bar Temperature: 40°C
FLASH3	Flash2	Pressure: 1 bar Temperature: 40°C
COMP	MCompr	Number of stages: 4 Last stage pressure: 70 bar Mid-stage cooling: 40°C
REACTOR	RPlug	Details in Section 2.4
COOLER	HeatX	Hot stream outlet temperature: 40°C
PREHEAT1	HeatX	Hot/cold outlet temperature approach: 10°C
PREHEAT2	HeatX	Hot/cold outlet temperature approach: 10°C
Fischer-Tropsch		
FLASH1	Flash2	Pressure: 1 bar Temperature: 40°C
FLASH2	Flash2	Pressure: 1 bar Temperature: 40°C

COMP	MCompr	Number of stages: 3 Last stage pressure: 25 bar Mid-stage cooling: 40°C
REACTOR	RStoic	Pressure: 25 bar Temperature: 220°C Reactions: Details in Section 2.5
COOLER	Heater	Pressure: 1 bar Temperature: 40°C